Alexander Stiegler, BSc

Mars Permittivity Probe Calibration and Instrument Performance Validation

MASTER THESIS

For obtaining the academic degree
Diplom-Ingenieur

Master Programme of
Technical Physics

Graz University of Technology

Supervisor:

Ao.Univ.-Prof. Dipl.-Ing. Dr.techn. Theo Neger

Institute of Experimental Physics

Graz, June 2011

Deutsche Fassung:
Beschluss der Curricula-Kommission für Bachelor-, Master- und Diplomstudien vom 10.11.2008
Genehmigung des Senates am 1.12.2008

EIDESSTATTLICHE ERKLÄRUNG

Ich erkläre an Eides statt, dass ich die vorliegende Arbeit selbstständig verfasst, andere als die angegebenen Quellen/Hilfsmittel nicht benutzt, und die den benutzten Quellen wörtlich und inhaltlich entnommene Stellen als solche kenntlich gemacht habe.

Graz, am 11.05.2011 ....
(Unterschrift)

Englische Fassung:

STATUTORY DECLARATION

I declare that I have authored this thesis independently, that I have not used other than the declared sources / resources, and that I have explicitly marked all material which has been quoted either literally or by content from the used sources.

11.05.2011 ....
date (signature)

Acknowledgements

I would like to thank the Space Research Institute of the Austrian Academy of Sciences and the University of Technology in Graz for the opportunity to write my master thesis at the Space Research Institute.
Within this institute special thanks go to Dr. Günter Kargl not only for supervising my master thesis, but also for affording me the opportunity to work as a space researcher for some time.
My acknowledgements go to the whole surface science group including Norbert, Mark, Erika K., Erika H. and Wolfgang, who helped me whenever there was need to.
I want to thank my supervisor at the University of Technology in Graz, Ao.Univ.-Prof. Dipl.-Ing. Dr.techn. Theo Neger for his support and his willingness to supervise a thesis at an external institute.
I am thankful to Novocontrol Technologies, who provided me reference data as well as additional information and the FFG Austria for funding the project HP3-PP/819663, within which this work has been performed.

Kurzfassung

Diese Masterarbeit beschreibt die Laborarbeit, die geleistet wurde, um eine Permittivitäts-Sonde für Mars-Anwendung zu kalibrieren und deren wissenschaftlichen Nutzen zu testen. Das beschriebene Instrument ist Teil des HP^3 (**H**eat-flow and **P**hysical **P**roperties **P**ackage) Instrumentes, welches ursprünglich für die europäische ExoMars Mission ausgewählt wurde. Nachdem die Humboldt Landestation dieser Mission, auf der sich das HP^3-Instrument befinden sollte, gestrichen wurde, entschieden sich die Projektverantwortlichen das Instrumentenpaket weiter zu entwickeln, bis eine hohe Reife für Weltraumapplikationen erreicht wird. In diesem Sinne liefert diese Masterarbeit die Kalibrierung des Permittivitäts-Instrumentes des Pakets und die Verifikation dessen wissenschaftlichen Interesses.
Die Permittivitäts-Sonde bestimmt die elektrischen Eigenschaften des Untergrundes. Da sie auf einem automatisierten Penetrator angebracht ist, kann das Instrument Einschlüsse und Schichtungen entlang des Eindringweges erkennen. Als wichtiger wissenschaftlicher Nutzen des Instrumentes gilt seine Sensitivität zu geringen Spuren von Wasser, welches die elektrischen Eigenschaften maßgeblich beeinflusst.
In den letzten Jahren wurden mehrere Permittivitäts-Instrumente für Weltraummissionen ausgewählt, da sie einen hohen wissenschaftlichen Nutzen bei sehr geringer technischer Komplexität durch Messung der Materialimpedanz liefern.
Diese Arbeit beschreibt die physikalischen Hintergründe, die zum Verständnis der Messmethode und der gewonnenen wissenschaftlichen Daten benötigt werden. Spezielle Anforderungen an Messinstrumente im Weltall werden beschrieben und ein Vergleich zu wissenschaftlich annähernd äquivalenten Messmethoden gebracht.
Der Großteil der Arbeit beschäftigt sich mit der Kalibrierung der Permittivitäts-Sonde und der Verifikation ihres wissenschaftlichen Nutzens. Abschließend sollen Erkenntnisse und Verbesserungsvorschläge, die sich im Zuge der Arbeit ergaben, die weitere Entwicklung des Instrumentes fördern.

Abstract

This thesis summarises the work which has been performed to calibrate and test a so called "permittivity probe" for applications on Mars. This instrument is part of the HP^3 (**H**eat-flow and **P**hysical **P**roperties **P**ackage) sensor suite, which was initially selected to be part of the European ExoMars mission. After the cancellation of the ExoMars Humboldt surface station, which included the HP^3 instrument, it was decided to develop the sensor suite further, until a high proto-flight maturity level was achieved. In this sense, the scope of this work was to calibrate the HP^3-Permittivity Probe and to verify its science performance.
This Mars permittivity instrument will determine the electrical properties of its environment with a high accuracy. Located on a self penetrating device, the instrument is able to identify lateral inhomogeneities and layer boundaries along its penetration path. Since the electrical properties of a material are strongly affected even by small H_2O-fractions in a sample, the Permittivity Probe is able to determine the state, abundances and variation of H_2O on surface and sub-surface of the future mission target body.
Due to its high scientific relevance and the comparable easy method of measurement, which goes back to the determination of the sample impedance, permittivity instruments have been selected for several space missions recently in the past.
In this thesis the physical background to understand and interpret the Permittivity Probe measurement and the obtained data will be given. The special requirements for an instrument working in space are listed and a comparison to other operational methods fulfilling the Permittivity Probe requirements is shown. The main part of the thesis explains the laboratory work for calibration and verification of the instrument performance. Finally remarks and conclusion drawn from this work shall enhance the ongoing instrument development.

Contents

CHAPTER 1

Introduction

"The surface of the earth is the shore of the cosmic ocean. [...] Recently, we have waded enough to dampen our toes or, at most, wet our ankles. The water seems inviting. The ocean calls."

(Carl Sagan, U.S. Astronomer)

To understand the formation of our solar system and with that the evolution of life on earth, humans need to explore the universe. There are various ways to do that, earth-based, or even only my simulating the space environment in the laboratory or on computers. Nevertheless, the most precise information will be obtained by the direct exploring of the planets, moons and small bodies in our solar system. Space missions potentially provide clues about the past, the formation as well as the evolution and fate of planetary bodies.
Instruments, that are expected to provide this information within such missions need to obtain a maximum of information with a minimum of mass and power consumption, respectively a minimum of costs. Thus special issues are drawn to a space instrument and its development.
As part of the development of such an instrument, this thesis deals with a so called "permittivity probe", an instrument measuring the electrical properties of planetary bodies.
Since the electrical properties are strongly affected by abundances of water, one major scope of a permittivity instrument is to determine the state, abundance and variation of H_2O on its target body. As H_2O is commonly known to determine the whole planetary evolution, this measurement technique is a comparable easy way to acquire key information about the target body. Other scientific key goals obtained by the measurement of the bodies electrical properties include the determination of local sub-surface stratigraphy and electromagnetic phenomena on surface and in the atmosphere.

Due to the high scientific relevance and the low complexity of such instruments, already three permittivity instruments have been selected to be part of space missions recently in the past.

At Saturn's moon Titan the PWA-MI (**P**ermittivity **W**aves and **A**ltimetry-**M**utual **I**mpedance) probe on ESA's (**E**uropean **S**pace **A**gency) Huygens lander contributed to identify Titan's surface structure and its atmospheric and surface electrical properties. As a tool for ground truth the instrument was expected to give additional information for the GPR (**G**round **P**enetrating **R**adar) instrument on board the Cassini-Orbiter. According to its scientific requirements for the surface experiments, the PWA-MI was able to give an estimation of Titans surface conductivity and permittivity [1].

The second example of a permittivity instrument as part of a space mission is the **T**hermal and **E**lectrical **C**onductivity **P**robe (TECP), which had been on board the NASA Phoenix lander. The scientific objective of this instrument was to help understanding the abundance, the state and the mobility of H_2O in the Mars north polar region. A small diurnal variation of the surface H_2O-content had been detected, which is not really understood until now [2].

The third permittivity instrument which has been selected to measure the electrical properties of a planetary object is part of the SESAME (**S**urface **E**lectric **S**ounding and **A**coustic **M**onitoring **E**xperiment) instrument suite on board ESA's Rosetta-lander Philae. Launched in 2004, it will reach the comet 67P/Churyumov-Gerasimenko in 2014. On the cometary surface the permittivity instrument will identify the mass fraction of H_2O-ice to other surface and sub-surface materials. Furthermore the sensor shall obtain stratigraphic information about the cometary nucleus and it's electron density variations close to the surface as a function of the comet activity [3]. As comets are expected to be the most pristine bodies in our solar system, results obtained within this mission could provide yet unknown information about the history of the solar system.

Initially selected for the ExoMars mission of ESA the HP^3 (**H**eat-Flow and **P**hysical **P**roperties **P**ackage) sensor suite should include the fourth permittivity probe to be part of a space mission. Unfortunately the ExoMars Humboldt surface station, which included the HP^3-instrument, was cancelled. Nevertheless it was decided to develop the HP^3 sensor suite further, until an instrument with a high proto-flight level was achieved.

In this perspective this thesis summarises the work, which has been performed for the development of the HP^3-PP, especially the instrument calibration and the verification of its science performance.

Since the instrument development will be continued, suggestions and remarks as a result of this work should enhance the instrument performance.

All in all this work should contribute to the development of a unique instrument for space applications, which probably will be part of scientific exploration answering fundamental questions about our solar system in the upcoming years.

CHAPTER 2

Phenomenological review on a dielectric material in an electric field

A perfect dielectric is a material that doesn't contain any free charges, basically an insulator. Although there are no free charges, a dielectric material is strongly affected by an external electric field. Maybe the most common example for this fact is the behaviour of a capacitor sandwiching a dielectric material between its electrodes. If one compares the capacity of an empty capacitor C_0 with one (the electrode-geometry and the electrode-charge Q is not varied) filled with a dielectric material C_{diel}, the system capacity C is increased by a sample dependent factor ϵ_r ($\epsilon_r > 1$):

$$\frac{C_{diel}}{C_0} = \epsilon_r$$

With

$$C = \frac{Q}{U},$$

connecting the capacity C with the potential U between the capacitor electrodes, one recognises, that the potential U_{diel} in the filled system is lowered compared to the empty one:

$$\frac{C_{diel}}{C_0} = \frac{U_0}{U_{diel}} = \epsilon_r \quad (\epsilon_r > 1,\ C_{diel} > C_0) \tag{2.1}$$

Thus the total electric field $\mathbf{E}_{total}$ at a point $\mathbf{r}$ in the dielectric consists of two components

$$\begin{aligned} \mathbf{E}_{total} = \mathbf{E} &= \frac{dU_{total}}{d\mathbf{r}} \\ &= \frac{d(U_0 - U_{diel})}{d\mathbf{r}} \\ &= \frac{dU_0}{d\mathbf{r}} - \frac{U_{diel}}{d\mathbf{r}} \\ &= \mathbf{E}_0 + \mathbf{E_1}, \end{aligned}$$

the external field $\mathbf{E}_0$ originating from the capacitor electrodes (as in the vacuum case), a field $\mathbf{E}_1$ originating from the dielectric medium directed in opposite to the external field. The electric field $\mathbf{E}_1$ is the so called depolarisation field, which can be mathematically expressed by a fictive surface charge on the dielectric medium ($\mathbf{n}$ is the surface normal vector). This expression is equivalent to the polarisation $\mathbf{P}$ of the medium:

$$\mathbf{E_1} = -\frac{\gamma}{\epsilon_0}\mathbf{n} = -\frac{P}{\epsilon_0}\mathbf{n} \tag{2.2}$$

(with the dielectric constant $\epsilon_0 = 8.854 \cdot 10^{-12}$ [As(Vm)$^{-1}$])

2.1 Dipole characteristics, polarisation and polarisability

To understand the behaviour of a dielectric material in an external electric field, it is necessary to give a short review of the characteristics of a dipole. In principle a dipole

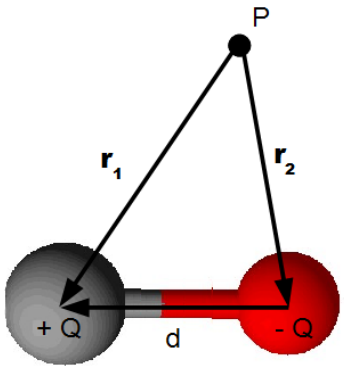

Figure 2.1: A dipole consisting of two charges ± Q separated by distance |**d**|.

consists of two charges of different sign separated by a distance |**d**|. In fig. 2.1 a dipole with charges +Q and -Q is shown. The general expression for the electric moment $\mathbf{p}$ originating from n charges Q at position $P(\mathbf{r})$ is:

$$\mathbf{p} = \sum_i Q_i \mathbf{r}_i$$

For a dipole with charges ± Q as in fig. 2.1 this expression reduces to:

$$\begin{aligned}\mathbf{p} &= +Q\mathbf{r}_1 + (-Q_2)\mathbf{r}_2 \\ &= (\mathbf{r}_1 - \mathbf{r}_2) \cdot Q\end{aligned}$$

With the distance vector $\mathbf{d}$ ($\mathbf{d} = \mathbf{r}_1 - \mathbf{r}_2$) one obtains the expression for the dipole moment $\mathbf{p}$:

$$\mathbf{p} = Q\mathbf{d} \tag{2.3}$$

In an electrical field $\mathbf{E}$, a dipole will try to align to the field lines to minimise its energy. This behaviour is shown for an H_2O molecule in fig. 2.2. A torque is applied to the dipole.

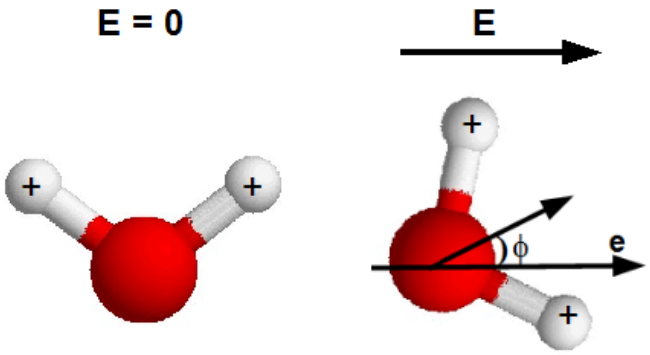

Figure 2.2: The behaviour of an H_2O-molecule with and without electric field $\mathbf{E}$. The dipole tries to align to the field. ϕ is the angle between field line e and the dipole.

ϕ is the angle between the dipole axis and the field line.

$$\mathbf{T} = \mathbf{p} \times \mathbf{E} = |\mathbf{p}| \cdot |\mathbf{E}| \ \sin\phi$$

The energy needed to achieve this torsion and thus the potential energy U of the dipole is:

$$U = -\int_0^{\phi} \mathbf{T} d\phi' \tag{2.4}$$

$$= -\int_0^{\phi} |\mathbf{p}| \ |\mathbf{E}| \sin\phi' d\phi' \tag{2.5}$$

$$= -|\mathbf{p}| \ |\mathbf{E}| \cos\phi \tag{2.6}$$

$$= -\mathbf{p} \ \mathbf{E} \tag{2.7}$$

In general the resulting dipole moment $\mathbf{p}$ is the sum of the existing one $\mathbf{p}_{exist}$ and an induced moment $\mathbf{p}_{ind}$ due to the displacement:

$$\mathbf{p} = \mathbf{p}_{exist} + \mathbf{p}_{ind}$$

The polarisation $\mathbf{P}$ is defined as the sum of dipole moments p per volume V:

$$\mathbf{P} = \frac{\sum_j \mathbf{p_j}}{V}$$

If u is the dipole moment per unit volume, $\mathbf{P}$ is obtained by calculating the mean vector sum of the dipole moments in the considered volume.

$$\mathbf{P} = \langle \sum_i \mathbf{u}_i \rangle$$

For identical, non-interacting molecules the expression above is given by:

$$\mathbf{P} = \sum_i \langle \mathbf{u}_i \rangle = \sum_i N_i \mathbf{u}_i = N \langle \mathbf{u} \rangle \tag{2.8}$$

N is the number of contributing molecules with dipole moment $\mathbf{u}_i$ in the considered volume. The mean value $\langle \mathbf{u} \rangle$ is connected to the field inside the dielectric $\mathbf{E}_{loc}$ through the polarisability α of the medium.[1]

$$\langle \mathbf{u} \rangle = \alpha \mathbf{E}_{loc} \tag{2.9}$$

In the most general case a dipole will not exactly align to the direction of the field $\mathbf{E}_{loc}$. Therefore the polarisability α gets a rank two tensor:

$$\begin{pmatrix} \alpha_{11} & \alpha_{12} & \alpha_{13} \\ \alpha_{21} & \alpha_{22} & \alpha_{23} \\ \alpha_{31} & \alpha_{32} & \alpha_{33} \end{pmatrix} \begin{pmatrix} E_x \\ E_y \\ E_z \end{pmatrix} = \langle \mathbf{u} \rangle$$

To reduce complexity, in this thesis the polarisability α is in general written as scalar value.

[1] The field $\mathbf{E}_{loc}$ is only for rarefied gases the same as the external field $\mathbf{E}_0$. In general the field $\mathbf{E}$ is built up by the external one and other contributions originating from nearby dipoles and other field sources. This field at a certain point in the dielectric medium is called $local field$ (see chapter 3.1.1).

CHAPTER 3

The physics of dielectrics

In this chapter the physical background needed to understand the Permittivity Probe measurement and data will be explained from a microscopic as well as from a macroscopic point of view.

3.1 Microscopic view of dielectrics

To treat a dielectric in a microscopic way, one has to define the local field inside the medium. With this the mechanism of polarisation can be explained, which defines the measurable parameters of a dielectric material.

3.1.1 The local field

In chapter 2 the macroscopic electric field $\mathbf{E}$ was described as sum of an external field $\mathbf{E}_0$ and the depolarisation field $\mathbf{E}_1$.
From a microscopic point of view one can state generally that the field inside a dielectric medium is built up by the external field $\mathbf{E}_0$ and a field originating from inside the medium $\mathbf{E}_{diel}$, which includes te depolarisation field $\mathbf{E}_1$:

$$\mathbf{E}_{diel} = \mathbf{E_1} + \text{microscopic contributions}$$

To get a clear understanding about the microscopic behaviour of a dielectric material in an electric field, one has to define the local field $\mathbf{E}_{loc}$, which is the sum of those two:

$$\mathbf{E}_{loc} = \mathbf{E}_0 + \mathbf{E}_{diel}$$

The local field is the true microscopic field at a certain point in the medium. This field can be split up in its contributing parts (according to fig. 3.1) [4]:

$$\mathbf{E}_{loc} = \underbrace{\mathbf{E}_0 + \mathbf{E}_1}_{} + \underbrace{\mathbf{E}_2 + \mathbf{E}_3}_{} \tag{3.1}$$

$$= \quad \mathbf{E} \quad + \quad \mathbf{E}_{micro} \tag{3.2}$$

In the considered approach, which has been first calculated by Lorentz, $\mathbf{E}_{micro}$ consists of

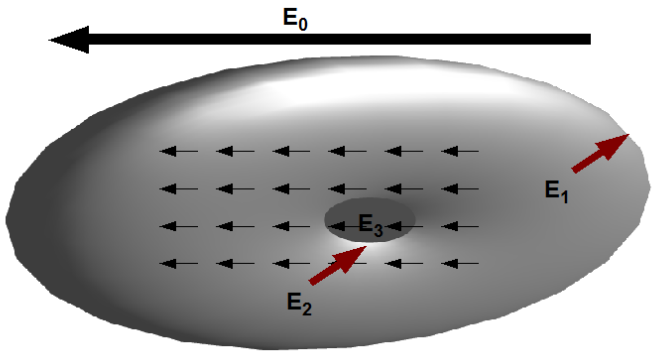

Figure 3.1: To calculate the local field $\mathbf{E}_{loc}$ one has to consider the external field $\mathbf{E}_0$, the depolarisation field $\mathbf{E}_1$, the so called Lorentz-field from the surface of the considered hollow sphere $\mathbf{E}_2$ and the field originating from the dipoles in the hollow sphere $\mathbf{E}_3$.

two microscopic components.
The local field is calculated by considering a hollow sphere embedded in a homogeneously polarised dielectric medium [4]. Four field sources are considered in this model:

- $\mathbf{E}_0$ is the field of external charges
- $\mathbf{E}_1$ is the depolarisation field
- $\mathbf{E}_2$ is the $Lorentz - field$ from the surface of the hollow sphere
- $\mathbf{E}_3$ is the field from the atoms inside the hollow sphere

The field inside the hollow sphere $\mathbf{E}_3$ is zero, if one suggests randomly orientated not interacting dipoles in the cavity. Supposing that the macroscopic field $\mathbf{E}$ is known, only the microscopic field $\mathbf{E}_2$ remains unknown. The field $\mathbf{E}_2$ is obtained by evaluating the field $d\mathbf{E}\cos\theta$ originating from each area $d\mathbf{S}$ of the hollow sphere. With Coulomb's law including

the surface charge on the hollow sphere (eq. 2.2) one gets:

$$\mathbf{E}_2 = \int_{\mathbf{S}} \frac{\mathbf{P}\cos^2\theta}{4\pi\epsilon_0 r^2} \tag{3.3}$$

$$= \frac{1}{2\epsilon_0}\mathbf{P}\int_0^{\pi} \sin\theta\cos^2\theta d\theta \tag{3.4}$$

$$= -\frac{2}{3\epsilon_0}\mathbf{P}|_0^{\pi}\cos^3\theta \qquad \text{by [5]} \tag{3.5}$$

$$\mathbf{E}_2 = \frac{\mathbf{P}}{3\epsilon_0} \tag{3.6}$$

Consequently the Lorentz-field is linearly related to the polarisation $\mathbf{P}$.
The Lorentz treatment of the local field does not imply any dipole interactions. Thus, if one is interested on materials exhibiting strong dipole interaction (e.g. H_2O) one has to work with other more complex models like the Onsager model [6].
For the following considerations the field $\mathbf{E}$ affecting the inner material structure is defined to be the local field $\mathbf{E}_{loc}$.

3.2 The mechanism of electric polarisation

The dielectric properties of a material are determined by its molecular components. A first classification of dielectrics separates materials with permanent dipole moments from those with non-polar constituents. If an external electric field is applied, permanent dipoles will be orientated - so called orientational polarisation occurs. If there are no existing dipoles, an external field will induce a polarisation. Both mechanism are sketched in fig. 3.2. Permanent dipoles (e.g. H_2O) are randomly orientated at zero field, but try to align, if a field $\mathbf{E}$ is applied. In the case of non-polar constituents, as on the left side of fig. 3.2 for CO_2, the movement of the in opposite charged particles will vary the centres of total positive and negative charges. These centres will not coincidence anymore, a dipole is induced.

A further classification splits up the different particles contributing to the macroscopic polarisation. Due to the difference in their masses and inertia a frequency dependence to the external electric field exists.

3.2.1 Material with non-polar constituents - Induced polarisation

To describe the mechanism of induced polarisation, one has to consider a mass that is oscillating around a centre point. For a first approximation there is no need to distinguish between atoms, ions or electrons. As an example a CO_2 molecule in an electric field $\mathbf{E}$ is sketched in fig. 3.3. In every case the displacement x of the considered mass m (e.g. the centre-mass in fig. 3.3) due to an external force F_x in an electric field E_x is described by

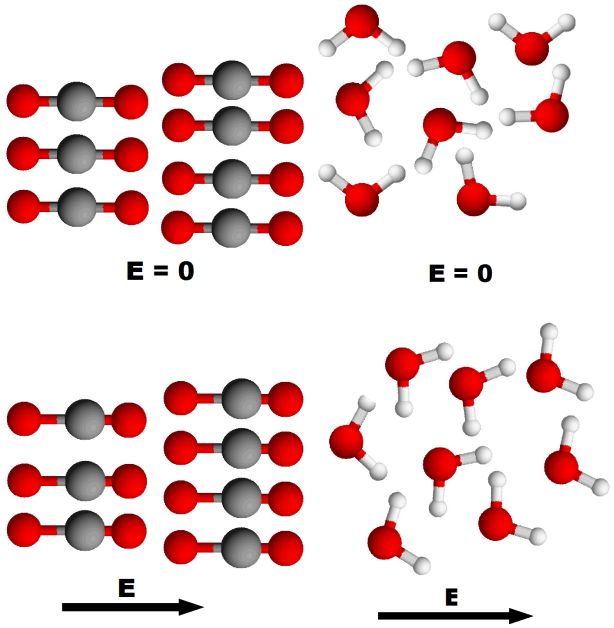

Figure 3.2: CO_2-molecules (left) as an example for non-polar constituents of a dielectric medium. On the right side the behaviour of polar molecules (H_2O) in an electric field **E** is sketched.

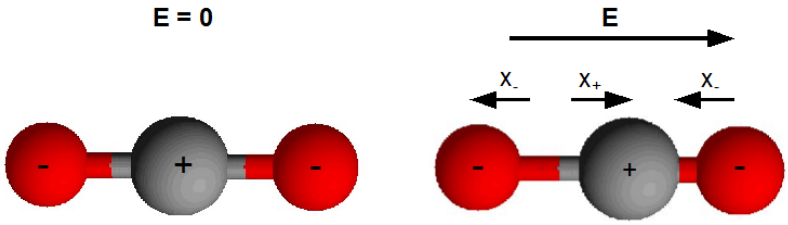

Figure 3.3: The behaviour of a CO_2-molecule with and without electric field **E**. According to their charges the masses will move in direction $x_{\pm}$.

an oscillator-equation (e is the elemental charge):

$$m\frac{d^2x}{dt^2} + \gamma x = F_x = eE_x \tag{3.7}$$

γ is the restoring constant between the moving particle and the centre, which includes the natural oscillator frequency ω_0 with $\gamma = m\omega_0^2$. A more sophisticated consideration of the induced polarisation for charged particles should additionally include a term describing the damping of the particle-movement due to radiation [7]. For a general understanding of the mechanism of induced polarisation the model (3.7) is sufficient.
An exponential ansatz with a harmonic external field $E_x = E_0 e^{iwt}$ leads to the solution of the oscillator-equation:

$$x = \frac{eE_x}{m(\omega_0^2 - \omega^2)}$$

With the definition of the induced dipole moment (eq.2.3), the polarisability α_{ind} for the considered system in a static field ($\omega = 0$) gets:

$$\alpha_{ind} = \frac{Qe}{m\omega_0^2} \tag{3.8}$$

This polarisation mechanism can additionally be separated by the particles that provoke the macroscopic dipole:

- electrons
- atoms/ions

The main difference between those particles is their mass. The electron rest mass is in the order of 10^{-31} kg, protons and neutrons in comparison have a rest mass of about 10^{-27} kg. It is obvious that this high mass difference will show a various behaviour in the considered model of an oscillator.
For an estimation of the natural frequency ω_0 of electrons (and therefore the resonance frequency (3.8)) one can think of a hydrogen atom. The restoring constant γ is determined by the Coloumb force of the nucleus:

$$\gamma = \frac{(Zq_e)^2}{4\pi\epsilon_0 R^3}$$

With the frequency ν_e

$$\nu_e = \frac{1}{2\pi} \cdot \sqrt{\frac{\gamma}{m}},$$

$Z = 1$, the electron charge $q_e = 1.6 \cdot 10^{-19}$ C, its rest mass of $9.1 \cdot 10^{-31}$ kg and the first Bohr radius $R_0 = 0.53 \cdot 10^{-10}$ m, one obtains a frequency in the order of 10^{15} Hz. Only considering the different rest mass (a factor 4 higher in the exponent) of protons and neutrons a simple estimation of their natural frequency gives about 10^{13} Hz.
Another essential point when looking at atoms or ions in a solid state is that the crystal lattice has to be included in the model. Due to the fact that two ions with mass $M_{A,B}$ in a lattice are connected to each other like a spring mass system one has to work with the reduced mass $M_r = \frac{M_A M_B}{M_A + MB}$.

3.2.2 Material with microscopic dipoles - Orientational polarisation

A different approach is necessary, if the material originally possesses microscopic dipole moments. If a field **E** is applied, additionally to the induced dipole moment the existing dipoles try to align to the field lines. For many microscopic dipoles one has to work with Boltzmann statistics. The number of dipoles with a certain angle θ to the field lines is:

$$n(\theta) = n_0 e^{-\frac{U}{kT}} \xrightarrow{(2.7)} n(\theta) = n_0 e^{-\frac{\mathbf{pE}\cos\theta}{kT}}$$

For normal fields $\mathbf{E}$ and temperatures T the exponent is small. Subsequently it is possible to approximate this value by [8]:

$$n(\theta) = n_0(1 + \frac{\mathbf{pE}\cos\theta}{kT})$$

To get the total polarisation $\mathbf{P}$ in a unit volume, one has to sum up the dipoles in the unit volume. For a lot of dipoles the sum can be evaluated as integral over the angular distribution (see [8]). The polarisability α_{orient} originated by the orientation of the microscopic dipoles becomes:

$$\alpha_{orient} = \frac{u^2}{3kT} \tag{3.9}$$

Equation 3.9 shows in contrast to (3.8) a temperature dependence, which is the main difference between polarisation originating from the orientation of microscopic dipoles compared to the induced polarisation.

The polarisability for an orientational polarisation was introduced under the assumption that the dipoles rotate freely as it is the case in some liquids and gases. In crystalline structures existing dipoles have less degrees of freedom due to interactions with their neighbours. The polarisability for a crystalline structure consisting of microscopic dipoles is given by [9]:

$$\alpha_{cryst} = \frac{2u^2}{kT}$$

The solid phase shows a 6 times higher polarisability compared to the liquid or gaseous phase.

3.3 Transition to macroscopic quantities - The Clausius-Mossotti equation

To get a smooth transition from microscopic to macroscopic dielectric quantities, one has to consider the macroscopic quantity relative permittivity ϵ_r, relating the field $\mathbf{E}$ and the polarisation $\mathbf{P}$ by:

$$\mathbf{P} = \epsilon_0(\epsilon_r - 1)\mathbf{E} \tag{3.10}$$

A detailed explanation is given in 3.4.

The Clausius-Mossotti equation connects the microscopic polarisability α with the macroscopic permittivity ϵ_r. It is valid for the Lorentz model of local field (see chapter 3.1.1). The polarisation $\mathbf{P}$ is expressed by the sum of N atoms of character i times their dipole moment $\mathbf{u}$ (2.8):

$$\mathbf{P} = \sum_i N_i \mathbf{u}_i \xrightarrow{(2.9)} \mathbf{P} = \sum_i N_i \alpha_i \mathbf{E}_{lok}(i)$$

By substituting $\mathbf{E}_{lok}$ with eq.3.6 and rearranging to $\mathbf{P}$ one gets:

$$\mathbf{P} = \frac{(\sum_i N_i\alpha_i)\mathbf{E}}{1 - \frac{1}{3\epsilon_0}(\sum_i N_i\alpha_i)}$$

With the definition (3.10) one gets finally (the calculation is given in appendix) to the Clausius-Mossotti equation:

$$\frac{\epsilon_r - 1}{\epsilon_r + 2} = \frac{1}{3\epsilon_0} \sum_i N_i \alpha_i \tag{3.11}$$

3.4 Permittivity and Susceptibility

With the Clausius Mossotti equation (3.11) the relation of microscopic polarisability α to the macroscopic quantity permittivity ϵ_r was found. Following this equation, the permittivity value of a medium is defined through the movement of induced or existing dipoles in the medium. As this movement is generally not without losses, the dipolar reaction to an electric field has in phase and out of phase components. Subsequently the relative permittivity is defined by its real (ϵ_r') and imaginary part (ϵ_r''), where j is the complex number:

$$\epsilon_r^* = \epsilon_r' - j\epsilon_r'' \tag{3.12}$$

The ratio of imaginary to real part is called loss tangent $\tan\delta$:

$$\tan\delta = \frac{\epsilon_r''}{\epsilon_r'} \tag{3.13}$$

It defines the dielectric loss of a material in an electric field. The real and imaginary part of the permittivity are connected through the Kramers-Kronig relations, which transfer the real part to the imaginary one and vice verse (P is the Cauchy principle part and ω the angular frequency of the field $\mathbf{E}$) [10]:

$$\epsilon_r'(\omega) = 1 + \frac{2}{\pi} P \int_0^\infty \frac{\omega' \epsilon_r''(\omega')}{(\omega')^2 - \omega^2} d\omega' \tag{3.14}$$

$$\epsilon_r''(\omega) = -\frac{2\omega}{\pi} P \int_0^\infty \frac{\epsilon_r'(\omega') - 1}{(\omega')^2 - \omega^2} d\omega' \tag{3.15}$$

In general the dielectric behaviour of a material is, equivalently to permittivity ϵ_r^*, described by its electric susceptibility χ^*, given by:

$$\epsilon_r^* = \chi^* + 1 \tag{3.16}$$

Only a constant factor divides these two quantities. It is a question of suitability which quantity is used. In this thesis the focus is given to permittivity, because it is the main physical information the HP[3]-Permittivity Probe deals with.
As generally used in this thesis one often speaks of relative permittivity ϵ_r.[2] It is a dimensionless number, defined as:

$$\epsilon_r = \frac{\epsilon}{\epsilon_0}$$

ϵ_0 is the vacuum permittivity with the value of $8.854 \cdot 10^{-12}$ [Fm^{-1}].

Table 3.1 summarises some common relative permittivity values. As shown in the table

[2] If not labelled with ϵ, the term "permittivity" is generally used for the relative value ϵ_r of a medium in this thesis.

Table 3.1: Relative permittivity ϵ'_r values for common natural ($Material_{nat}$) and technical relevant materials ($Material_{tech}$). Values within the first column are listed for a frequency of 1 MHz [11].

Material$_{nat}$ **[11]**	ϵ'_r	**Material**$_{tech}$ **[12]**	ϵ'_r
Air	1.0	Polytetraflourethylene	2.1
Water	80	Polystyrol	3.0
Ice	3.4	Polycarbonate	2.8
Mica	6.4	Polypropylene	2.2
Olivine	7.2	Aluminium Oxide (Al_2O_3)	9.8
Pyroxene	8.5	Paper	4 - 5.6
Quarz	4.5	Glass	3.8 - 8

most of the natural materials in solid state have relative permittivities around 5-10, whereas water has a significantly higher value of about 80. Consequently for geologic investigations the relative permittivity is a very good indicator for the presence of water.

3.4.1 Dependence on frequency and temperature

Frequency

The dependence of permittivity on frequency is obtained directly from the considerations in sec. 3.1. It is summarised for a homogeneous dielectric in fig. 3.4. For heterogeneous systems contributions of charges at interfaces contribute to an additional frequency dispersion (increasing of permittivity) at very low frequencies [13], which is discussed in sec. 4.1.1.1. Permanent dipoles contribute through their relaxations at low frequencies, whereas atoms, ions and electrons determine the characteristic behaviour (resonances) at high frequencies. The mathematical treatment of the frequency dependence of permittivity was established by Debye for polar liquids in 1929 [14]. It describes the relaxation region in the frequency behaviour (see fig. 3.4). Split in it's real and imaginary part, the permittivity is described as (see 3.5)

$$\epsilon'_r = \epsilon_\infty + \frac{\epsilon_{st} - \epsilon_\infty}{1 + (\omega\tau_0)^2} \tag{3.17}$$

$$\epsilon''_r = \frac{(\epsilon_{st} - \epsilon_\infty) \cdot \omega\tau_0}{1 + (\omega\tau_0)^2}, \tag{3.18}$$

where ϵ_{st} is the static permittivity, ϵ_∞ the value at high frequencies and τ_0 a characteristic relaxation time. Cole and Cole [15] expanded this model by introducing an empirical parameter α, with complex permittivity ϵ^*_r as (j is the complex number):

$$\epsilon^*_r - \epsilon_\infty = \frac{\epsilon_{st} - \epsilon_\infty}{1 + j(\omega\tau_0)^{1-\alpha}} \tag{3.19}$$

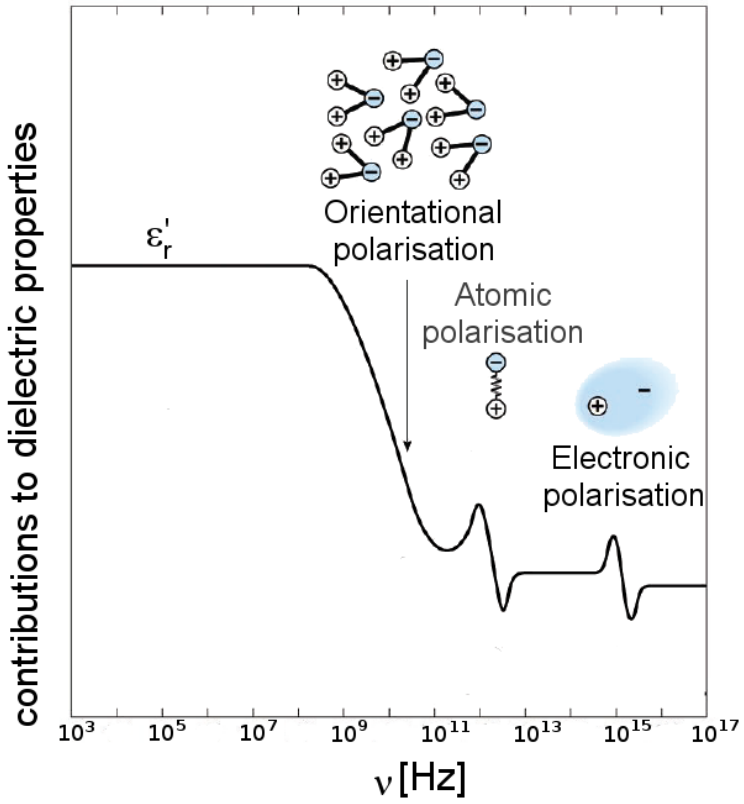

Figure 3.4: Different inner mechanism contribute to the value of permittivity in various frequency ranges. The picture has been modified from its original publication in [13].

In this model the real and imaginary part of permittivity are defined as [16]:

$$\epsilon'_r - \epsilon_\infty = \frac{1}{2}\,(\epsilon_{st} - \epsilon_\infty)[1 - \frac{\sinh(1-\alpha)\ln(\omega\tau_0)}{\cosh(1-\alpha)\ln(\omega\tau_0) + \cos(\frac{1}{2})\alpha\pi}] \tag{3.20}$$

$$\epsilon''_r = \frac{1}{2}(\epsilon_{st} - \epsilon_\infty)[\frac{\cos(\frac{1}{2})\alpha\pi}{\cosh(1-\alpha)\ln(\omega\tau_0) + \sin(\frac{1}{2})\alpha\pi}] \tag{3.21}$$

This consideration generally leads to a broader relaxation peak in the imaginary part of permittivity ϵ''_r and a softer decreasing of ϵ'_r (see fig. 3.5). For $\alpha = 0$ the Cole-Cole model reduces to Debye's formula (eq. 3.18). Figure 3.5 shows the Cole-Cole model for three different parameters α.

Davidson and Cole [17] modified (3.19) for their data to

$$\epsilon^*_r - \epsilon_\infty = \frac{\epsilon_{st} - \epsilon_\infty}{(1 + j(\omega\tau_0))^{1-\alpha}}$$

Later models for the frequency-behaviour of permittivity were derived by Havriliak-Negami [18] and Hill-Jonscher [19]. Including the basic $\frac{1}{1+j\omega\tau_0}$ function, these models introduce other parameters to better fit the obtained data.

Temperature

As for the frequency dependence of permittivity, the temperature dependence is a direct

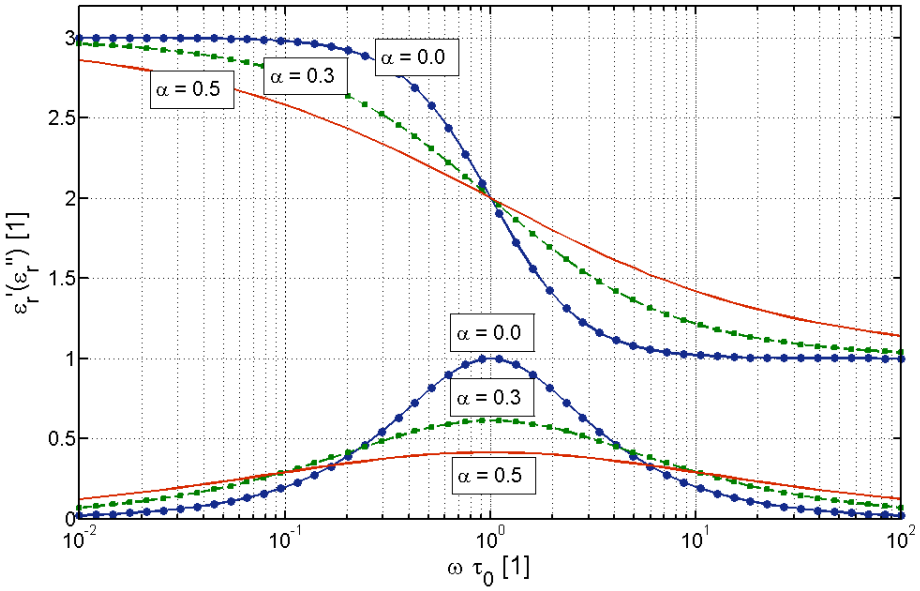

Figure 3.5: The Cole-Cole formalism (3.19) introduces a parameter α, which broadens the imaginary relaxation peak. Three selected values for α are plotted in the figure. For $\alpha = 0$ the Cole-Cole formalism reduces to the Debye equation 3.18.

result of the microscopic considerations in section 3.2, too. With the Clausius Mossotti equation (3.11) the microscopic behaviour is projected to macroscopic quantities.
In general, working with Boltzmann statistics for inner dipoles (see sec. 3.2.2) leads to a temperature dependence of the relaxation time constant τ_0 [20]

$$\tau_0 = \tau_\infty \exp\left(\frac{U}{kT}\right), \tag{3.22}$$

with the time constant at infinite temperature τ_∞, the dipole energy U, temperature T and Boltzmann's constant k.
The dependence of the permittivity value ϵ_r' to temperature T for non-polar dielectrics is defined with the temperature coefficient TK_e, obtained by derivation of (3.11) [21]:

$$TK_e = \frac{1}{\epsilon_r} \cdot \frac{d\epsilon_r}{dT} = -\frac{(\epsilon_r - 1)(\epsilon_r + 2)}{3\epsilon_r}\beta \tag{3.23}$$

TK_e in general behaves linear to the cubic expansion coefficient β of the material.
For polar dielectrics the considerations are more complex. Due to the temperature dependent polarisability (3.9), not only the volume expansion contributes with increasing temperature T [22].
In the book of Weissmantel and Hamann [23] an overview for the different material classes is given:

1. Polymers
   - ϵ_r increases, if T increases to values, where the material becomes more elastic

- further increasing of T (melting) causes dipole collisions and ϵ_r decreases

2. Low-molecular crystals with permanent dipoles
   - as principle behaviour TK_e is positive at low temperatures
   - characteristically there is a sudden increase of ϵ_r at order-disorder transitions
   - this sudden increase follows a negative TK_e
3. Ionic crystals
   - TK_e is positive, if ionic polarisability is dominant and negative, if electronic polarisability dominates

3.4.2 Effective permittivity models

In reality the permittivity ϵ_r of a measured medium is, especially for geophysical applications, an effective value ϵ_{eff}, in which multiple materials and phases are included. In general the frequency dependent models of section 3.4.1 could be used to estimate permittivities of the contributing materials. Various constituents contribute to the relaxation frequencies. Therefore by estimating the relaxation frequency of contributing materials, the abundance in the whole sample could be derived.[3]
Generally more direct models exist to determine sample constituents by their permittivities. Most of these models need the contributing volume fractions of materials and geometric information about the material. An overview of mixing-models for various shapes of constituents is given in Tinga et al. [24]. As for this work granular materials are most important, the consideration of spherical particles is sufficient.
Without the knowledge of any shapes within the sample, the lower and upper limits of effective permittivity $\epsilon^{\pm}_{eff}$ for a two component medium are obtained by the Hashin-Shtrikman boundaries [25]

$$\epsilon^{\pm}_{eff} = \epsilon_1 + \frac{f_2}{(\epsilon_2 - \epsilon_1)^{-1} + \frac{f_1}{3\epsilon_1}}, \tag{3.24}$$

where $f_{1,2}$ are the volume fractions and $\epsilon_{1,2}$ the permittivities of constituent 1 and 2.
As a simple model working with contributing volume fractions f_i, the Maxwell-Garnett model describes a linear dependence of effective permittivity ϵ_{eff} to the constituent permittivities ϵ_i of N materials:

$$\epsilon_{eff} = \sum_{i=1}^{N} f_i \epsilon_i \tag{3.25}$$

For a material with two components (spherical inclusions of material 2) the Clausius-

[3] If not mentioned otherwise, the effective value ϵ_{eff} is described by the real part permittivity values ϵ'_r of the material components

Mossotti formulation (3.11) yields to [26]:

$$\frac{\epsilon_{eff} - \epsilon_2}{\epsilon_{eff} + 2\epsilon_2} = f_1 \frac{\epsilon_1 - \epsilon_2}{\epsilon_1 + 2\epsilon_2},$$

The Maxwell-Wagner-Bruggeman-Hanai (MWBH) theory considers a host material (1) with embedded spheres (2) of volume fraction f_2 [27]

$$\frac{\epsilon^*_{eff} - \epsilon^*_2}{\epsilon^*_1 - \epsilon^*_2 (\frac{\epsilon^*_1}{\epsilon^*_{eff}})^{\frac{1}{3}}} = 1 - f_2. \tag{3.26}$$

This model works in comparison to the previous mentioned models with complex values of permittivity ϵ^*_r.

Hanai and Sekine [28] extended this model for suspensions of two kind of particles.

Beside these mathematically based models empirical models like the Lichtnecker-Rother formula

$$\epsilon^*_{eff} = [\sum_{i=1}^{N} f_i {\epsilon_i}^{*\gamma}]^{\frac{1}{\gamma}} \qquad (-1 \leq \gamma \leq 1) \tag{3.27}$$

introduce material dependent paramter (γ) to describe a multi-constituent sample.

Olhoeft and Strangway [29] introduced an empirical equation to describe the dependence between bulk density and real part permittivity, where their original studies go back to the evaluation of data from the Apollo missions.

For the work with sand/ice-mixtures Stillman et al. [30] used for their real part permittivity data a model similar to the Lichtnecker-Rother formula

$$\epsilon_{eff}^{\frac{1}{\gamma}} = f_1 \epsilon_1^{\frac{1}{\gamma}} + f_2 \epsilon_2^{\frac{1}{\gamma}} + f_3 \epsilon_3^{\frac{1}{\gamma}}, \tag{3.28}$$

in which they took one phase as sand, one as ice and the third as air. For their data they obtained a value of 2.7 ± 0.3 for γ.

For the determination of water content in a geologic sample, existing models have to be adapted especially at low frequencies (see e.g. [31] or [32]). For higher frequencies (20 MHz - 1 GHz) Topp's relation is commonly accepted to describe the effective real part permittivity ϵ_{eff} (f_w is the volumetric water content):

$$\epsilon_{eff} = 3.03 + 9.3 f_w + 146 f_w^2 - 76.7 f_w^3 \tag{3.29}$$

Knight and Nur [33] found for lower frequency ranges (60 kHz - 4 MHz) an empirical power law for the angular frequency (ω) dependence of the real part permittivity ϵ'_r of water bearing sandstones:

$$\epsilon'_r = A\omega^{-\alpha} \quad (0 < \alpha < 0.4) \tag{3.30}$$

A and α are saturation and material dependent parameters.

Including very low frequencies, Rusiniak [34] related the real part effective permittivity ϵ_{eff} of some solid water bearing samples to the sample porosity ϕ_s, water volume fraction f_w and the permittivity of rock (ϵ_{ro}) and water ϵ_w by:

$$\epsilon_{eff} = f_w \phi_s \epsilon_w + (1 - \phi_S)\epsilon_{ro}$$

CHAPTER 4

Real media - Maxwell's Equations

In the previous chapters, the physical properties of perfect insulators have been discussed. In the following chapter the influence of conductivity σ within a dielectric medium is considered. Therefore the Maxwell equations are listed and consequences for the measurement are derived.

4.1 Maxwell's equations

The Maxwell equations (eq. 4.1 - eq. 4.4) connect the electromagnetic properties of a material to the electric- $\mathbf{E}$ and magnetic-fields $\mathbf{H}$:

$$\nabla \times \mathbf{E} = -\frac{\partial \mathbf{B}}{\partial t} \tag{4.1}$$

$$\nabla \times \mathbf{H} = \frac{\partial \mathbf{D}}{\partial t} + \mathbf{j} \tag{4.2}$$

$$\nabla \cdot \mathbf{D} = \rho \tag{4.3}$$

$$\nabla \cdot \mathbf{B} = 0 \tag{4.4}$$

$\mathbf{j}$ is the current density, ρ the charge density. The dielectric displacement $\mathbf{D}$ and the magnetic induction $\mathbf{B}$ are connected to the fields $\mathbf{E}$ and $\mathbf{H}$ by

$$\mathbf{D} = \epsilon \mathbf{E} \tag{4.5}$$

$$\mathbf{B} = \mu \mathbf{H}, \tag{4.6}$$

with the permittivity ϵ and permeability μ.

4.1.1 Determination of dielectric properties

Equation 4.2 includes for the total current density **J** contributions from dielectric displacement **D** (bound charges) as well as from free charges (**j**). Considering a harmonic field **E** (**E** (t) = $E_0 e^{i\omega t}$), with Ohm's law and relation (4.5), the total charge density **J** is expressed by

$$\mathbf{J} = -\epsilon \frac{\partial \mathbf{E}(t)}{\partial t} + \mathbf{j} \tag{4.7}$$

$$= (-i\omega\epsilon + \sigma)\mathbf{E}(t) \tag{4.8}$$

$$= \tilde{\sigma}\mathbf{E}(t), \tag{4.9}$$

with the complex term $\tilde{\sigma}$. Indicating permittivity and conductivity as complex quantities, the current density can be written as:

$$\Re\{\mathbf{J}\} = \sigma' + \omega\epsilon''$$
$$\Im\{\mathbf{J}\} = \sigma'' - \omega\epsilon'$$

The total current density **J** of a medium is described through both quantities, since (dielectric) polarisation as well as free charges contribute (see (4.3)). Thus permittivity and conductivity are connected to each other:

$$\sigma' \leftrightarrow \omega\epsilon'' \tag{4.10}$$

$$\sigma'' \leftrightarrow \omega\epsilon' \tag{4.11}$$

In the measurement of dielectric properties both quantities can only be extracted by the frequency dependence of ϵ^*. A material is equivalently described by its complex permittivity ϵ^* or its complex conductivity σ [35], but obviously the information is reduced to a certain quantity, if conductive or dielectric phenomena are the main contributing part (conductors, insulators).
Based on (4.9) the material properties can be determined. Ohm's law yields for the comparison of the vacuum value $\tilde{\sigma}_0$ to a material value $\tilde{\sigma}_m$:

$$\frac{\tilde{\sigma_0}}{\tilde{\sigma}_m} = \frac{\frac{\mathbf{j}_0}{\mathbf{E}_0}}{\frac{\mathbf{j}_m}{\mathbf{E}_m}} =: \frac{\xi_0}{\xi_m}$$

With the definition of $\tilde{\sigma}$ in (4.9) and the absence of free charges ($\sigma_0 = 0$) in vacuum one gets

$$\begin{aligned}\frac{\xi_0}{\xi_m} &= \frac{-i\omega\epsilon_m + \sigma_m}{-i\omega\epsilon} \\ &= \frac{-i\omega\epsilon_0(\epsilon_{r,m} + \frac{\sigma_m}{i\omega\epsilon_0})}{-i\omega\epsilon_0} \\ &= \epsilon_{r,m} + \frac{\sigma_m}{i\omega\epsilon_0},\end{aligned}$$

where contributions from the imaginary parts of conductivity σ'' and permittivity ϵ_r'' are not considered for better presentation. Thus σ_i and $\epsilon_{r,i}$ (i $\in$ {m,0}) represent the real parts σ' and ϵ_r'. The imaginary parts are obtained by using the relation in (4.11).
The sample permittivity $\epsilon_{r,m}$ and its conductivity σ_m are finally expressed by the real and imaginary parts:

$$\epsilon_{r,m} = \Re\{\frac{\xi_0}{\xi_m}\} = \Re\{\frac{\frac{\mathbf{j}_0}{\mathbf{E}_0}}{\frac{\mathbf{j}_m}{\mathbf{E}_m}}\} \tag{4.12}$$

$$\frac{\sigma_m}{\omega\epsilon_0} = \Im\{\frac{\xi_0}{\xi_m}\} = \Im\{\frac{\frac{\mathbf{j}_0}{\mathbf{E}_0}}{\frac{\mathbf{j}_m}{\mathbf{E}_m}}\} \tag{4.13}$$

For technical evaluations it is more convenient to describe $\epsilon_{r,m}$ and σ_m by means of complex current I^* and voltage U^*, which are connected by Ohm's law (with complex impedance $Z^* = |Z|e^{i\phi}$):

$$U^* = Z^* I^*$$

Expressing $\mathbf{j}$ and $\mathbf{E}$ by I and U eq. 4.13 gives an expression for ϵ_r and σ_m:

$$\epsilon_{r,m} = \Re\{\frac{Z_0^*}{Z_m^*}\} \tag{4.14}$$

$$= \frac{|Z_0|}{|Z_m|}\cos(\phi_0 - \phi_m) \tag{4.15}$$

$$\frac{\sigma_m}{\omega\epsilon_0} = \Im\{\frac{Z_0^*}{Z_m^*}\} \tag{4.16}$$

$$= \frac{|Z_0|}{|Z_m|}\cdot\sin(\phi_0 - \phi_m) \tag{4.17}$$

4.1.1.1 Frequency spectrum of real media

The conductivity of a medium plays an important role when investigating its dielectric properties, due to the fact that conductivity σ and permittivity ϵ are connected to each other as shown in (4.11). Especially for low frequencies the measurement of the imaginary part permittivity ϵ_r'' is influenced by conductivity σ (ϵ_r'' goes with ω in relation (4.11))
The contribution of real part conductivity σ' to the real part ϵ'-values is manifested in the Maxwell-Wagner effect. This effect describes high effective permittivity values ϵ_{eff} for low frequency measurements (at high frequencies dielectric phenomena are dominant (relation 4.11)). It results from the variation in phase-conductivity between the constituents of a composite material (e.g. dielectric grains in a conductive fluid). The Maxwell-Wagner effect is especially important in systems with water abundances [36]. Microscopically this low frequency effect is described by so called "*interfacial polarisation*". This effect describes polarisation contributions originating from space charges located at phase boundaries [37]. Figure 4.1 shows the effect of the two mentioned phenomena on the general frequency behaviour of a dielectric material. It has to be noted that an increase of real part permittivity

ϵ_r' is not necessarily connected to an increase of imaginary part ϵ_r'', since the real part increase originates from permittivity contrast in various phases of a heterogeneous medium, whereas imaginary values increase due to whole sample (effective) conductivity. Nevertheless in some cases these phenomena go together. As an example, the conductivity gradient is high in granular material surrounded by liquid water ($\Delta\epsilon_r' \approx 70$). In this case the sample conductivity σ is increased too, resulting from additional conduction paths due to the liquid phase. Thus, the ϵ_r' and the ϵ_r'' values at low frequencies will be higher. To mathemati-

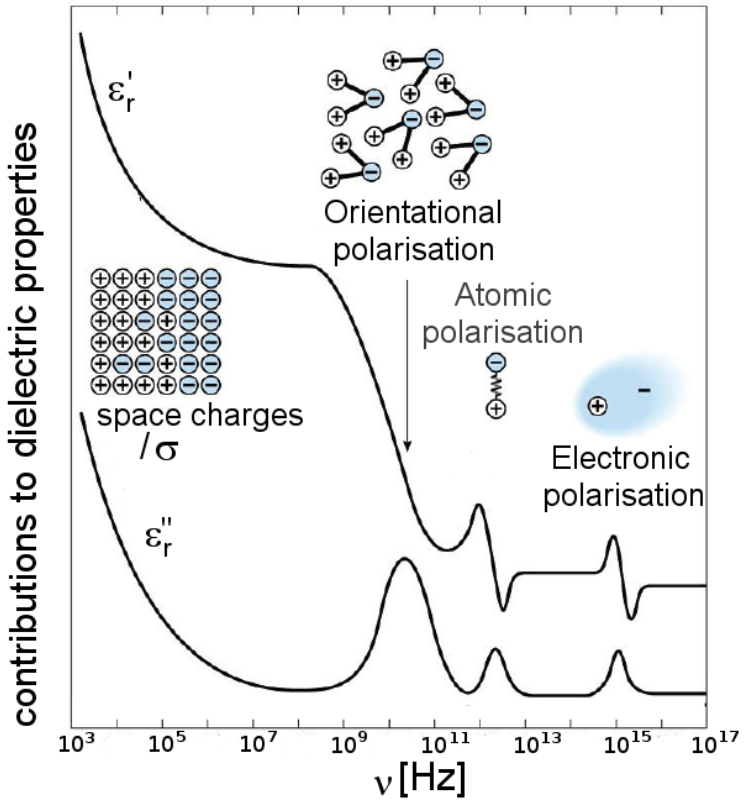

Figure 4.1: The material contributions to the dielectric properties (ϵ_r',ϵ_r'') for real media including conductivity σ (modified from [13]).

cally describe the conductive phenomena for complex part permittivity ϵ_r'' a representing term has to be added to the frequency model (see e.g. [38]). Exemplary, including the dc conductivity σ_0, the Cole-Cole function (3.19) gets:

$$\epsilon_r^* - \epsilon_\infty = \frac{\epsilon_{st} - \epsilon_\infty}{1 + j(\omega\tau_0)^{1-\alpha}} + j\frac{\sigma_0}{\omega\epsilon_0} \tag{4.18}$$

4.1.2 Electric potential for a Wenner-α array

With the Maxwell equations (4.1-4.4) the potentials within any geophysical arrays can be calculated. Since PP is geometrically designed as Wenner array type "α" (see sec. 5.2 and sec. 6.4) the following considerations focus on this geometry. As being typical for

geophysical applications, the following calculations are performed in a quasi-static approach. Thus, introduced quantities are described by their amplitudes.
Considering the continuity equation, relating current density $\mathbf{j}$ to the time derivative of charge density ρ,

$$\nabla \mathbf{j} = -\frac{\partial \rho}{\partial t}$$

and Gauss' law, one obtains for the volume integral

$$\int_V \nabla \mathbf{j} \; d\mathbf{V} = -\int_V \frac{\partial \rho}{\partial t} \; d\mathbf{V}$$
$$\int_S \mathbf{j} \; d\mathbf{S} = -\frac{dQ}{dt}$$

Inserting Ohm's law (eq. 4.9) and calculating the surface integral for a half sphere, what simulates a geophysical surface measurements, one gets for the field $\mathbf{E}$

$$\int_S \sigma \; \mathbf{E} \; d\mathbf{S} = I$$
$$and$$
$$\mathbf{E} = \frac{I}{2\pi\sigma r^2},$$

respectively, and finally for the potential U:

$$U = \int_r^\infty \mathbf{E} \; d\mathbf{r} = \frac{I}{2\pi\sigma r} \tag{4.19}$$

Equation 4.19 is the general expression for a point source. For a Wenner array, the potential difference between two points (receiving electrodes (M,N)) is determined. The potential there originates from two source potential electrodes (A,B) (see fig. 5.5). The source potential of transmitter A and B adds at the receiving points M and N (superposition):

$$U_A = U_{A,M} + U_{A,N}$$
$$U_B = U_{B,M} + U_{B,N}$$

For the relevant potential difference ΔU_{MN} one obtains with (4.19)

$$\Delta U_{MN} = \frac{I}{2\pi\sigma}\left(\frac{1}{r_{A,M}} + \frac{1}{r_{B,M}} - \frac{1}{r_{A,N}} - \frac{1}{r_{B,N}}\right)$$

For the Wenner-α configuration (equidistant electrodes) with electrode distance a

$$r_{A,M} = -r_{B,N} = a$$
$$r_{A,N} = -r_{B,M} = 2a,$$

eq. 4.1.2 reduces for the measured potential ΔU_{MN} to:

$$\Delta U_{MN} = \frac{I}{2\pi\sigma a} \tag{4.20}$$

CHAPTER 5

Measurement of permittivity

To determine the sample permittivity experimentally, various techniques exist for different frequency-ranges. In the book of Weißmantel and Hamann [39] measurement techniques are listed as shown in tab. 5.1.

As shown in sec. 4.1 (eq.4.17) the determination of permittivity ϵ_r^* generally reduces to the determination of the unknown complex impedance Z^* of a test sample and a reference value without sample (geometries are supposed to be known). In the most straight forward case of a capacitor filled with the sample under test, the permittivity ϵ_r^* is determined by

$$\epsilon_r^*(\omega) = \frac{1}{j\omega C_0 Z^*(\omega)}, \tag{5.1}$$

where ω is the angular frequency and C_0 the capacity of the empty capacitor.
In the following sections the basic principles of the measurement techniques presented in tab. 5.1 are explained. Additionally to this classification the method of determining permittivity with direct measurement methods of sampling current I to applied voltage U is explained. This method is suitable for a very broad frequency range (see [40]) by adjusting its electrical

Table 5.1: `Various measurement techniques of permittivity are differentiated for their applicable frequency ranges according to [39].`

Technique	**Frequency range**
AC-bridges	10^{-2} - 10 MHz
resonant-circuits	10 - 700 MHz
resonant-cavities	10^9 - 10^{11} Hz
optical methods	$>10^{12}$ Hz

components.
At first the basic difference between the measurement in time- and frequency-domain is shown.

5.1 Time and frequency domain measurement

In general, time and frequency domain measurement techniques are equivalent [41]. Moreover the two techniques are principally convertible by mathematical transformation (e.g. Fourier transformation). Figure 5.1 shows the principle of (a) time domain and (b) frequency domain spectroscopy. In the time domain the polarisation decay curve $P_0(t)$ of a transmitter signal is determined. When applying an electromagnetic (EM)-pulse function to a material, the inner dipole moments (see sec. 3.2) will be oriented in a specific way. The characteristic signal features are a sudden increase of polarisation P_{inf} subsequently after applying, and the maximum amplitude P_0, which is asymptotically reached. After switching off the input signal, this characteristic behaviour is repeated with inverted sign.

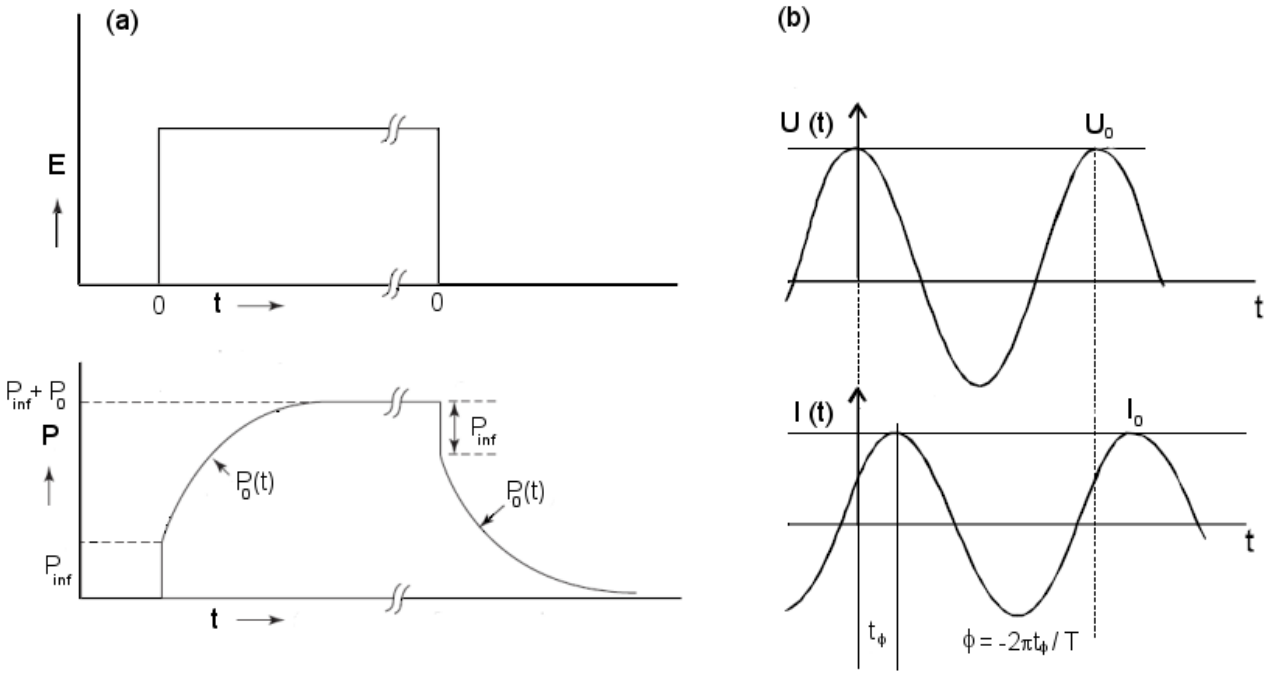

Figure 5.1: The basic measurement principles of (a) time- and (b) frequency-domain techniques. In time domain an EM-pulse function **E** is applied to the material and the polarisation decay curve $P_0(t)$ is determined. P_{inf} symbolises a sudden increase of the material polarisation **P** immediately after the pulse is applied, P_0 is the amplitude reached within the asymptotic increase of polarisation. In frequency domain the signal amplitude I_0 and phase shift t_ϕ of a transmitted voltage signal U(t) is measured.

In practice this change in polarisation is determined by measuring the decay of the signal originating from the induced sample currents.
In frequency domain an EM-wave with fixed frequency and amplitude is transmitted into the material. This transmitted EM-wave is characterised by phase ϕ and amplitude U_0 of the signal $U(t)$. Depending on frequency and material properties the EM-wave will be damped and shifted in phase. Measuring the amplitude I_0 and phase shift $\Delta\phi$ of the sample current, the material impedance can be determined by

$$Z^* = \frac{U^*}{I^*}, \tag{5.2}$$

where * describes the complex (amplitude and phase) values of the input signal voltage $U(t)$ and the sample current $I(t)$.

5.2 Impedance measurement techniques

There are various techniques to measure the impedance of a test-sample in a specified frequency range. In general bridge and direct methods are most suitable for low frequency measurements, whereas reflection methods are used for very high frequencies.

Bridges
The basic measurement principle of a balancing bridge is sketched in fig.5.2. One or several

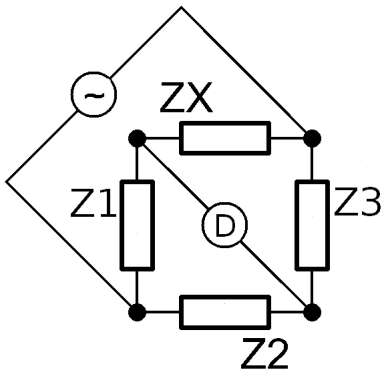

Figure 5.2: The basic scheme of a balancing bridge.

of the known impedances $Z_{1,2,3}$ are changed until the voltage-detector D is nulled. The unknown impedance Z_x is then determined by:

$$Z_x = \frac{Z_3}{Z_2} \cdot Z_1$$

Various bridge-type measurement systems including RC-elements are available [42, 43] for the determination of the dielectric sample parameters.

Resonant Methods
The basic circuit for the determination of an unknown impedance Z_x - respectively in

fig.5.3 the unknown resistance R_x and -inductance L_x - is drawn in fig.5.3. The unknown impedance is determined in the LC-circuit by tuning the capacitor C_i to resonance. In knowing the adjusted capacity the unknown impedance Z_x is determined through the resonance angular frequency ω_0, defined as

$$\omega_0 = \frac{1}{\sqrt{L_x C_i}}.$$

Exemplary the permittivity of a sample could be determined by putting in a second capacitor parallel to the tunable one. By comparing the impedance values with empty to filled capacitor the dielectric properties could be evaluated. For measurements in a frequency

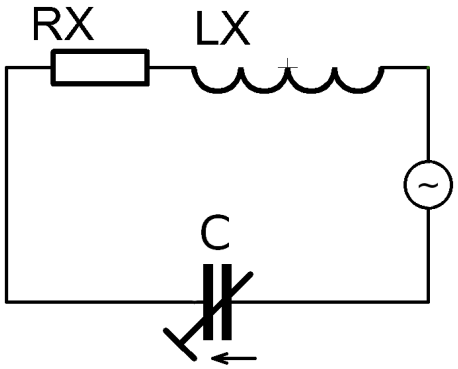

Figure 5.3: The basic scheme of measuring impedance by a resonant LC-circuit.

range between 10^9 Hz and 10^{11} Hz the sample is put in a resonance cavity. In this case the sample permittivity is determined by the shift and damping of resonance frequency [39]. E.g. for a cubically shaped ideal resonant cavity the Eigen-frequencies ν_{nmp} are defined by [44]

$$\nu_{nmp} = \frac{1}{\sqrt{\epsilon_0 \epsilon_r \mu_0 \mu_r}} \cdot \sqrt{\sum_{i=1}^{3} (\frac{m_i}{2a_i})^2},$$

with the cavity dimensions a_i and the values $n_i = 0, 1, 2, ...$ (at least one $n_i > 0$), which describe the mode of the EM-wave. Thus if a dielectric material with $\epsilon_r > 1$ is placed into the cavity, the Eigen-frequencies will shift compared to the empty resonator ($\epsilon_r \approx 1$).

Direct Methods

The direct measurement of the unknown sample impedance $Z_x = Z_s$ by recording U^* and I^* may be the easiest way to determine the material properties. Ohm's law yields

$$Z_s^* = \frac{U_1^*}{I_s^*} = \frac{U_1^*}{U_s^*} R_x, \tag{5.3}$$

where R_x is a known resistance to obtain the sample voltage U_2. The Novocontrol impedance spectrometer used for this work (see 7.3) in principle works as a direct method (see fig.5.4). A sinusoidal voltage U_1^*, which is measured by the first channel of a vector analyser, is put on the sample capacitor. The sample currents I_s^* are measured by means of a current-to-voltage conversion. Then the sample voltage U_2^* is determined with the second channel

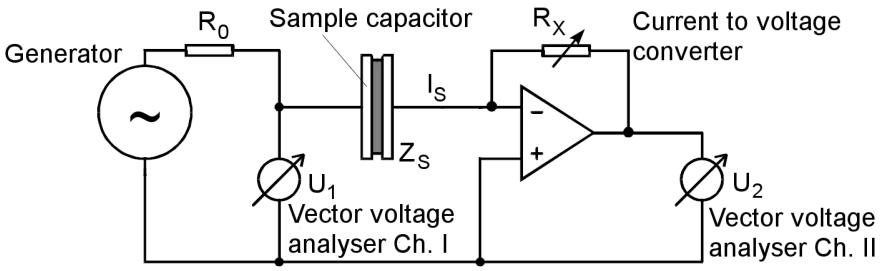

Figure 5.4: The direct measurement method of the impedance spectrometer used in this work. The figure is taken from [45].

of the vector analyser. Using eq. 5.3 one obtains the sample impedance Z_s^*. Sometimes this method of directly measuring the excitation voltage U_1^* and the sample currents I_s^* by means of current-to-voltage conversion is referred as a auto-balancing bridge method [40], because the operational amplifier balances its input signals.

For geophysical applications direct measurement systems are mostly realised as 4-point measurement devices. Two electrodes are used to generate a current in the sample under test, whereas two other electrodes are used to acquire the differential voltage ΔV as drawn in fig.5.5. The use of four electrodes instead of only two suppresses electrode polarisation effects.

In general there are various possibilities for arranging the four electrodes, each of them showing advantages and disadvantages (see [46]). As the permittivity probe (PP) used in this work is geometrically designed as a Wenner-α array [47], this concept is shown in fig.5.5. Four electrodes are located equidistant. The two outer electrodes (A, B) inject a current I in the test sample. The inner electrodes (M, N) measure the voltage difference ΔV. As for geophysical applications needed, the apparent resistivity ρ_a of the sample under test is then defined as [49]

$$\rho_a = K\frac{\Delta V}{I_s}, \tag{5.4}$$

The factor K is dependent on the array geometry and calculated to be $K = 2\pi a$ for the Wenner-type-α (see (4.20) in sec. 4.1.2). For the determination of the complex sample impedance Z^* a phase sensitive detector is used to compare the transmitted and received signal. In geological applications the electrode distance a is varied for vertical sounding of the underlying medium, because this distance determines the origin of the measurable signal. For a Wenner array this so called "effective depth" of investigation z_e is calculated to be [50]:

$$z_e = 0.519 \cdot a \tag{5.5}$$

In general the Wenner-arrangement shows high vertical resolution, high signal to noise ratio, but weak lateral resolution compared to arrays of other geometries [46].

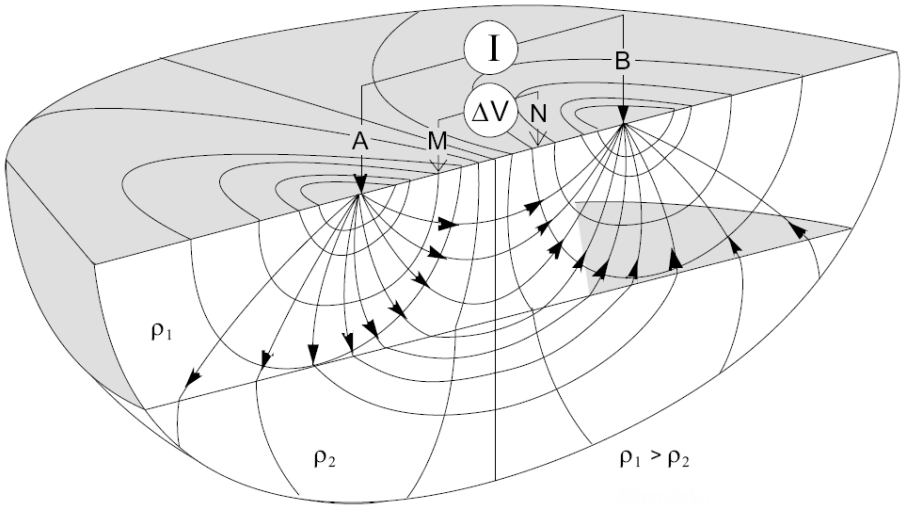

Figure 5.5: In the Wenner-α array [47] four electrodes are equidistant located. The two outer electrodes A/B generate a current I. The inner electrodes M/N measure the voltage difference ΔV. This figure originally was published in [48].

Optical Methods

Optical methods are used for operating frequencies $>10^{12}$ Hz. For these methods the determination of permittivity ϵ_r^* is achieved by the determination of the refractive index n^* of a test medium. Especially for non-ferromagnetic materials (magnetic permeability $\mu_r \approx 1$) the relation

$$\epsilon_r^* \approx n^2$$

holds. A more detailed explanation of this method is given in [51].

CHAPTER 6

The HP^3-Permittivity Probe

In this chapter the properties and function of the HP^3 (**H**eat Flow and **P**hysical **P**roperties **P**ackage)-Permittivity Probe will be explained in more detail. In the first sections the applicability of a permittivity-instrument within a Mars mission and the special requirements of a space instrument are discussed. After that details of the HP^3-Permittivity Probe are presented.

6.1 Requirements for a space instrument

Special technical requirements are applied to an instrument designed for a space mission. The following aspects have to be considered:

1. Local environmental conditions: low temperature, thermal cycling radiation, atmospheric pressure, gravitation
2. Distance and transport: long duration of transport, forces at launch and landing
3. In general: energy support, long term control, pollution control and planetary protection.

Even Mars, which is known as the most earth-like planet, shows big differences in its characteristics compared to the Earth (tab. 6.1). These facts have to be considered in planning a space instrument for Mars.

The key points for the instrument's design are considerations on minimal acceptable power and mass of the instrument. Space instruments have to be designed as lightweight as possible, because each kg of mass influences the costs drastically (see e.g. [52]). In tab.6.2 the mass budgets of some selected lander missions are listed. As shown, only a small amount

Table 6.1: Comparison of Earth's main characteristics to Mars.

	Earth	**Mars**
equatorial radius [km]	6378	3394
mass [10^{24} kg]	5.97	0.64
mass (normalised to earth)	1	$\approx$ 0,1
distance to sun [10^6 km]	$\approx$ 150	$\approx$ 228
gravitational acceleration [ms^{-2}]	9.81	3.71
mean surface temperature [K]	$\approx$ 295	$\approx$ 233
max. temperature gradients [K]	$\approx$ 100	$\approx$ 160
atmospheric pressure [mbar]	1000	7

of the total lander mass is provided as scientific payload. The main part of the total mass is needed for heat protection, power supply and operational hardware.

The long-term power supply for a Mars mission is a critical task. The best long-term

Table 6.2: Mass budget for some selected planetary landers. Values taken from [53].

	Viking	**Beagle2 [54]**	**Huygens**	**Phoenix**
target body	Mars	Mars	Titan	Mars
total mass [kg]	1185	69	318	680 [55]
scientific payload [kg]	100	9	44	55 [56]
landing velocity [ms^{-1}]	2.4	16.7	4.7	1.6

power supply is guaranteed by solar and radio nucleid systems, whereas batteries and fuel cells provide a rather short-term lifetime (see [57, 58]). The available power systems - depending on resources and mission target body - influence the possible instrument's power consumption.

Another point which has to be considered in the instrument design is its mechanical stability. For example at launch, depending on the launch vehicle, several g (e.g. 4.5 g for Ariane 5 with maximum payload of 600 kg, [59]) peak acceleration is reached. Additionally at launch big structural and acoustic vibrations have to be taken into account. The peak deceleration is reached in the spacecraft landing phase. The landing velocities of some selected missions are listed in tab.6.2.

Shielding against solar-radiation has to be considered in the design as well as protection against dust and other pollution of the scientific instrument. Especially for a Mars mission strict planetary protection requirements have to be taken into account [60]. Planetary

protection generally treats the protection of the natural environment of planets. Their environment should not be influenced by pollution originating from space missions. Thus, fabrication has to be as clean as possible and not permanently sealed parts have to be controllable at any time.
The points mentioned above have to be considered for each instrument component (mechanical, electronic,...). Therefore every component has to be officialy qualified for a space mission.

6.2 A permittivity instrument on Mars

The instrument concept of a permittivity probe for Mars was proposed frequently in the past [35,61–63]. Nevertheless, with the TECP (**T**hermal and **E**lectrical **C**nductivity **P**robe) - instrument on Phoenix [2] only one instrument was successful on-board a Mars mission.
In general, the basic interests of a permittivity instrument within a Mars mission can be summarised as:

- Characterisation of the electrical properties of the surface material,
- determination of stratigraphic variations (e.g. inclusions, layers with varying geology),
- detection of water and ice, and
- detection of electromagnetic phenomena.

As listed above, one major aim of a permittivity instrument on Mars would be the in-situ characterisation of the electrical properties of regolith [4]. This would increase the general knowledge about yet poorly known electrical properties of Mars. Moreover it would provide ground truth data for orbiting instruments [64]. The precise knowledge of surface and sub-surface electrical parameters determine the electromagnetic wave propagation in and around the planet, and therefore would provide clues to the basic inner structure [65].
As another important tool a permittivity probe would be able to determine stratigraphic variations of subsurface layers, if it is employed in a penetrating device, or the electrode configuration is changeable [66]. This could probably reveal potential water-bearing layers, which are supposed to exist at decimeter depths even at mid latitudes of Mars [67]. Additionally the depth of the weathering layer on the Martian surface, altered by solar and micrometeoritic bombardment, could be determined. This weathered layer is supposed to work as shield against particle radiation. It determines the depth, where living systems can exist [68].
As described in section 4.1.1.1, abundances of water drastically influence the electrical

[4] The fine grained material which is commonly observed as a first layer on top the surface of solid bodies (except the so called "icy" bodies) in the solar system is called *regolith*.

properties of a material. Therefore a device determining the electrical characteristics of a medium is a strong indicator for water deposits. Furthermore diurnal and seasonal variations of the local moisture content are detected easily. This provides unique information about the state, abundance and cycle of water on the whole planet [2].
In a passive mode, a permittivity probe is able to determine electromagnetic events on its target body. Especially on Mars the detection and quantification of triboelectric phenomena connected to local dust storms would provide yet unknown information [69].
Furthermore the permittivity value is a possible measure for the sample bulk density (e.g. empirical formulations by Olhoeft [29] or WenZhe Fa [70]), which is an important parameter in the data evaluation for other experiments like the measurement of heat flow [71].

6.3 The HP^3-instrument

The HP^3 (**H**eat Flow and **P**hysical **P**roperties **P**ackage) sensor suite was initially intended to be part of the ExoMars Humboldt surface station [72]. Its scientific objectives were to characterise the physical properties of the Martian subsurface and to determine the planetary heat flow. After the cancellation of the surface station, it was decided to develop the HP^3 instrument further, until a laboratory model with a high proto-flight maturity level was achieved.
The current design of the HP^3 instrument includes a heat flow-probe, thermal sensors, accelerometers and a permittivity probe. Initially, also a supplementing gamma-ray backscatter densitometer [73] was planned to be part of the instrument package. The instrument suite is expected to explore the Martian subsurface by means of a mole introduced by self penetrating mechanism.
A sketch of the HP3-instrument including its four subsystems is presented in fig. 6.1.

Scientific measurements will be performed during penetration into the ground and in steady state at the final sub-surface position. Details concerning the thermal investigations within the instrument package are presented in Spohn et al. [71]. The following sections focus on the HP^3-Permittivity Probe.

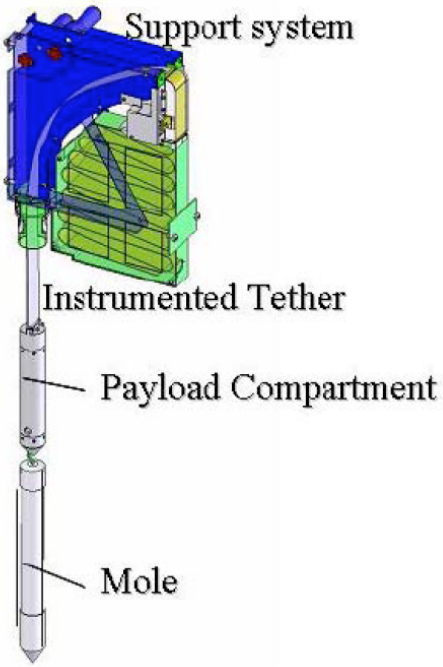

- The mole for ground penetration,
- the payload compartment housing scientific instruments and their front end electronics,
- the instrument-tether for power supply and data link (including thermal sensors) and
- the support system including the back end electronics and power subsystem

Figure 6.1: A scheme of the HP^3 instrument.

6.4 Permittivity Probe measurement principle

The measurement principle follows the concept of a classical Wenner-array type α (see section 5.2). The application of a permittivity probe for use in space was first suggested by Grard [66], who proposed instruments working on the mutual impedance concept. The HP^3-Permittivity Probe principally follows this concept (fig.6.2). Two transmitting electrodes

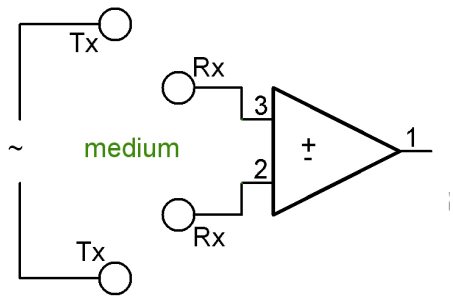

Figure 6.2: The HP^3-PP measurement following a concept which was first proposed by Grard [63] for space applications.

(Tx) apply an electric field into the investigated medium, whereas two receiving electrodes (Rx) measure the potential difference. Comparing the measured potential-difference to the source potential, the amplitude difference and the phase shift of the injected signal are determined. This leads to the electrical properties of the sample under test (see sec. 5.1)

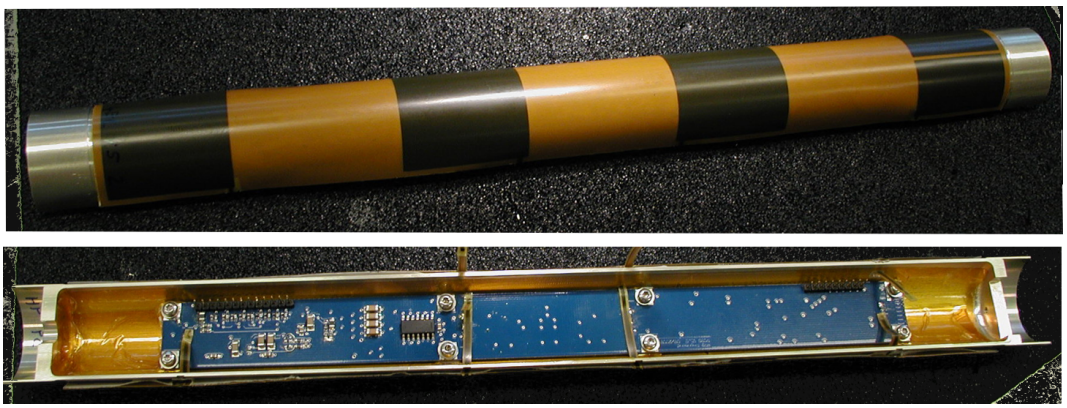

Figure 6.3: A picture of the HP^3-Permittivity Probe. The main electrodes can be seen (black). Underneath the PP front end electronics within the payload compartment is presented.

6.5 Instrument description

The HP^3-Permittivity Probe (PP) is built as a follow up development of an ESA (**E**uropean **S**pace **A**gency) prototype [74]. The instrument requirement's were set for its initial target body Mars:

- Determination of ice/water content of the regolith as a function of depth,
- determination of permittivity and conductivity of the regolith as a function of depth,
- recognition of the subsurface stratigraphy along the penetration path.

The PP is designed as a small and lightweight tool. A picture of the HP^3-PP design is shown in fig. 6.3. In the lower half of the picture the PP-front end electronics is shown in the payload compartment. In black the main electrodes - located equidistantly in a Wenner-α array configuration (see section 5.2) - are shown.
The characteristic parameters of the instrument and the payload compartment (PC) are listed in tab. 6.3. As listed, the Permittivity Probe needs very low power. The frequency range of 1 to 20,000 Hz is comparably high in relation to the successful permittivity-instrument on the Huygens-probe, which measured the electrical properties of Titan's atmosphere and its ground [1]. In comparison to the Permittivity Probe on the Rosetta-lander Philae [3], the HP^3-PP provides the same frequency range. A general comparison of the instrument mass and power consumption to similar instruments is given in section 6.7.

6.5.1 Electrodes and electronics

The HP^3-PP electronics consists of two redundant electronic boards, each of them operating on one side of the payload compartment (see 6.1) as a vector analyser. A scheme of the basic electronic components is shown in fig. 6.4 [75]. As for the measurement principle

Table 6.3: Characteristics of the HP3-permittivity sensor and the payload compartment (PC).

parameter	**value**
PC length [mm]	250
PC diameter [mm]	26
mass front-end electronics [g]	15
mass measurement foils [g]	7
electrode separation [mm]	42
electrode area [mm^2]	30×35.1
frequency range [Hz]	1 - 20,000
frequency resolution [Hz]	1
overall rel. measurement error	< 0.1
rel. measurement error	< 0.05 ($\nu > 100$ Hz)
sampling rate [count/s]	1
mean power consumption [mW]	166.1

needed, the basic electronics components consist of:

- A signal generator which provides the AC-signal,
- an output stage consisting of a digital to analog converter (DAC), filters, amplifiers and two transmitting channels,
- an input stage with two receiving channels, pre-amplifiers and a differential amplifier,
- a vector analyser to determine the amplitude- and phase difference of the received signal to the transmitted one and
- the digital output (ADC) for further data evaluation.

Each of the two redundant electronic boards is connected directly with electrode-foils, which are mounted outside the payload compartment.
Each foil consists of five measuring electrodes, arranged as a classical Wenner-α array (see 6.4). Two transmitters are located on the upper part, two receivers in the middle and one ground electrode at the end of the compartment. Figure 6.5 shows the electrode arrangement in a "flat" configuration [5].
Because of the circular arrangement of four transmitter electrodes in the instruments upper part, the final instrument development will be able to perform a virtual rotation in the

[5] Currently this flat configuration is the state of the art of the PP instrument development.

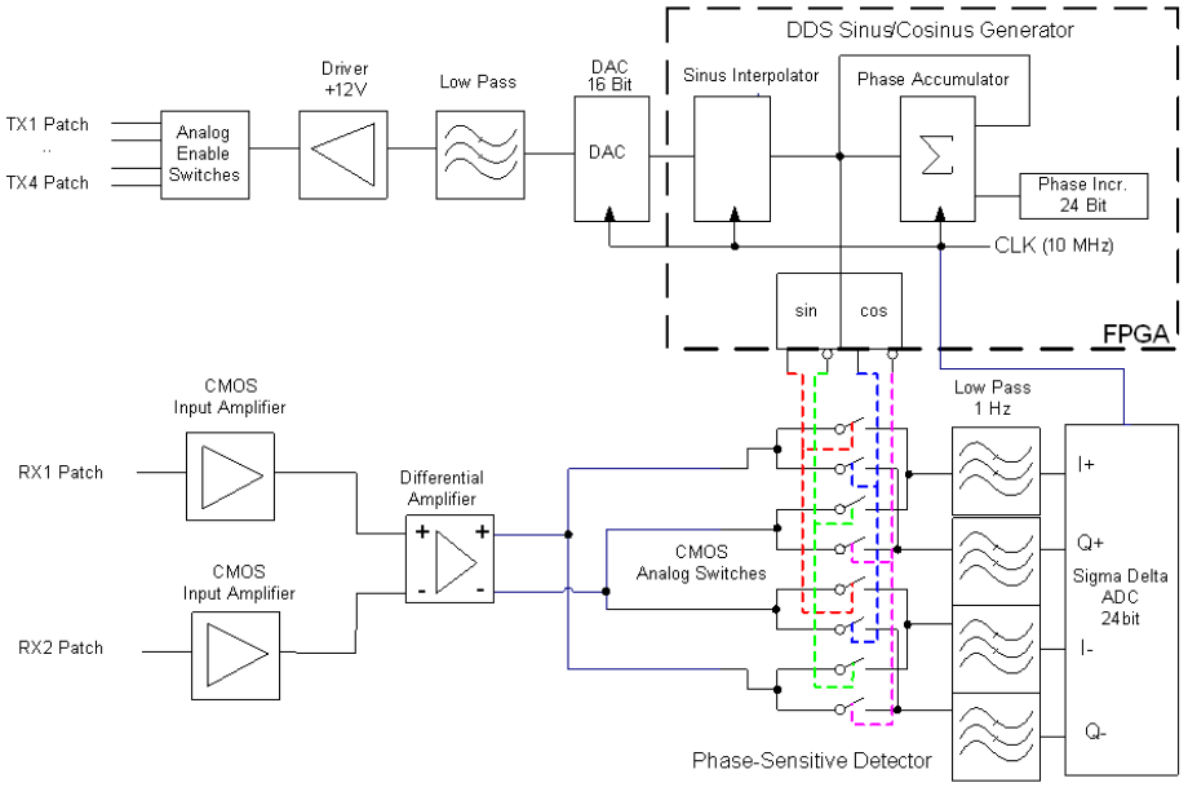

Figure 6.4: The block diagram shows the main parts of the PP-electronics [75].

ground. By switching different transmitters the local environment will be scanned for 360° around PP. To guarantee measurement parameters with high accuracy it was a design requirement to minimise any stray capacities and fields. As a consequence a copper shield electrode is placed under each receiving copper-electrode. This guarding electrode is tied to a fixed local ground potential to which the measured receiving potential is defined. At the lower and the bottom end of the electrode foil system, Kapton layers serve as mechanical protecting layers to avoid any destruction.

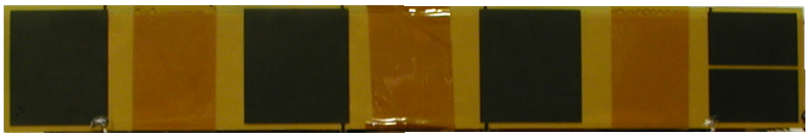

Figure 6.5: The PP-electrodes in a flat configuration. Two transmitters are located on the upper part, two receivers in the middle and one ground electrode at the end of the compartment.

6.6 Laboratory setup

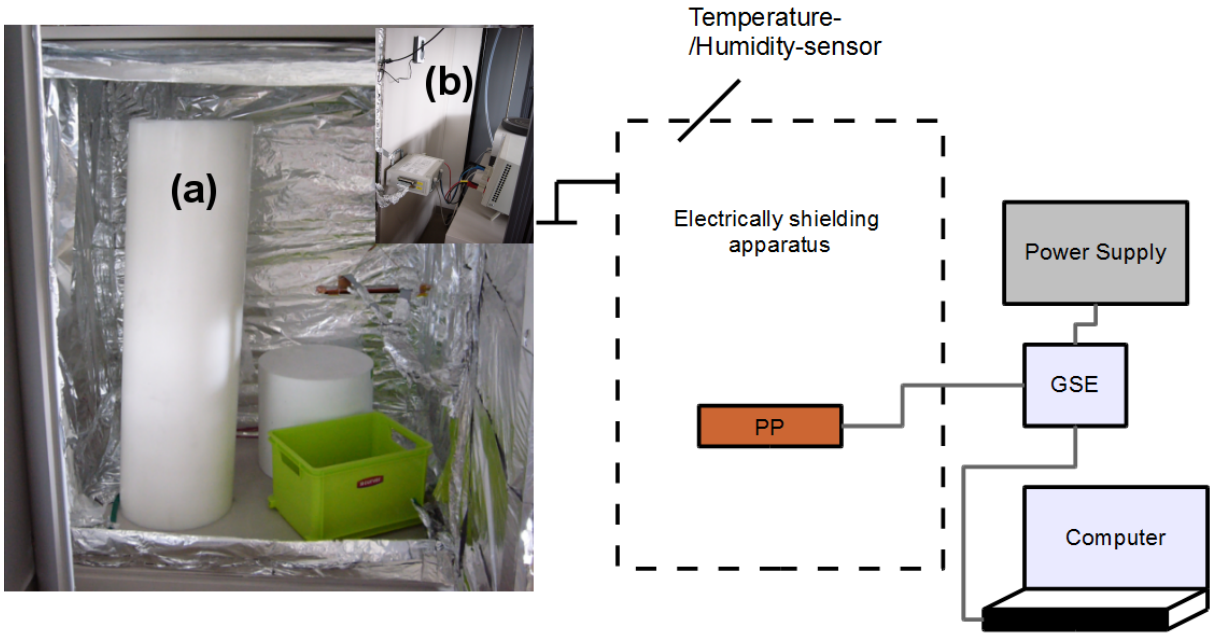

Figure 6.6: Scheme of the laboratory set-up. The various components are explained in the text. In (a) PP is shown in the aluminium shielded closet with some sample materials. (b) shows the GSE - mounted on the outside of the closet - and its power supply.

The laboratory set-up is sketched in fig. 6.6. Additionally a picture of the aluminium-shielded closet (a), as well as the **G**round **S**upport **E**quipment (GSE) (b) is presented. The Permittivity instrument is located in an electrical shielded and temperature as well as humidity controlled measurement apparatus (see sec.7.1). The PP-electronics (section 6.5.1) is connected to the GSE by a shielded flat-band cable to minimise internal noise. The GSE works as data and power supporting system as shown. Next, the GSE is connected to an external power supply and via USB link to the laboratory computer. The measuring software is based on a LabView program [76], which allows to select the measurement frequency, the number of data-points and the operating transmitting electrodes. Furthermore it is possible to control the gain of the PP-input voltage to avoid an overload in the detected signal. A full measurement sequence of pre-selected configurations can be automatically processed by this software.

6.7 A comparison to other measurement concepts

In comparison to the 4-point measurement method of the HP^3-PP (described in section 5.2 and 6.4) two other in-situ measurement concepts are basically able to fulfil the scientific requirements for a permittivity probe instrument (section 6.5):

Table 6.4: Characteristic features of GPR and TDEM compared to the PP
.

	GPR	**TDEM**	**PP**
measurement parameter	travel time of transmitter-wave	Amplitude/time of EM-pulse response	Amplitude/phase shift to transmitter-wave
min. apparatus (+ electronics)	1 antenna	1 loop	4 electrodes
frequency range	MHz - GHz	kHz - MHz	Hz - kHz
exploring depth	cm-km	m-km	cm-m
vertical resolution	cm-100s of m	dm-100s of m	cm

- **G**round **P**enetrating **R**adar (GPR) and
- **T**ime **D**omain **E**electro**m**agnetic (TDEM) methods.

The basic features of the three methods under comparison are listed in table 6.4. The numbers are based on existing and proposed developments for in-situ space instruments [64, 77–79].

Compared to the PP measurement method, GPR determines the travel time and amplitude of a back-scattered wide-band transmitter signal. The instrument measures in frequency-domain and determines the pulse response by Fourier transformation. Layers and inhomogenities with different ϵ_r-values cause the detected scattering signal. With the TDEM method the decay of a secondary field originating from induction currents following an EM-pulse are detected. These induction currents are mainly dependent on the sample conductivity σ (for more details see [80] or [81]).
Following this short explanation, the TDEM is used rather for conducting ground, whereas GPR is suitable preferably for non-conductive ground [64].
As listed in tab. 6.4 the exploring depth of the various systems is strongly dependent on the measurement frequency. As the frequency of typical GPR instruments shows the highest bandwidth, these instruments are able to detect structures in shallow depths as well as those in deeper zones, with comparable high vertical and lateral resolution. The vertical depth of investigation for PP is strongly determined by the penetration depth of the penetrating probe (mole). Only vertical layers along the penetration path are resolved. Laterally (or vertically to the main payload-axis) the investigation depth is in the cm range (determined by the electrode spacing [35]). For the TDEM system the vertical resolution is at 20% of the distance of the target-layer at best [82]. Its lateral resolution is in the magnitude of the vertical distance to the detected layer, if overburdened of a high resistive ground [77] as it is expected for Mars.

Following this information GPR and PP seem to be more appropriate for the shallow sub-surface. In contrast the TDEM system is considered as the best choice for the detection of possible liquid layers in large depths. In general the low frequency instruments are more sensitive to the detection of water. If GPR possibly works at typical H_2O relaxation frequencies ($>$ 1GHz) to detect water, the penetration depth is strongly decreased and makes it impossible to see deep liquid layers. For the detection of water-ice and low concentrations of liquid (as well as maybe adsorbed water) in the near sub-surface PP is most sensitive, because its working frequency includes typical ice relaxation features in the kHz-regime [83]. Moreover, the directly determined permittivity ϵ_r is strongly influenced by small abundances of H_2O (see sec.3.4.2).
In general the methods of PP and TDEM allow a more simple interpretation of the data [77]. GPR resolution and data interpretation is affected by the permittivity value, which is not determined directly, but could be provided using a PP-instrument [64]. Another advantage of PP is the general robustness of the method since the field is guided with the electrodes. Additional influences of lander and other instruments are defined by their design and therefore known. The GPR measurement is influenced additionally by multiple reflections, surface scattering and side lobes of the transmitted wave. TDEM is in general more sensitive to ambient noise, because of working in time domain [77].
In summary one could say that a TDEM system is the most convenient one, if one looks for deep surface liquid layers. For near surface investigations PP and GPR-instruments yield more information. Especially if one expects very low concentration of water and/or ice (maybe only in diurnal or seasonal variations), PP seems to be the most effective and simple way to detect them. The big advantage of GPR is its high resolution to obtain small scale lateral and vertical inhomogeneities.
Finally tab. 6.5 lists masses and mean power consumption of three selected instruments. All instruments have a high technical readiness level for space applications. This makes a comparison yet possible. The total power/mass of the HP^3 is stated, because several units are used together by the scientific instruments. The mass includes electronics, eventual

Table 6.5: `Characteristic mass and power consumption in comparison.`

	GPR [84]	**TDEM [85]**	**HP^3**
mass [kg]	$\approx$ 1.0	$\approx$ 5.5	2.8
mean power consumption [W]	11.0	19.2	4.6

deployment devices or mole. For the TDEM the instrument parameters are stated for a 200 m loop which is proposed by the instrument developer [85]. As listed in the table, the GPR provides the lowest mass, preferably as a consequence that the other two instruments need to be moved. Considering the power budget, the HP^3 needs the lowest power.

CHAPTER 7

Instrument calibration

In this chapter the laboratory work, which has been performed to calibrate the Permittivity Probe, will be described. For an accurate calibration of the instrument the following points had to be considered:

- Appropriate sample dimensions, which influence the data-accuracy of the instrument,
- the measurement shielding against other (internal and external) **EM**-fields and
- the high measurement sensitivity to water abundances.

For the reference data, the sample and measurement processing considering the above mentioned points are explained in section 7.3. Constraints on the Permittivity Probe measurements are presented in the following section.

7.1 Constraints on Permittivity Probe measurement and samples

To estimate the sample diameters needed to get accurate data, the penetration depth of the Permittivity Probe signal was experimentally evaluated. A first approximative value is given by the effective depth of investigation z_e for a Wenner array. Equation 5.5 leads to an effective depth $z_e \approx 2.2$ cm in case of the Permittivity Probe.
Although this depth is sometimes referred to be the field penetrating depth, the effective depth of investigation z_e was introduced mainly for the inversion theory of geophysical applications. It is defined as a median depth, where half of the signal originates from the upper and half of the signal from the lower field lines [86]. The actual dimensions of a test sample, contributing to a measurement, are possibly larger.

However, there was no possibility to increase the thickness of a test sample. Subsequently to get the maximum distance of a signal source influencing the measurement, a simple setup with the laboratory model of the Permittivity Probe was developed: The instrument was placed on a handmade pulley, with which the distance to a fixed sample could be varied. As sample H_2O ($\epsilon_r \approx 80$) was chosen to cause a very high permittivity contrast to the surrounding medium. Since the measurement was performed in the laboratory, this medium was air ($\epsilon_r \approx 1$). In fig. 7.1 the results of this test are plotted for a set of frequencies. At a distance of d $\approx$ 8 cm the Permittivity Probe detects the H_2O sample.

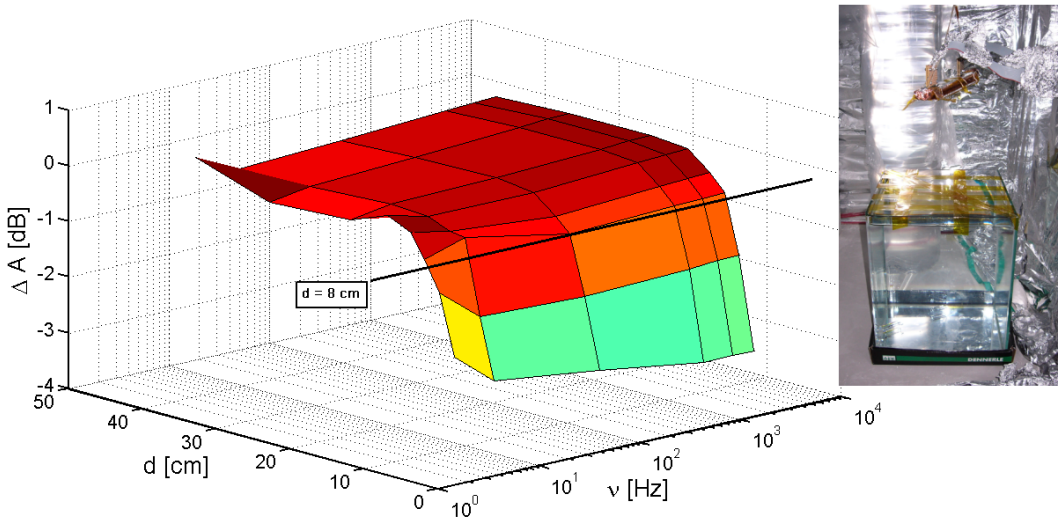

Figure 7.1: Amplitude changes of a H_2O sample (right) as function of distance to the H_2O sample for a set of frequencies. At a distance of $d \approx 8$ cm (red line) the instrument detects the H_2O sample, for an electrode spacing of 4.2 cm.

The signal amplitude of the H_2O sample changes significantly to its reference value at a distance of $d_{ref} = 42$ cm. Similar measurements have been performed to get the instrument sensitivity on the width and the height of the sample. Changes were detected only at sizes in the cm-regime larger than the dimensions of the Permittivity Probe (listed in section 6.5). Summing up these evaluations (including some margin), following sample dimensions for the calibration measurements were defined to be necessary:

$$D = 30 \times 10 \times 10 \; cm^3$$

A measurement shielding against electric noises was necessary. In our case the best way to obtain an appropriate shielding for these sample sizes was to refurbish an empty closet and cover it with aluminium. This was a simple, but effective way to get rid of disturbing electrical environment noise.

Another problem when measuring electrical properties of a sample are water abundances originating from the sample storage or ambient laboratory conditions, as described in chapter 4.1.1.1. Considering this fact, polymer blocks were chosen as reference materials. These were selected to have the smallest possible water assimilation in consideration that the ref-

erence sample should also have a highly different permittivity value. In tab.7.1 the selected polymer samples and their characteristics are listed.[6] The comparable high moisture as-

Table 7.1: The PP calibration samples. Listed are their diameters d, heiht h and the moisture assimilation $m_{\%}$.

sample	d [cm]	h [cm]	$\mathbf{m}_{\%}$ [%]	ϵ'_r
Polytetrafluorethylen (PTFE)	30	30	0.001	2.1
Polyamid 6 (PA 6)	30	30	2.2	3.7

similation of the Polyamid (PA 6) sample had to be taken into account, because it was the only feasible polymer sample with an expected low frequency permittivity value in the range of $\epsilon_{r,PA} \approx 5$. The seasonal temperature variations in the laboratory (292 K $< T_{RT} <$ 296 K) didn't vary the polymer permittivity in a significant way. For the non-polar material PTFE (3.23) yields to a temperature variation of ϵ'_r of 0.9%/100 K for its volume expansion coefficient of $1.25{\cdot}10^{-4}$/K [88]. A study of Laredo et al. [89] for PA 6 noted for a measurement of 1 kHz excitation frequency a temperature change of 0.5% for ϵ'_r and 1 % for ϵ''_r. The evaluation for this is given in the appendix.
The sample permittivities generally were chosen to be in the range of $1 < \epsilon_{r,cali} < 5$. This interval was defined because Martian surface and sub-surface samples are expected to be in this range. Although there exist no data on the electrical properties in the kHz-regime, dielectric properties at least in the radio-wave regime are within this interval [29,90]. Another evidence for the selected interval is given by Simoes et al. [91] and Cereti et al. [92], who performed dielectric measurements on the Martian analogue material JSC Mars-1, which has been cited in various publications as a close spectral soil analogue to Mars' bright surface regions [93,94].
The third needed calibration sample (see chapter 7.2) was air with a permittivity value of $\epsilon_{r,air} \approx 1$.

7.2 Equivalent circuit - Calibration matrix

The HP[3] Permittivity Probe works in a simplified consideration as an impedance measurement system by a capacitive voltage divider as it is sketched in fig. 7.2. By measuring the voltages V_0 and V_{Rx} and knowing the capacity C_{Rx} the unknown impedance $Z_?$ can be calculated by the system transfer function $\frac{V_{Rx}}{V_0}$.

$$\frac{V_{Rx}}{V_0} = \frac{\vec{i} Z_{C_{Rx}}}{\vec{i}(Z_? + Z_{C_{Rx}})}$$

[6] The ϵ'_r values are listed according to the material data-sheets [87] at room temperature.

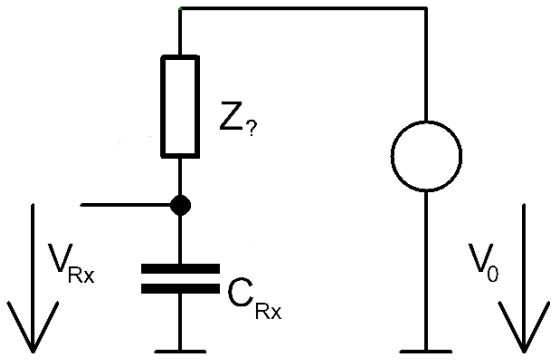

Figure 7.2: In a simplified consideration the HP[3] Permittivity Probe measures the unknown impedance $Z_?$ as a capacitive voltage divider.

For the calculations of the permittivity probe setup, it is easier to work with the sample admittance Y ($Y = Z_?^{-1}$) instead of its impedance $Z_?$. The unknown material admittance is supposed to result from dielectric- as well as conductive phenomena. Considering that the probe setup is principally based on an open capacitor with an unknown dielectric material in it, the admittance is given by:

$$Y = j\omega\frac{\epsilon_r' A}{d} + \omega\frac{\epsilon_r'' A}{d} + \frac{\sigma A}{d} \tag{7.1}$$

$$= \frac{A}{d}\cdot(\sigma + \omega\epsilon_r'' + j\omega\epsilon_r') \tag{7.2}$$

$$= G\cdot(\sigma + \omega\epsilon_r'' + j\omega\epsilon_r') \tag{7.3}$$

In (7.3) A is the area of the setup capacitor and d its plate distance, which can be summed up to a geometric factor G.

To get to a mathematical calibration, the Permittivity Probe measurement setup can be generalised into a linear 4-port device like drawn in fig.7.3. This model has been proposed by Hofbauer G. (company XERXES Klagenfurt, [95]), the design engineer of the PP electronics. The system driving voltage V_0 is supposed to be known. The output voltage V_{Rx} on port 2 is not loaded, no current flows in or out of port 2. The unknown admittance $Y = Z_?^{-1}$ is connected to the device on port 3 and 4 in order to obtain a differential voltage signal. Following the general matrix representation of the admittance in the 4-port model [96], the system is described by:

$$\begin{pmatrix} I_1 \\ 0 \\ I_3 \\ -I_3 \end{pmatrix} = \begin{pmatrix} Y_{11} & Y_{12} & Y_{13} & Y_{14} \\ Y_{21} & Y_{22} & Y_{23} & Y_{24} \\ Y_{31} & Y_{32} & Y_{33} & Y_{34} \\ Y_{41} & Y_{42} & Y_{43} & Y_{44} \end{pmatrix} \begin{pmatrix} V_0 \\ V_{Rx} \\ V_3 \\ V_3 + I_3 Y \end{pmatrix} \tag{7.4}$$

After rearranging and transforming this system of linear equations, the unknown admittance Y can be directly linked to the voltage ratio $\frac{V_{Rx}}{V_0}$ and three constants $K_{1,2,3}$:

$$\frac{V_{Rx}}{V_0} = \frac{Y + K_1}{K_2 Y + K_3} \tag{7.5}$$

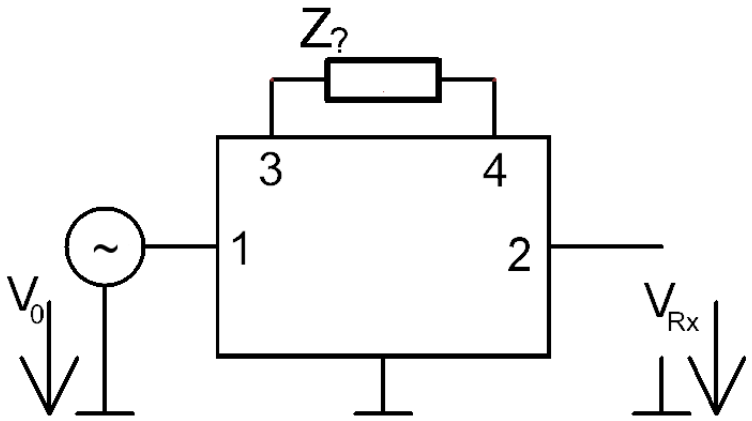

Figure 7.3: The measurement setup can be generalised into a linear 4-port device [95].

The three constants $K_{1,2,3}$ are given by the elements of the admittance matrix:

$$K_1 = \frac{Y_{21}Y_{34} - Y_{21}Y_{44} + Y_{23}Y_{41} + Y_{24}Y_{41} - Y_{21}Y_{43} + Y_{24}Y_{31} - Y_{21}Y_{33} + Y_{23}Y_{31}}{Y_{21}Y_{33}Y_{44} - Y_{24}Y_{33}Y_{41} + Y_{24}Y_{31}Y_{43} - Y_{23}Y_{31}Y_{44} + Y_{23}Y_{41}Y_{34} - Y_{21}Y_{43}Y_{34}}$$
$$K_2 = \frac{Y_{22}Y_{43}Y_{34} - Y_{24}Y_{32}Y_{43} - Y_{23}Y_{32}Y_{44} + Y_{23}Y_{42}Y_{34} + Y_{22}Y_{33}Y_{44} - Y_{24}Y_{33}Y_{42}}{Y_{21}Y_{33}Y_{44} - Y_{24}Y_{33}Y_{41} + Y_{24}Y_{31}Y_{43} - Y_{23}Y_{31}Y_{44} + Y_{23}Y_{41}Y_{34} - Y_{21}Y_{43}Y_{34}}$$
$$K_3 = \frac{Y_{23}Y_{42} - Y_{24}Y_{42} + Y_{22}Y_{44} - Y_{23}Y_{32} + Y_{22}Y_{33} + Y_{22}Y_{34} + Y_{22}Y_{43} - Y_{24}Y_{32}}{Y_{21}Y_{33}Y_{44} - Y_{24}Y_{33}Y_{41} + Y_{24}Y_{31}Y_{43} - Y_{23}Y_{31}Y_{44} + Y_{23}Y_{41}Y_{34} - Y_{21}Y_{43}Y_{34}}$$

By combining (7.3) and (7.5) one obtains the direct relationship of the electric parameters σ and ϵ_r^* to the measured voltage ratio $\frac{V_{Rx}}{V_0}$:

$$\sigma + \omega\epsilon_r'' + j\omega\epsilon_r' = \frac{\tilde{K}_1 - \frac{V_{Rx}}{V_0}\tilde{K}_3}{\frac{V_{Rx}}{V_0}K_2 - 1} \tag{7.6}$$

The constants $\tilde{K}_1$ and $\tilde{K}_2$ are connected to the geometric factor G (see (7.3)):

$$\tilde{K}_1 = \frac{K_1}{G} \qquad \tilde{K}_3 = \frac{K_3}{G}$$

Finally the whole calibration procedure is reduced to the problem of determining the three unknown constants $\tilde{K}_1$, K_2 and $\tilde{K}_3$. Three independent linear equations have to be solved to evaluate the calibrated parameters ϵ_r^* and σ.[7]
Following the considerations above, in total three samples with known parameters ϵ_r^* and σ are needed to calibrate the instrument. Measuring the voltage ratio $\frac{V_{Rx}}{V_0}$ with the Permittivity Probe leads to the unknown constants $\tilde{K}_1$, K_2 and $\tilde{K}_3$. The ensuing system of

[7] In practise, due to the frequency functionality of permittivity ϵ_r^* and conductivity σ ((4.11)) only the real part of the permittivity ϵ_r' is determined as imaginary solution of (7.6) neglecting contributions from σ''. To get the ohmic sample conductivity σ, one has to evaluate this value at low angular frequencies, to minimise contributions of the imaginary part of permittivity ϵ_r'' (goes with ω in (7.6)).

equations has then to be solved (eq. 7.6). (The indices $_{1,2,3}$ are dedicated to the 3 calibration samples.):

$$
\begin{aligned}
-\tilde{K_1} + \frac{V_{Rx1}}{V_0}(\sigma_1 + \omega\epsilon''_{r1} + j\omega\epsilon'_{r1})K_2 + \frac{V_{Rx1}}{V_0}\tilde{K_3} &= \sigma_1 + \omega\epsilon''_{r1} + j\omega\epsilon'_{r1} \\
-\tilde{K_1} + \frac{V_{Rx2}}{V_0}(\sigma_2 + \omega\epsilon''_{r2} + j\omega\epsilon'_{r2})K_2 + \frac{V_{Rx2}}{V_0}\tilde{K_3} &= \sigma_2 + \omega\epsilon''_{r2} + j\omega\epsilon'_{r2} \\
-\tilde{K_1} + \frac{V_{Rx3}}{V_0}(\sigma_3 + \omega\epsilon''_{r3} + j\omega\epsilon'_{r3})K_2 + \frac{V_{Rx3}}{V_0}\tilde{K_3} &= \sigma_3 + \omega\epsilon''_{r3} + j\omega\epsilon'_{r3}
\end{aligned}
$$

In matrix notation:

$$
\begin{pmatrix}
-1 & \frac{V_{Rx1}}{V_0}(\sigma_1 + \omega\epsilon''_{r1} + j\omega\epsilon'_{r1} & \frac{V_{Rx1}}{V_0} \\
-1 & \frac{V_{Rx2}}{V_0}(\sigma_2 + \omega\epsilon''_{r2} + j\omega\epsilon'_{r2} & \frac{V_{Rx2}}{V_0} \\
-1 & \frac{V_{Rx3}}{V_0}(\sigma_3 + \omega\epsilon''_{r3} + j\omega\epsilon'_{r3} & \frac{V_{Rx3}}{V_0}
\end{pmatrix}
\begin{pmatrix} \tilde{K_1} \\ K_2 \\ \tilde{K_3} \end{pmatrix}
=
\begin{pmatrix}
\sigma_1 + \omega\epsilon''_{r1} + j\omega\epsilon'_{r1} \\
\sigma_2 + \omega\epsilon''_{r2} + j\omega\epsilon'_{r2} \\
\sigma_3 + \omega\epsilon''_{r3} + j\omega\epsilon'_{r3}
\end{pmatrix}
\tag{7.7}
$$

7.2.1 Mathematical error treatment

Basically the equation to be solved (eq. 7.7) is a standard matrix equation of the form:

$$\hat{\mathbf{A}}\mathbf{x} = \mathbf{d}$$

In case of the HP^3-instrument calibration the solution $\mathbf{d}$ is given by the reference measurement. The matrix components of $\hat{\mathbf{A}}$ are stated following (7.7) as a combination of reference and Permittivity-Probe measurements. Typically for a standard fitting problem the vector $\mathbf{x}$ remains as the unknown parameter. Thus

$$\mathbf{x} = \hat{\mathbf{A}}^{-1}\mathbf{d} \tag{7.8}$$

yields to the searched values (in our case the calibration constants K_i). As known for such fitting problems [97] the error of the measured value d_i is considered by its standard deviation σ_i:

$$\frac{1}{\sigma_i} \cdot A_{ij} \cdot x_j = \frac{1}{\sigma_i} \cdot d_i$$

To get the error of the matrix components A_{ij} in the calculation, one has to assume that the matrix $\hat{\mathbf{A}}$ is the sum of the matrix $\hat{\mathbf{A}}_\mathbf{0}$ in (7.7) and an error matrix $\mathbf{\Delta}\hat{\mathbf{A}}$, defined by the errors of each matrix component $A_{0,ij} = f(a_1, a_2, ...a_n)$:

$$\Delta A_{ij} = \sum_k \left(\frac{\partial A_{0,ij}}{\partial a^k_{ij}} \cdot \Delta a^k_{ij} + ...\right)$$

Δa_{ij}^k are the errors of the parameters defining the matrix element $A_{0,ij}$.
Following this assumption the inverse of matrix $\hat{\mathbf{A}}^{-\mathbf{1}}$ is given as:

$$\begin{aligned}\hat{\mathbf{A}}^{-\mathbf{1}} &= (\hat{\mathbf{A}}_\mathbf{0} + \Delta\hat{\mathbf{A}})^{-1} \\ &= [\hat{\mathbf{A}}_\mathbf{0}(\hat{1} + \hat{\mathbf{A}}_\mathbf{0}^{-1}\Delta\hat{\mathbf{A}})]^{-1} \\ &= (\hat{1} + \hat{\mathbf{A}}_\mathbf{0}^{-1}\Delta\hat{\mathbf{A}})^{-1}\hat{\mathbf{A}}_\mathbf{0}^{-1} \\ &= [\hat{1} - \hat{\mathbf{A}}_\mathbf{0}^{-1}\Delta\hat{\mathbf{A}} + (\hat{\mathbf{A}}_\mathbf{0}^{-1}\Delta\hat{\mathbf{A}})^2 - \dots\,]\hat{\mathbf{A}}_\mathbf{0}^{-1} \\ &\approx \hat{\mathbf{A}}_\mathbf{0}^{-1} - \hat{\mathbf{A}}_\mathbf{0}^{-1}\Delta\hat{\mathbf{A}}\hat{\mathbf{A}}_\mathbf{0}^{-1}\end{aligned}$$

With (7.8) the unknown vector $\mathbf{x}$ is determined by the vector $\mathbf{x}$ without errors and the error-vector $\Delta\mathbf{x}$:

$$\mathbf{x} = \mathbf{x_0} + \Delta\mathbf{x} \tag{7.9}$$

$$\approx \hat{\mathbf{A}}_\mathbf{0}^{-1}\mathbf{d} - \hat{\mathbf{A}}_\mathbf{0}^{-1}\Delta\hat{\mathbf{A}}\hat{\mathbf{A}}_\mathbf{0}^{-1}\mathbf{d} \tag{7.10}$$

7.3 Reference measurement

As required for calibration (left side of (7.7)), the permittivity ϵ_r^* and conductivity σ values of three calibration samples (see sec.7.1) are needed. For air these values are commonly known to be in very good approximation $\epsilon_{r,air} \approx 1$ and $\sigma_{air} \approx 0$, whereas the values for the two polymers depend on the production process. These values were determined with a high accuracy impedance spectrometer "Alpha-A series" produced by Novocontrol Technologies [45] (fig.7.4).

In fig.7.4 the main components of the reference instrument are:

- The mainframe, which works as vector analyser and also houses the signal generator,
- the active sample cell is a special measurement device to minimise all disturbing cable and cell effects [45] and
- the gold plated electrodes provide a defined sample volume to evaluate the material properties.

The instrument works as a capacitor filled with the sample of interest. The AC-signal generator applies a fixed voltage U* with angular frequency ω to the sample capacitor. The resulting currents in the capacitor material I* generally are complex values. The ratio of measured voltage U* to current I* yields the unknown impedance, which is connected to the sample permittivity ϵ_r^* by:

$$\epsilon_r^* = \frac{1}{j\omega C_0 Z^*} \tag{7.11}$$

C_0 is the empty sample capacity which is defined through the capacitor geometry (plate

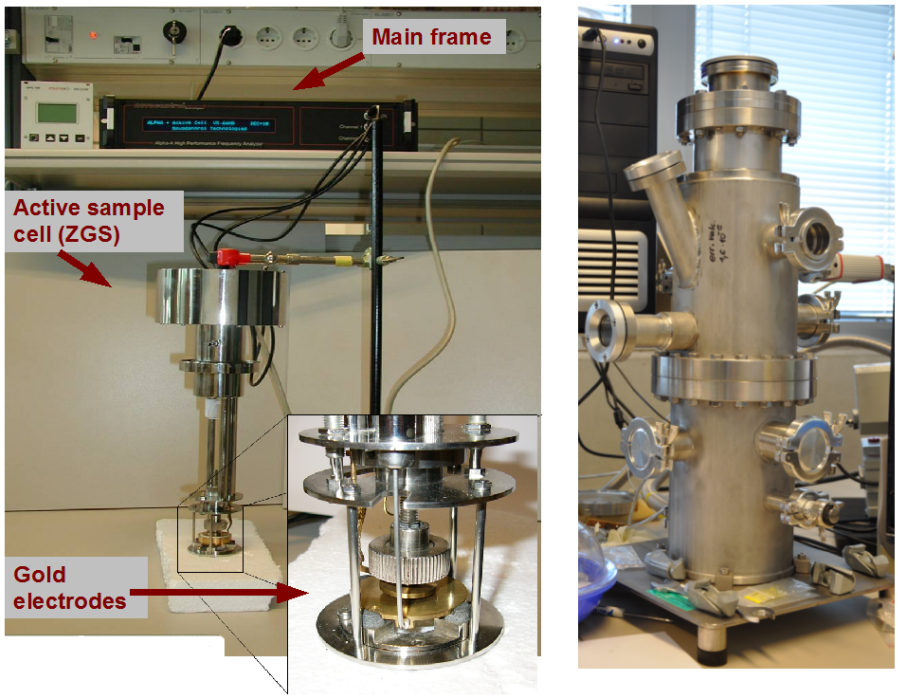

Figure 7.4: Left: The reference measurement system of Novocontrol Technologies [45] with its main components. Right: The vacuum chamber for reference measurements in low pressure.

area A and height d):

$$C_0 = \epsilon_0 \frac{A}{d}$$

Relevant parameters, like the sample conductivity and the dielectric loss are derived from this.

To get high accuracy data, certain points have to be considered within the reference measurement and evaluation [45]:

1. The sample-to-plate contact of the capacitor has to be as perfect as possible.
2. To minimise electrode stray capacities due to edge effects, the ratio of sample thickness d to its diameter D should be minimised.
3. The uncertainty in sample geometry (especially its height) has to be minimised.

To test the sample-to-plate contact, the calibration samples were covered with liquid silver paint. No changes in the data to the uncovered samples were detected. Subsequently, to protect the gold electrodes from silver residuals, the most part of the measurements was performed with uncovered samples. The ratio of sample diameter D to its thickness d was defined by the thinnest available reference sample ($d \approx 1$ mm) and the electrode diameter $D = 40$ mm. The uncertainty in sample geometry was included into the calibration by the errors of reference values (7.2.1). The selected samples and their reference values are listed in table 7.2. The evaluated real part permittivity values ϵ_r' agree well with the values

provided by the selling company (listed in tab. 7.1) and general literature values (tab. 3.1). As mentioned in section 7.2, it was not possible to seperate the values of σ and $\epsilon''_{r,d}$. However, the measured value ϵ''_r ($\epsilon''_r = \epsilon''_{r,d} + \frac{\sigma}{j\omega}$) is sufficient for calibration (see (7.7)). To minimise moisture assimilation in the sample, the precision reference measurements were performed in vacuum (pressure p $< 1 \cdot 10^{-2}$ mbar, fig. 7.4,right) at room temperature [8].

Table 7.2: The calibration values measured with the high accuracy impedance spectrometer. Listed are the sample heights d and permittivity values $\epsilon_r{}'('')$ of the samples.

sample	**d [mm]**	ϵ'_r **[1]**	ϵ''_r $(\cdot 10^{-2})$ **[1]**
Polytetrafluorethylen (PTFE)	1.00 ± 0.02	2.1	0.02-0.28
Polyamid 6 (PA 6)	1.05 ± 0.02	5.4-3.5	36-11

7.3.1 Accuracy of the reference measurement

The measurement accuracy of the precision impedance spectrometer is defined by the selling company for various measurement ranges [45].
To test the validity of the accuracy data sheet, the data of a standard RC-element was compared to the data provided by Novocontrol Technologies. The result is shown in fig.7.5. As shown in the figure the measurement standard in the laboratory in Graz coincidences very well with the standard data of the company. Since the results agree, the accuracy specification provided by the company can be used. The measurement accuracy for sample capacities of 20-60 pF - such as the calibration samples - lies for the Permittivity Probe frequency range (4 - 20,000 Hz) at maximum in between the 0.2% amplitude- and 0.06% phase error [45]. The correct uncertainty was implemented in (7.6). As these values are very low, the major source of uncertainty seems to be caused by the geometry of the samples.
Another verification of high accuracy within the reference measurement was obtained through a direct comparison of a measurement with one of our test samples by Novocontrol Technologies. Figure 7.6 shows the comparison of the PTFE sample measured in Graz and the measurement of the same sample by Novocontrol in two different ways. In a first measurement they determined the permittivity values with a plate capacitor, the second data (BDS) was obtained with a special measurement cell, which originally is built for liquid samples. The real part permittivity ϵ'_r is in very good agreement, the imaginary part ϵ''_r varies even within the two methods provided by Novocontrol. Possible reasons are mentioned in sec. 7.4.
Having the general measurement accuracy as the instruments of Novocontrol Technologies,

[8] For the chosen sample capacity-interval (< 50 pF) a sample cell stray capacity of 1 pF had to be subtracted from the measured values [45].

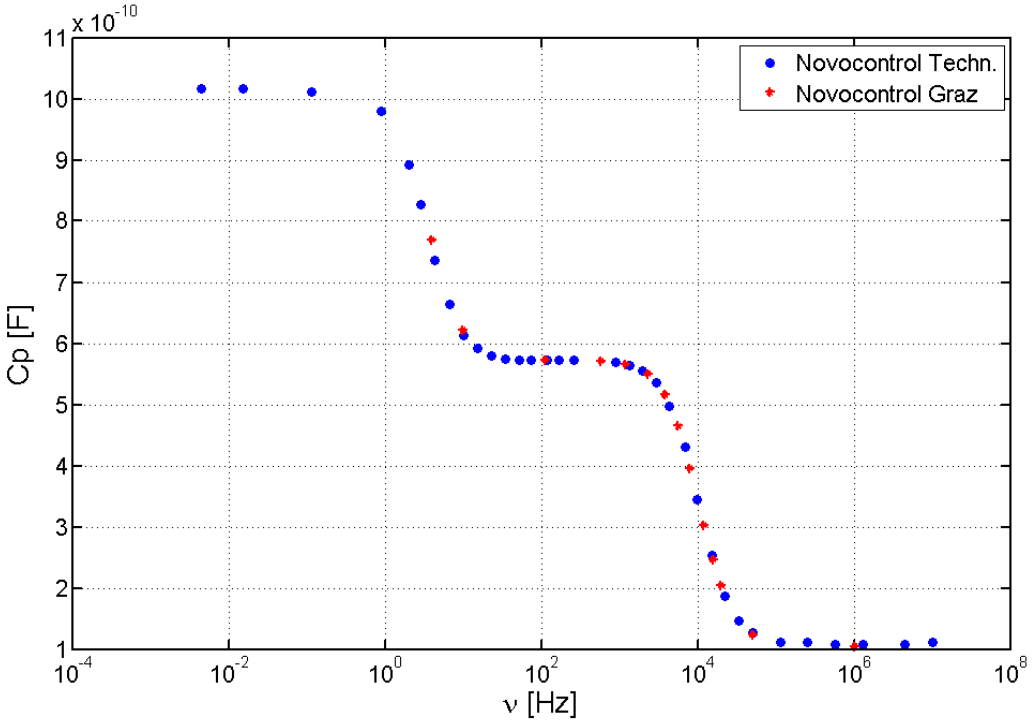

Figure 7.5: The comparison of a standard RC-element measurement in Graz is compared with the data provided by Novocontrol.

systematic instrument uncertainties have to be considered following the provided diagram. Figure 7.5 shows the comparison of a standard RC-element measurement in Graz with the data provided by Novocontrol Technologies.

7.3.2 Measurement of liquid and fine granular samples

To evaluate the calibration for various kinds of materials, liquid and fine granular samples (see sec. 7.4) have been measured with the reference instrument. To get a known geometry of the reference capacitor for these samples a silica ring provided by Novocontrol Technologies with a nominal height of 1 mm [45] has been glued onto the lower plate of the capacitor (fig. 7.7). The actual ring dimensions - its height d and its inner and outer diameter (D_i,D_o) - were measured with a calliper:

$$d = (0.98 \pm 0.02)\ mm$$
$$D_i = (35.42 \pm 0.02)\ mm$$
$$D_o = (39.99 \pm 0.02)\ mm$$

For the evaluation of the data obtained by measuring samples with the silica ring a linear model like the Maxwell-Garnett formula (eq.3.25) between sample and ring was proposed by Novocontrol Technologies [98]. To test this assumption, an accurate fitting plate of a Polyethylene (PE) (d_{PE} =(0.99 ± 0.02) mm) sample as well as a PTFE plate (d_{PTFE} =(1.00

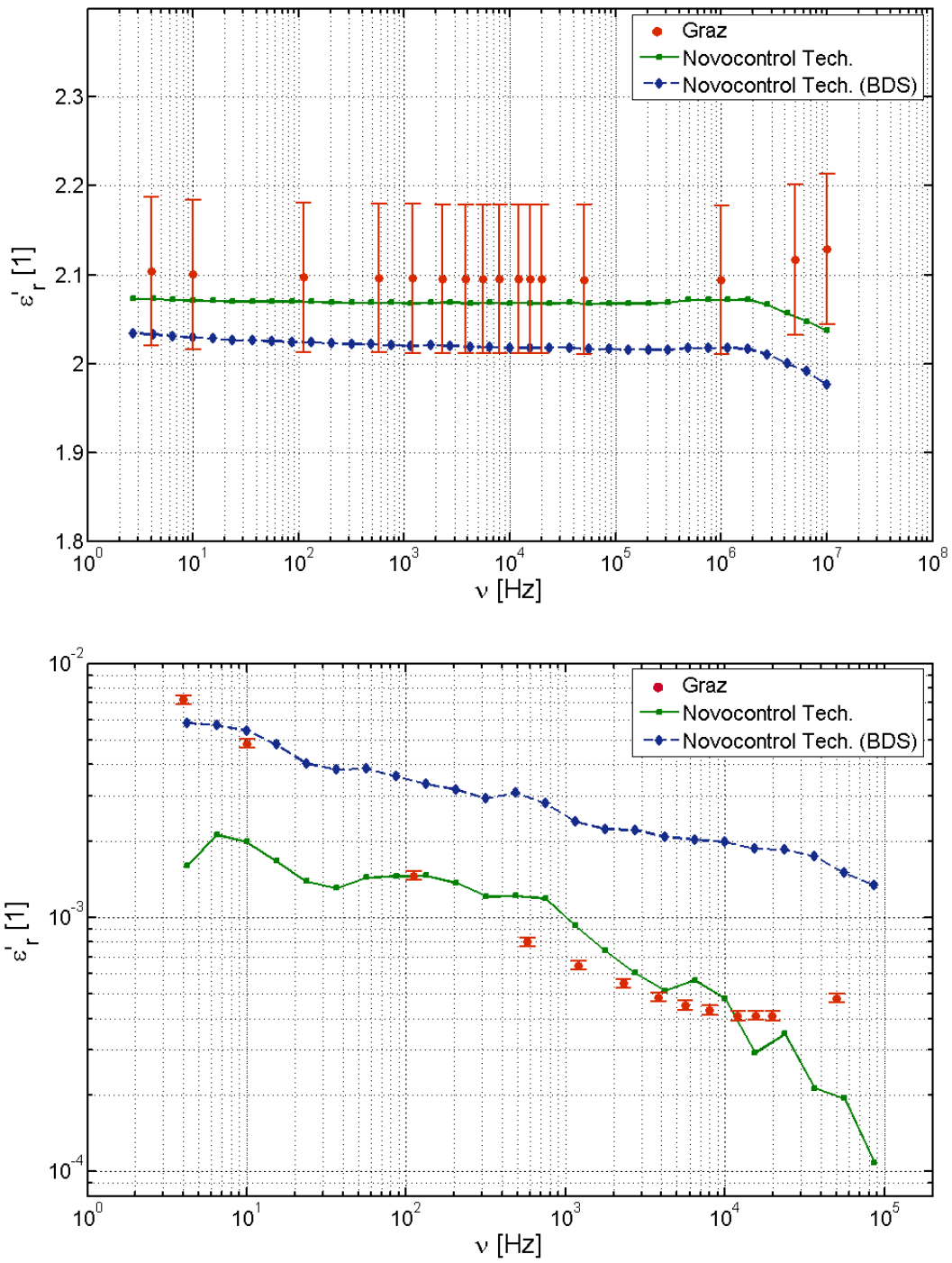

Figure 7.6: The plots compare our reference values for PTFE compared to measurements by Novocontrol Technologies with our PTFE sample. Novocontrol provided data by the measurement with a plate capacitor similar to that used in Graz and a special sample cell (BDS). The real part permittivity ϵ_r' is in very good agreement, whereas the imaginary part ϵ_r'' comparison even fails for the two Novocontrol data sets.

Figure 7.7: To measure liquid and fine granular samples, a silica ring was glued on to the lower electrode plate of the reference instrument.

± 0.02) mm) were cut. Both samples showed a slightly non-linear dependence in their effective permittivity ϵ^*_{eff}, which was described by the measured polymer permittivities ϵ^*_P of the full capacitor and the measurement of the capacitor with only the silica ring (ϵ_{sil})

$$\epsilon^*_{eff} = f_P(\epsilon^*_P)^\zeta + f_{sil}(\epsilon^*_{sil})^\zeta,$$

with the contributing volume fractions f_P and f_{sil}. The exponent ζ was evaluated to be:

$$\zeta = 1.1 \pm 0.2$$

Following this evaluation, the influence of the silica ring was subtracted from the measured sample effective permittivity for liquid and fine granular samples.

7.4 Calibration and evaluation

For calibration, the matrix equation 7.7 was implemented in Matlab [99]. The measurement ($\frac{V_{Rx,i}}{V_0}$) of PP, as well as the reference values ϵ'_r and ϵ''_r were inserted according to section 7.1 and section 7.2. For several frequencies in the instrument range (1 Hz - 20 kHz) the calibration constants were determined. Those are summarised in the appendix.

Real part permittivity ϵ'_r

To test the evaluated calibration of the real part permittivity ϵ'_r, eq.7.6 has been applied to four reference samples (Poly-Metha-Methyacrylate (PMMA), Poly-Ethylen (PE), Aluminium dioxide (Al_2O_3)) and dielectric oil. These samples have been selected to serve for a comparison of calibration for the selected permittivity range between 2 and 5 (see sec.7.1). Furthermore the four test samples provide data for three different types of materials,

- solid (PE and PMMA),
- liquid (diel oil),
- fine granular (Al_2O3, gain size < 0.1 mm [100]),

and therefore test the calibration for mechanical different material states. Figure 7.8 shows the comparison between reference, not-calibrated and calibrated frequency spectrum of permittivity ϵ'_r for the four test samples. As shown, a clear improvement is obtained for the

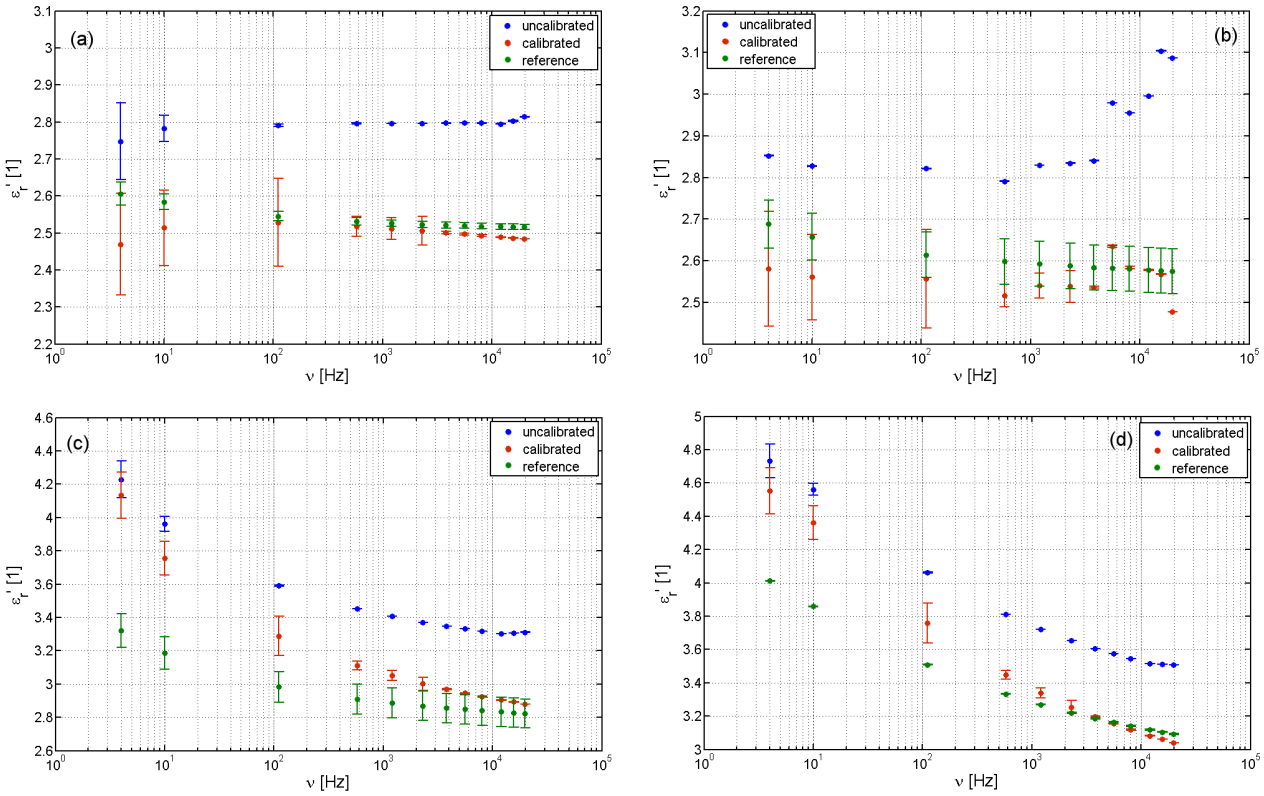

Figure 7.8: The ϵ'_r-frequency spectrum of the four test samples (a) PE, (b) dielectric oil, (c) Al_2O_3 and (d) PMMA. Compared are the calibrated spectrum to the not-calibrated one and the reference data.

calibrated data compared to the not-calibrated spectrum for all samples in most parts of the PP-frequency range. The variation of the low frequency values to the reference sample for PMMA and Al_2O_3, most likely originates in a slightly different H_2O content of the test sample compared to the reference sample. This varies especially the low frequency dispersion in the sample, because higher heterogeneity through H_2O assimilation in a sample causes contributions to interfacial polarisation mechanisms (see sec.4.1.1.1)

In fig. 7.9 the relative deviations for the four test samples in comparison to the reference measurement are plotted as function of frequency. In red the not-calibrated data is presented, in blue the calibrated one. As shown the relative deviations of the PMMA- and Al_2O_3- sample cause a big spread for the lower frequency-permittivities. For clear presentation, the error bars of fig. 7.8 are not included into this plot. Figure 7.10 shows the mean relative deviation $\langle \frac{\Delta\epsilon'_r}{\epsilon'_r} \rangle$ of the four mentioned test samples as a function of frequency ν before and after calibration. The error bars mark the scattering in this value for the four test samples. Through the calibration, a mean relative deviation of less than 5 % for the most part of the measurement frequency is achieved. This 5% limit was a design requirement for the PP instrument. In general, for the whole frequency range an improvement to the uncalibrated data is obtained. The higher deviation in the low frequency ranges is a direct result of the deviation of the PMMA and Al_2O_3 test sample.

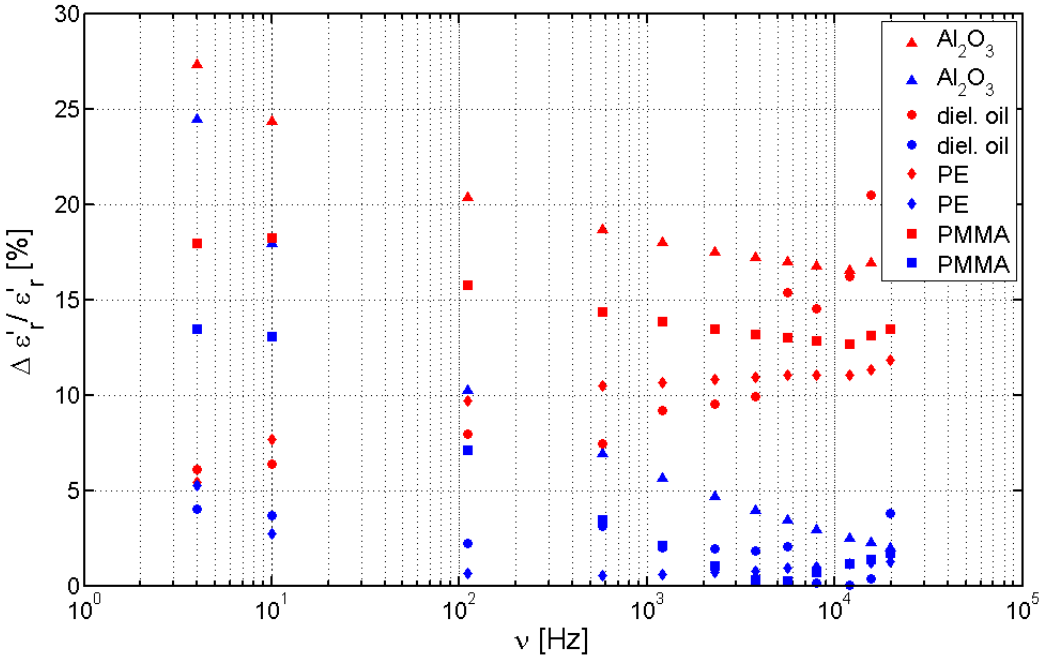

Figure 7.9: The evaluated relative deviation of the four test samples (PE, PMMA, Al_2O_3, dielectric oil) as function of frequency. In red the not-calibrated data, respectively in blue the calibrated one, is shown.

Imaginary part permittivity ϵ_r''

Figure 7.11 shows the mean relative deviation to the reference values of the imaginary part of permittivity ϵ_r'' for the three test samples PE, PMMA and Al_2O3 compared to the uncalibrated data. The data of dielectric oil was not considered, because of variations in decades to the reference data. This variation seems to be originating from additional sources of conductivity from impurities in the liquid phase, which strongly influence the conductivity and therefore the imaginary part of permittivity (see text below). As plotted, only for the very first frequencies a significant decrease of the mean relative deviation is obtained. On a first look the calibration for the imaginary part of permittivity ϵ_r'' fails. The calibration is shown as an improvement when looking on the absolute deviation of the imaginary permittivity values of the test samples to the reference data (fig. 7.12). Generally there exist two main reasons for the high discrepancies between the data from the Novocontrol spectrometer and PP:

1. Weak comparability of imaginary part measurement between reference and PP.
2. Sample treatment in ambient laboratory conditions for PP and comparability to reference samples taken in low pressure environment.

The different measurement methods of the Novocontrol spectrometer (sec. 7.3) and PP (sec. 6.5) play a crucial role. For dielectric measurements with two electrode devices like the reference system, in general contact impedances have to be quantified and eliminated

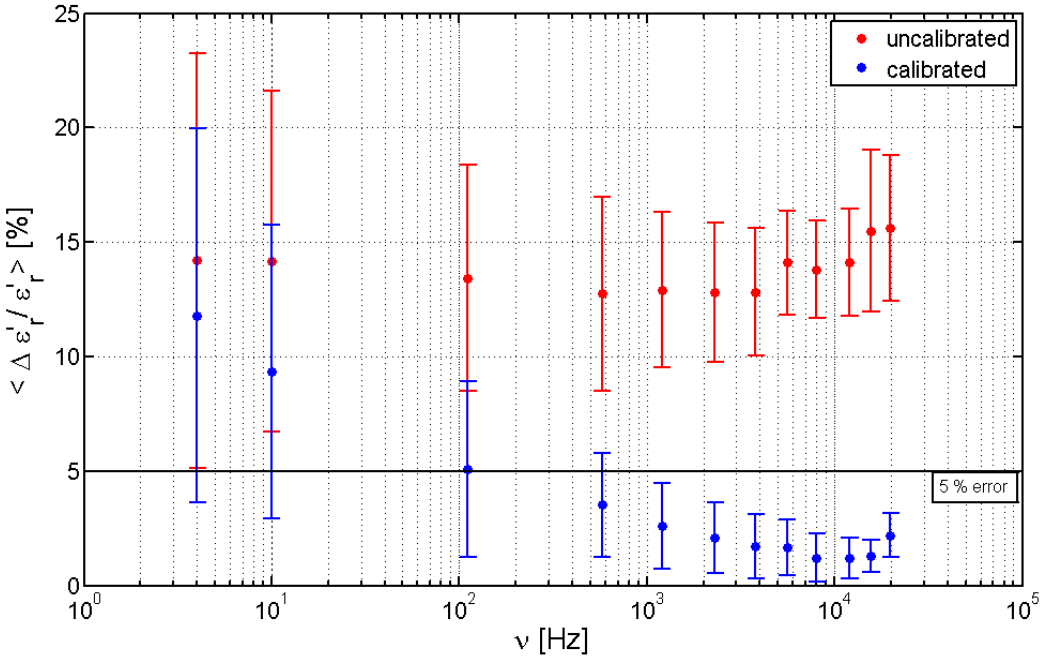

Figure 7.10: The evaluated mean relative deviation of ϵ'_r for four test samples (PE, PMMA, Al_2O_3, dielectric oil) to the reference values. Compared are the deviations before and after calibration. The error bars show the spread of this value for the four test samples.

from the measured impedance in contrast to the 4-point measurement [101]. Those possibly vary the measurement of permittivity in amplitude and phase. Although not recognised in the real part permittivity measurement, the imaginary part could be influenced significantly, because of its small order of magnitude typically less than 10^{-2} for dry polymers (the real part permittivity is in the order of 10^0). The elimination of contact impedances for the reference measurement requires various sample geometries, which haven't been available for this study.

As a second point, the imaginary part of permittivity is highly affected by water impurities in the sample, which cause higher conductivities. The result is an increased value of ϵ''_r (see sec.4.1.1.1). Thus the sample storage of the PP-samples under ambient laboratory conditions possibly plays an important role, because small variations in the sample volume water content compared to the reference samples vary the imaginary part permittivity.

Furthermore, the small reference sample plate (V_{Novo} ≈1 cm^3) is not exactly representing the bulk water-volume fraction of the PP-sample volume (V_{PP} ≈ 600 cm^3), especially when considering that the precision measurements for accuracy had to be performed under vacuum conditions. Considering that, drying and storing as well as measurement of the polymers in vacuum could provide more comparable data. Unfortunately, this doesn't seem to be feasible for polymer blocks with dimensions used for the PP measurement (see sec.7.1).

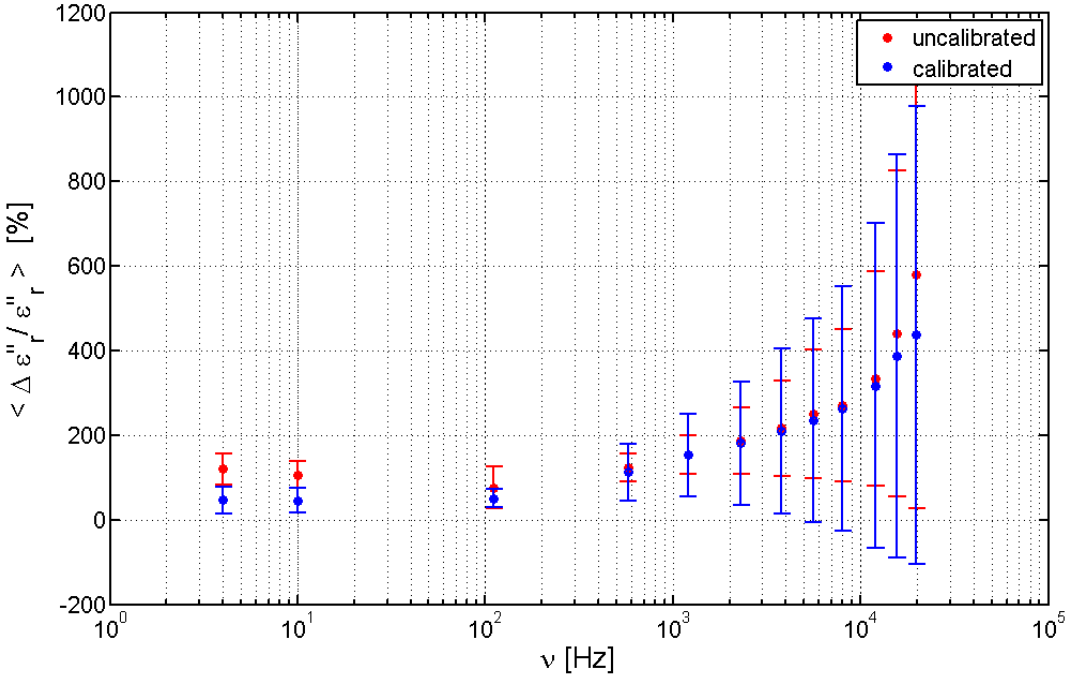

Figure 7.11: The evaluated mean relative deviation of ϵ_r'' for three test samples (PE, PMMA, Al_2O_3). Compared are the deviations to the reference measurement before and after calibration. The error bars symbolise the straying of the data for the three test samples in their mean relative deviation.

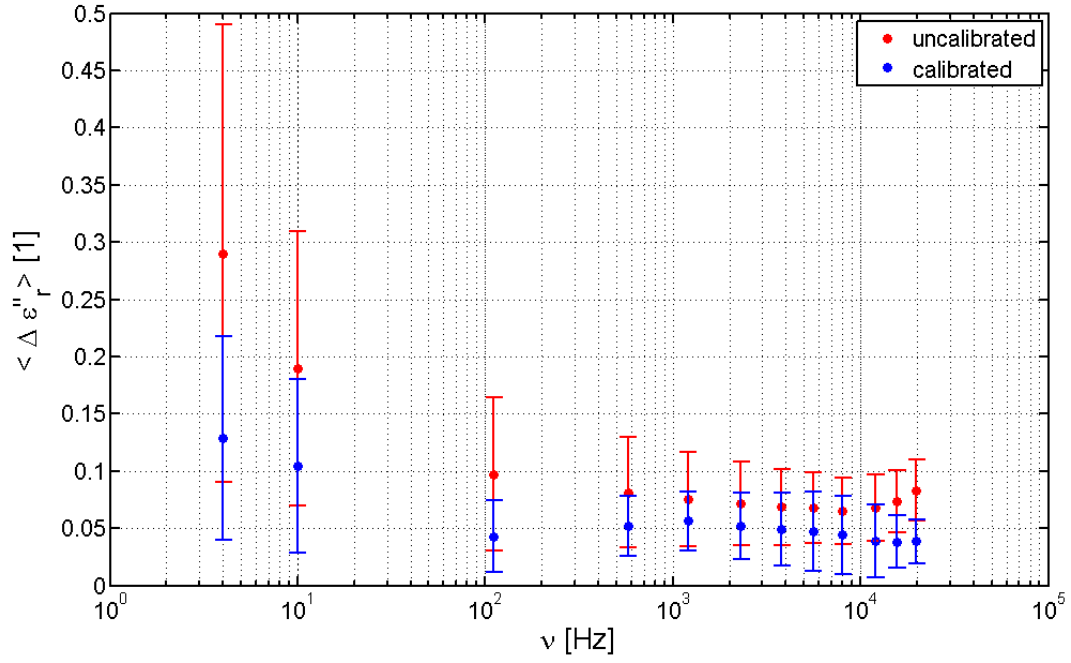

Figure 7.12: The evaluated mean absolute deviation of ϵ_r'' for three test samples (PE, PMMA, Al_2O_3). Compared are the deviation to the reference data before and after calibration.

If one trusts the comparability of the PP and Novocontrol imaginary data, which is not likely following the above mentioned points, one finally can expect an error in the assumption of a linear 4-port model describing the instrument, obviously being a simplification of the real instrument.
Nevertheless this disagreement in the values of imaginary permittivity can be taken into account. The uncertainty in conductivity - even if it is supposed to result from the evaluations above - allows a clear determination of the conductivity range. Even for relative errors supposed to be above 400 % (see fig.7.11) the data range is determined for expected conductivities of less than 10^{-7} Sm^{-1} with ranges varying by orders of magnitude in literature, including estimates for Mars and dry geologic materials [65, 90, 91, 102, 103].
Finally the interest of determining accurate values of imaginary part permittivity - and not the diurnal or seasonal variation - lies in the low frequency values. Those are supposed to be dominated by the static conductivity σ_0. In this frequency region PP provides the most accurate data.

CHAPTER 8

Instrument performance validation

Beneath the calibration, which is described in chapter 7, instrument performance tests of the Permittivity Probe (PP) have been performed to validate this new permittivity-instrument. The test results are presented in the upcoming chapter. In the first section the PP measurement accuracy is determined.

8.1 Accuracy of the HP^3-Permittivity Probe

This section gives an accuracy estimation of the electrical properties determined by PP. Following these assumptions, the measurement uncertainty of the data points in the upcoming sections is given.
To estimate the accuracy of the Permittivity Probe, one has to consider various systematic measurement uncertainties:

- Limited electronics measurement accuracy,
- variation in apparatus and materials,
- systematic errors of the instrument and
- mathematical data evaluation methods.

In general the PP electronics measures the vector components of the complex voltage ratio $\frac{V^*_{rx}}{V^*_0} =: U^*_{rx}$, where $V*_0$ is the source signal and V^*_{rx} the measured differential potential, with an accuracy better than 99% [104]. Following (4.17) and (5.3) the electrical properties

are determined then by

$$\epsilon_r^{'} = \frac{\Re\{\mathbf{Z_0}\}}{\Re\{\mathbf{Z_m}\}} = \frac{\Re\{\mathbf{U_m}\}}{\Re\{\mathbf{U_0}\}} \tag{8.1}$$

$$\epsilon_r^{''} = \frac{\Im\{\mathbf{Z_0}\}}{\Im\{\mathbf{Z_m}\}} = \frac{\Im\{\mathbf{U_m}\}}{\Im\{\mathbf{U_0}\}} \tag{8.2}$$

$$\frac{\sigma_m}{\omega\epsilon_0} = \frac{\Im\{\mathbf{Z_0}\}}{\Im\{\mathbf{Z_m}\}} = \frac{\Im\{\mathbf{U_m}\}}{\Im\{\mathbf{U_0}\}} \tag{8.3}$$

where index '0' indicates the reference (air) measurement and index 'm' the sample material measurement. Thus, the contribution to uncertainty caused by the instrument electronics (and the statistical error) adds in a worst case assumption to the evaluation of the permittivity values as

$$\Delta\epsilon_r^* = \frac{\delta\epsilon_r^*}{\delta U_{rx}^*}\Delta U_{rx}^* + \frac{\delta\epsilon_r^*}{\delta U_0^*}\Delta U_0^*. \tag{8.4}$$

For the conductivity σ_m the additional term $\omega\epsilon_0$ has to be included.

For the Permittivity Probe additional uncertainties including sample variations, slight differences in the set up (e.g. the position on the sample) and the limited accuracy by the instrument itself (e.g. geometry, stray capacities,...) have to be considered.

For the PP measurement, sample- and variations in the apparatus have been minimised, especially the position of the instrument on sample and in the measurement cell were tried not to be varied. In fact, these uncertainties have been considered by the evaluation of mean values of multiple time series over several months. Therefore they are already included into the uncertainties of the final (mean) $\langle\frac{U_{rx}}{U_0}\rangle$-values of a sample.

The instrument itself provides uncertainties foremost due to geometric factors and additional stray capacities. These uncertainties are difficult to quantify. In general they are minimised through the instrument calibration.

The consideration of the statistical uncertainties within a material measurement and its reference is simple (see (8.4)). The mathematical formula which yields the calibrated ϵ_r^*-values (7.6) includes additionally to the uncertainties of the measured values U_m^* and U_0^*, those of the calibration constants $\tilde{K}_1$, K_2, $\tilde{K}_3$. These constants contain the measurement uncertainty of the reference system (mostly geometric considerations, see sec.7.3), samples and statistic considerations of the PP evaluation.

Since the test samples in sec. 7.4 have been chosen to represent a variety of materials (solid, liquid, fine granular) and include a vast amount of measurement series, the best estimation of total systematic uncertainties is obtained directly by the values in fig. 7.9 and 7.10. Since the reference data are the most accurate data available for the test samples (see sec. 7.3.1), the variation of the PP data includes all points of accuracy considerations above. Thus the total measurement uncertainty of the PP-data is the sum of the defined systematic errors in sec. 7.4 and the statistical error obtained by each PP measurement.

For ϵ_r'-values being not within the defined calibration interval ($I \in [1, 5]$), the uncertainties of the uncalibrated measurement have to be taken, since the accuracy of PP for values above

the calibrated range is not guaranteed. Since the calibration of ϵ_r'' seems not too reliable, for the imaginary part permittivity values, the evaluation with (8.3) and the assumption of uncertainties in the range of not calibrated ϵ_r'-values is preferable. As mentioned in sec. 7.4, one big problem of the high variation of ϵ_r'' values to the reference might be their small order of magnitude. In fact this low value is connected directly to low values of U_m. A low signal amplitude causes high statistical errors as seen within several tests. Through the statistics of the time series this uncertainty is directly considered in the evaluation.
For the evaluations in the following sections, the measurement uncertainties worked out above are applied to the dielectric loss $\tan\delta$ and σ by their relations to permittivity ϵ_r^* (eq.3.13 and eq.4.11).

8.2 Dielectric properties of selected laboratory and Mars analogue samples

For selected materials, the dielectric properties, measured with PP, are presented in this section. If not stated otherwise, the measurement has been performed at room temperature. The uncertainties of the data points result from the considerations in sec. 8.1.
The comparison of the dielectric properties obtained with PP to other data is difficult, because of the general incomparability of the used samples, especially their inner chemical structure, bulk volume, water volume fraction and porosity. Especially for natural samples differences are to be expected, since the physical properties can vary on the scale of a few centimetres. For granular material this problem is even worse, due to mixing and de-mixing (Paranut effect) and other intrinsic texture changing processes. Nevertheless some comparison will be given. The focus lies in the characteristic spectral features of permittivity ϵ_r^*, dielectric loss tangent $\tan(\delta)$ and conductivity σ related to relaxation and conductive phenomena. The dc-conductivity is stated in case of the PP-measurement as the low frequency value of the measurement, which is generally 4 Hz.
Figure 8.1 shows the dielectric properties of a solid granite sample. In comparison to the data obtained by Strangway et al. [105], the real part permittivity ϵ_r' is in good agreement with the sample measured at 1 atmosphere ($7 < \epsilon_r' < 10$). The high low frequency increase of the PP-data can be assigned to additional H_2O assimilation of the sample and subsequent Maxwell-Wagner polarisation. The loss tangent of the PP data $\tan(\delta)$ agrees very well with the data obtained by the mentioned study ($0.1 < \tan(\delta) < 1$). The dc conductivity σ_0 for the dried granite sample used by Strangway et al. reaches values $< 10^{-13}$ Sm^{-1}. Although they didn't publish any dc conductivity data for the not dried granite sample they detected for a comparable sample an increase of dc conductivity of about 4 orders in magnitude when measuring under atmospheric conditions. If an increase of this order is assumed for the granite sample too, the PP-data value agrees well ($\approx 10^{-9}$ Sm^{-1}).

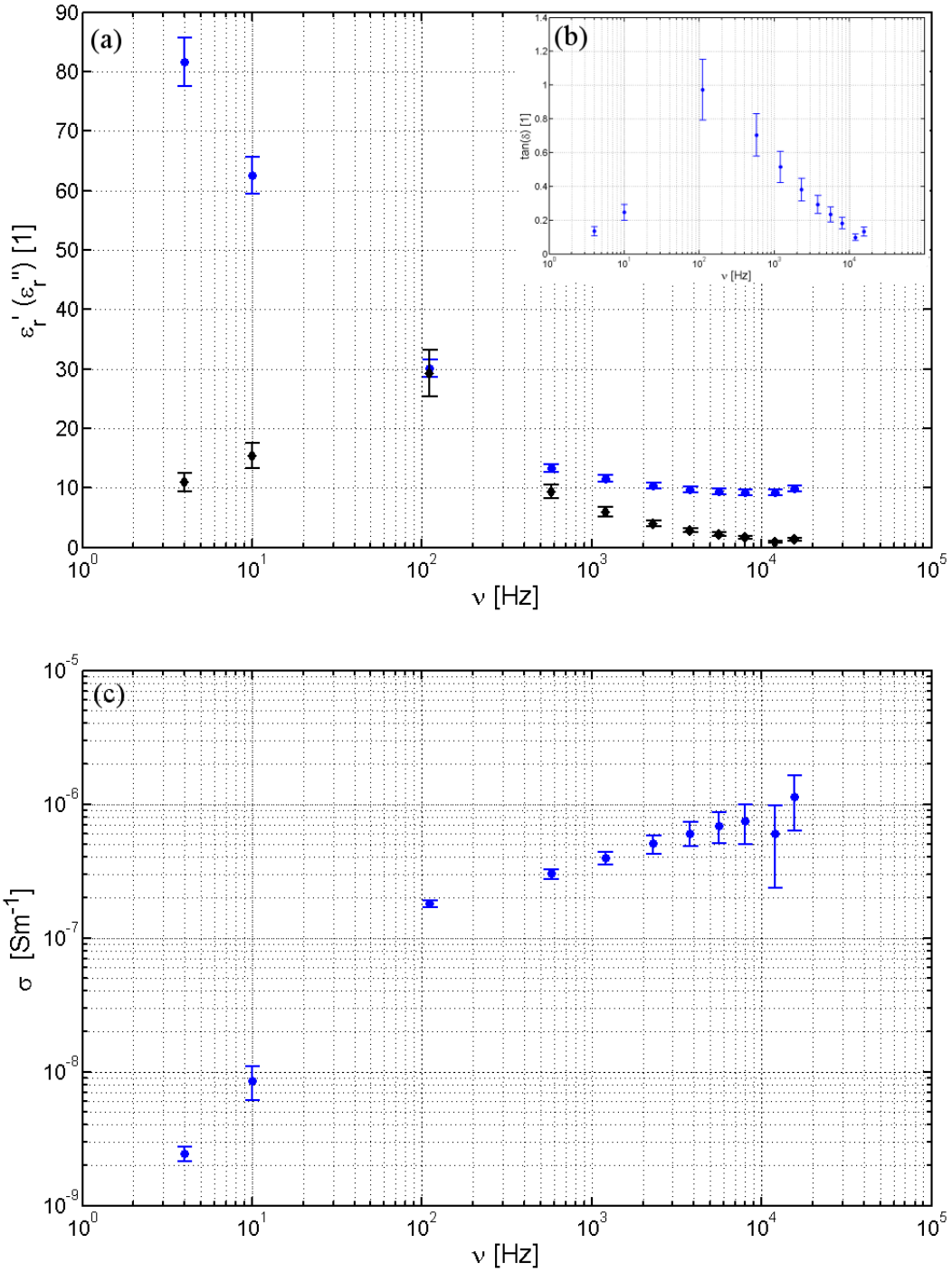

Figure 8.1: The permittivity ϵ_r^* (a) and loss tangent $\tan(\delta)$ (b) spectra of a solid granite sample obtained with PP are in good agreement with a study by Strangway et al. [105], who obtained ϵ_r' values between seven and ten. The dc conductivity σ_0 (see spectrum (c)) provides with $\approx 10^{-9}$ Sm^{-1} a comparable value compared to this study (see text).

In fig. 8.2 the dielectric properties of a snow sample at 255 K are plotted. A comparison to literature values seems to be difficult since the snow sample was not produced under controlled conditions. Nevertheless, to get some estimates of the values expected, Evans [106] published dc conductivity values in the range of 10^{-7}-10^{-9} Sm^{-1} for granular snow at 263-233 K. The static permittivity $\epsilon'_{r,dc}$ is estimated to be about fifteen. Evans published maximum loss tangents (relaxation frequencies) for city snow in the range of 10-25 kHz for temperatures between about 263-273 K. The relaxation frequencies are expected to be shifted to lower frequencies for decreasing temperatures.

Though the comparison of quantitative values of dielectric properties is difficult, a relaxation frequency in the kHz regime is typical. This relaxation is shown in fig. 8.2 at about 10 kHz. The low frequency dispersion of ϵ'_r is assigned to Maxwell-Wagner polarisation due to the heterogeneity (impurities) of the natural snow sample. Since there are no signs of dc-contributions in the ϵ''_r spectrum, a small peak results as a consequence of the Maxwell-Wagner polarisation.
The spectra of the Martian dust analogue sample Salten Skov [107, 108] (see fig. 8.3) show characteristic features of H_2O assimilation in the sample, which has been stored at ambient laboratory conditions. Both real and imaginary part of permittivity show a significant increase at low frequencies due to Maxwell-Wagner polarisation, respectively for ϵ''_r an effective sample conductivity increase. This results in a low frequency increase of loss tangent $\tan(\delta)$, too (see fig. 8.3). The PP behaviour to H_2O abundances in the material are discussed in more detail in sec. 8.4.
Figure 8.4 shows the dielectric properties of the Martian dust analogue sample JSC Mars 1A [109] at room temperature and at 255 K. The values can be compared to data obtained by Simoes et al. [91], who performed dielectric measurement on this sample at various temperatures, porosities and water volume fractions. A quantitative comparison to this study fails in general. The PP data, with sample porosity of 54 % [109], is dominated by a water content of 7.3 m% at RT, which affects the 255K measurement in form of frozen water too. In general the occurrence of H_2O manifests in a slight increasing of low frequency imaginary part permittivity values ϵ''_r for both measurements. The low frequency values of the ϵ''_r value at room temperature are higher than those at 255 K. The reason can be found in the higher conductivity of the RT measurement (see text below). A significant increase for the real part permittivity value ϵ'_r due to Maxwell-Wagner polarisation is not recorded, which is surprising due the determined comparable high water content. The most likely explanation for the missing polarisation characteristic may be, that the high uncertainties in the low frequency real part permittivity values suppress the dispersion. The JSC Mars 1A data obtained by PP at room temperature compared to that at 255 K shows no significant variations in the values of dielectric permittivty ϵ'_r. The sample at RT provides a higher dc conductivity, which is seen in the low frequency increasing of the ϵ''_r-value (fig. 8.4 (a)). This seems to be reasonable, because of the contained H_2O, which freezes at 255K. Most

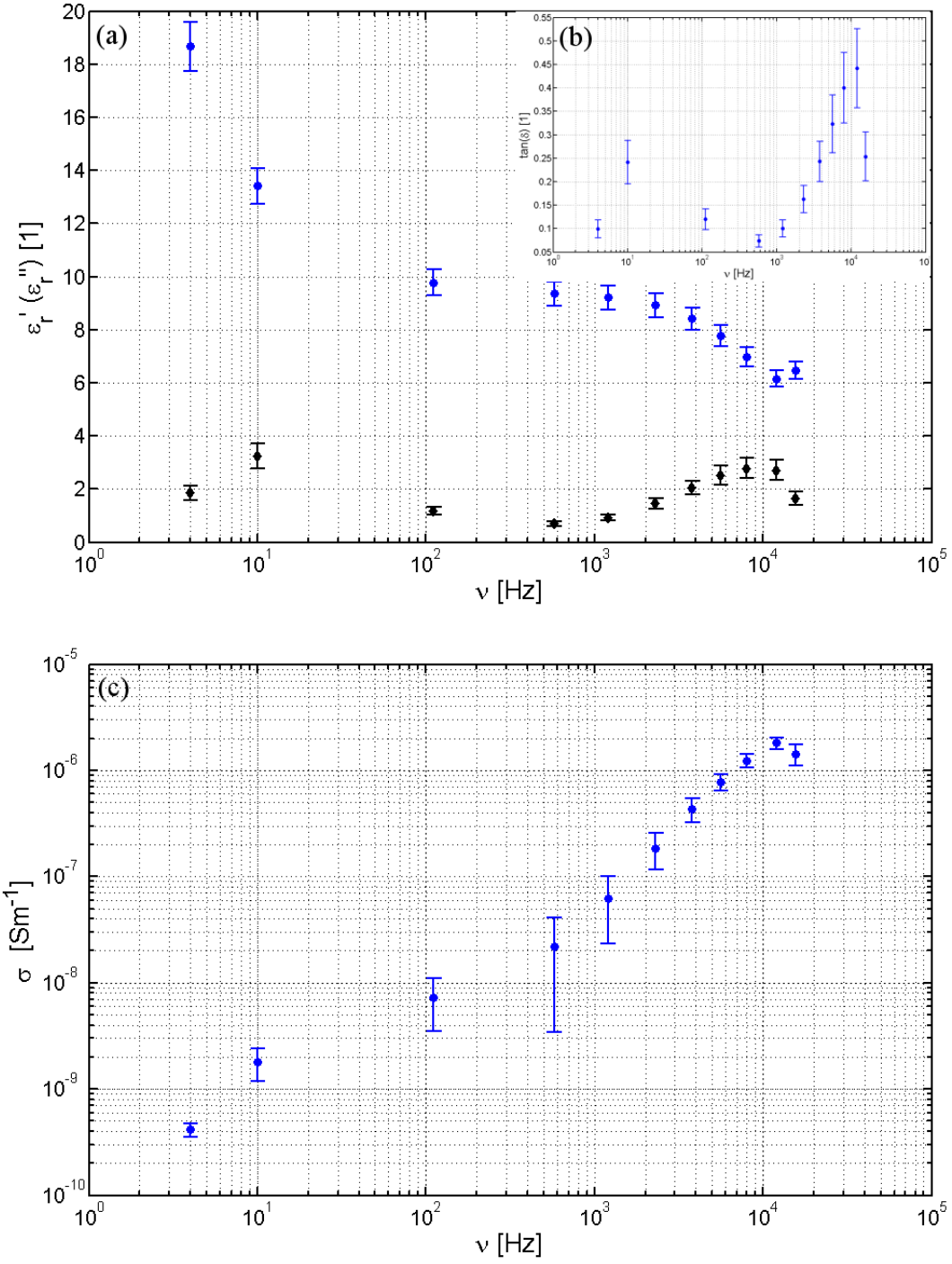

Figure 8.2: The dielectric properties ϵ_r^* (a), $\tan(\delta)$ (b) and σ (c) of a snow sample measured at 255 K. A comparison to other data is difficult, since the sample wasn't built under controlled conditions.

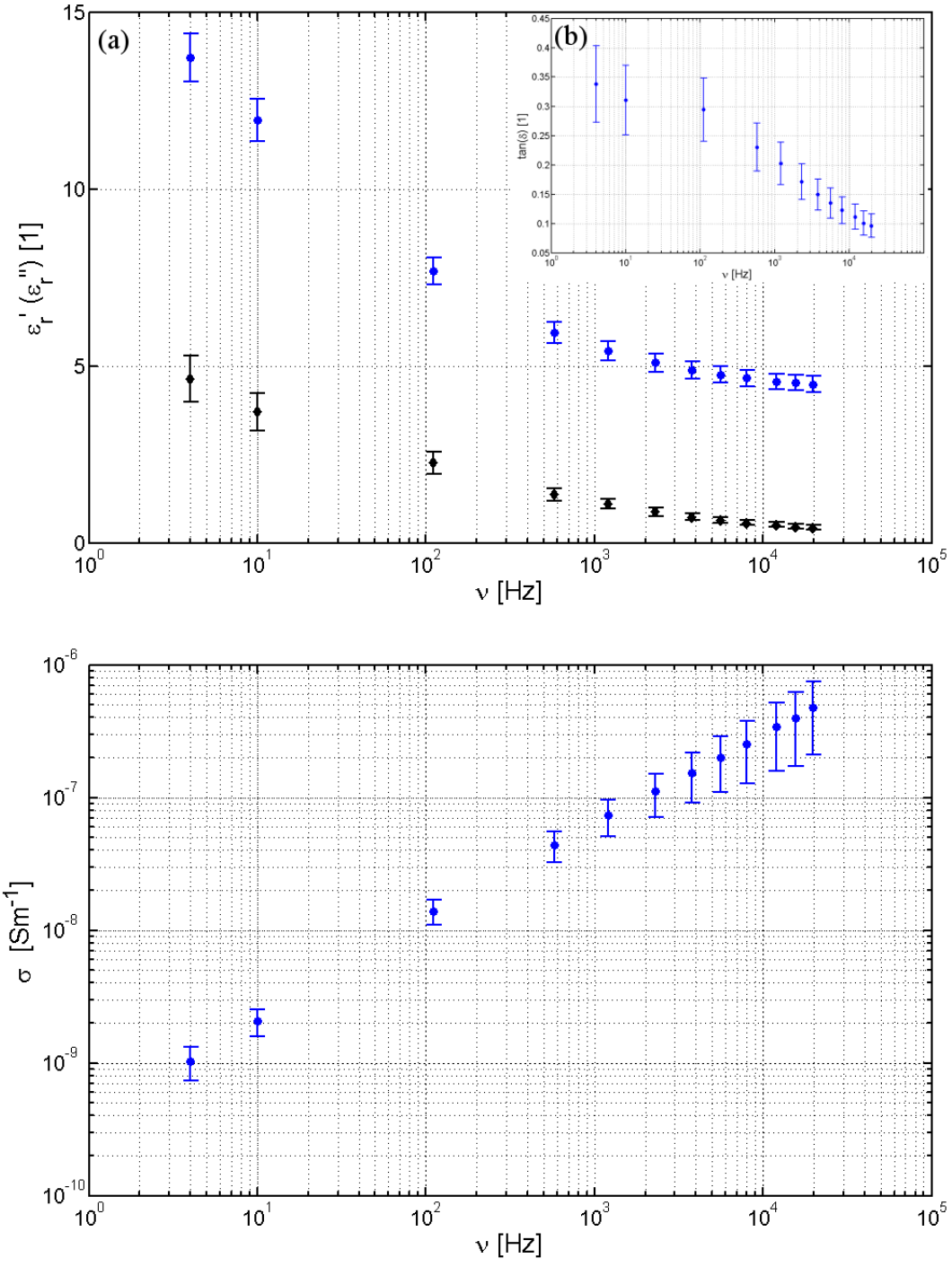

Figure 8.3: The permittivity ϵ_r^* (a), loss tangent $\tan\delta$ (b) and conductivity σ (c) of the Martian dust analogue sample Salten Skov are strongly influenced by water-abundances in the sample. As a consequence in each spectrum a low frequency dispersion arises.

Table 8.1: The static permittivity ϵ_{st}, permittivity at high frequencies ϵ_{inf}, dc conductivity σ_0, Cole-Cole parameter α, relaxation time τ_0 and the sum of squared errors χ^2 for real and imaginary part obtained by describing the PP data with the Cole-Cole model in fig. 8.5.

parameter	**JSCM 1A (RT)**	**JSCM 1A (255 K)**
ϵ_{st}	23.2	24.4
ϵ_{inf}	11.8	9.4
σ_0 [Sm^{-1}]	$10^{-8.95}$	$10^{-9.30}$
α	0.12	0.25
τ_0 (10^{-5}) [s]	3	7
χ^2_{re}	9.0	9.2
χ^2_{im}	2.1	1.9

significantly a clear shift of the resonance in the kHz regime occurs for the two temperatures. This shift arises also in the data of Simoes et al.. The resonance is moved to lower frequencies for the low temperature sample.

Unfortunately the relaxation peaks haven't been resolved in their full bandwidth, because of their occurrences at the end of the PP frequency range. To get an estimate for the true relaxation frequency, the Cole-Cole model (4.18) has been applied to the data. The Cole-Cole function including the conductivity term describes well the data obtained with PP (see fig. 8.5). The parameters used for the least square approximations are listed in tab. 8.1. The value of ϵ_{inf} had to be guessed to 80% of the last data point for both temperatures. This seems to be reasonable, because it was not likely that the PP-data includes this value. The slightly higher dc-conductivity value used in the model for the room temperature measurement follows the general trend of the imaginary permittivity data (see fig. 8.4 (a)). The general dc conductivity used for this model ($\sigma_0 \approx 10^{-9}$ Sm^{-1}) lies in the range of the low frequency PP data. The shift in resonance to higher τ_0 values is in agreement with the theoretical predictions in (3.22) ($\tau_0 \propto e^{\frac{1}{T}}$ ($\tau = \nu^{-1}$)). The broadening of the relaxation peak for the lower temperature data is possibly a direct result of multiple relaxations in the sample in the kHz-range. This seems reasonable, if one thinks of additional ice relaxations (see fig. 8.2), which occur consequently after freezing the water assimilated in the JSC Mars 1A sample.

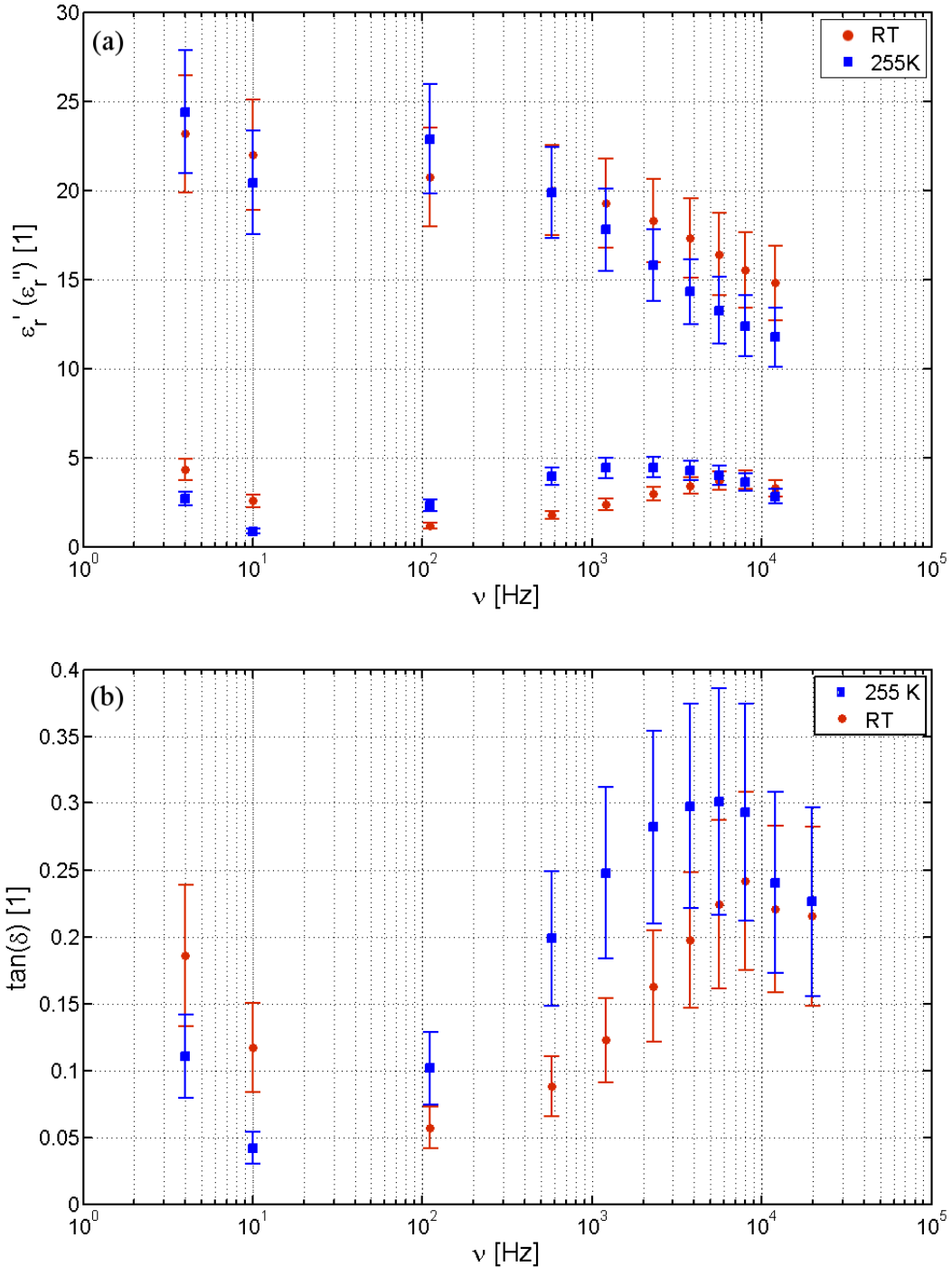

Figure 8.4: The dielectric properties of the Martian dust analogue sample JSC Mars 1A at room temperature (RT) compared to those obtained at a temperature of 255 K. Shown are (a) ϵ_r^* and (b) $\tan(\delta)$. Most significantly the loss peak in the kHz-regime shifts for different temperatures.

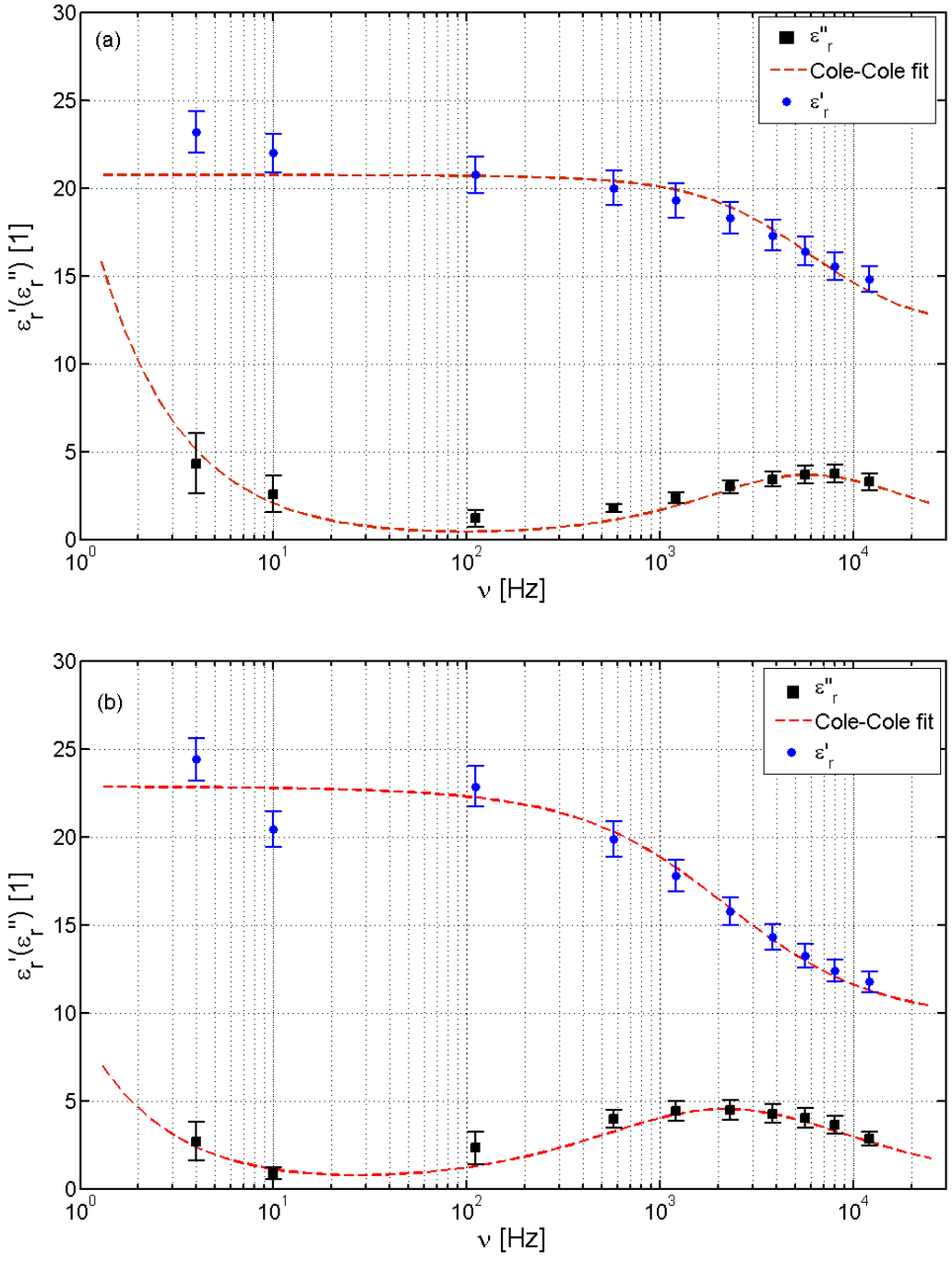

Figure 8.5: The Cole-Cole model has been applied (a) to the JSC Mars 1A data at room temperature (RT) and (b) at 255 K. The model shows a good agreement to the data. Model paramters are listed in tab. 8.1

8.3 Detection of inhomogenities and layered structures

The ability of PP to detect inhomogeneities like layer boundaries or inclusions along its penetration path was tested. Figure 8.6 shows a typical signal obtained with PP for a sample with an inclusion. In this case the inhomogeneity was a sphere of 10 cm diameter filled with H_2O. The plastic sphere was embedded in glass beads ($\epsilon'_{r,g} \approx 4$) at ($2.2 \pm 0.2$) cm depth (centre of sphere at $\approx$ 7 cm depth). PP was moved laterally above the inclusion. The operating frequency was 111 Hz. As a characteristic feature, a minimum of

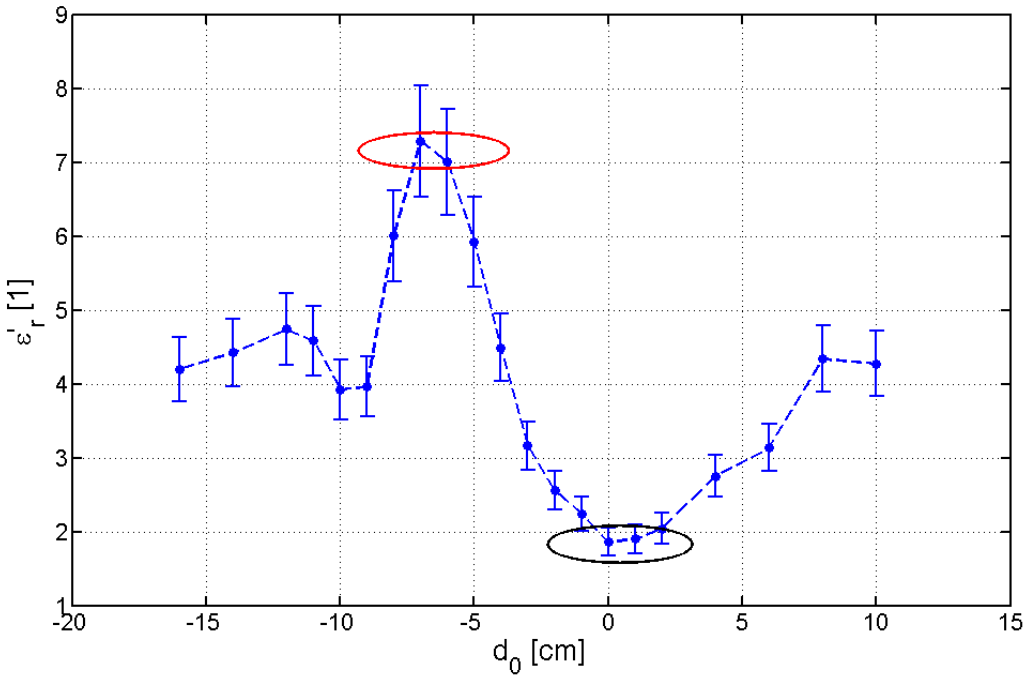

Figure 8.6: The figure shows the typical signal for a lateral movement of PP above an inclusion. Marked are typical maxima and minima. The x-axis indicates the relative centre position of PP lateral to the inclusion. The measurement is explained in the text.

ϵ'_r is detected, when the centre of PP is above the inclusion ($d_0 = 0$ cm). Moreover, due to the sensitivity pattern of a Wenner-α array a maximum is detected, if the inclusion is between the transmitting and the following receiving electrode [110] ($d_0 = -7$ cm). These two characteristic positions are marked in fig. 8.6.
Unfortunately, this characteristic maximum sometimes is suppressed, due to the strong main minimum at the PP centre position. In fig. 8.7 the evaluation in terms of signal voltage amplitude variation ΔA in comparison to the host material signal is shown for a half sphere (6 cm diameter) embedded in polystyrol. The measurement was performed with a 10 kHz transmitter-frequency. The half sphere was filled with H_2O and put at a depth of $z_{pp} = (5.5 \pm 0.5)$ cm. The same measurement has been performed with the half sphere filled with granular granite at $z_{pp} = (3.0 \pm 0.2)$ cm depth. When moving PP above the inclusions,

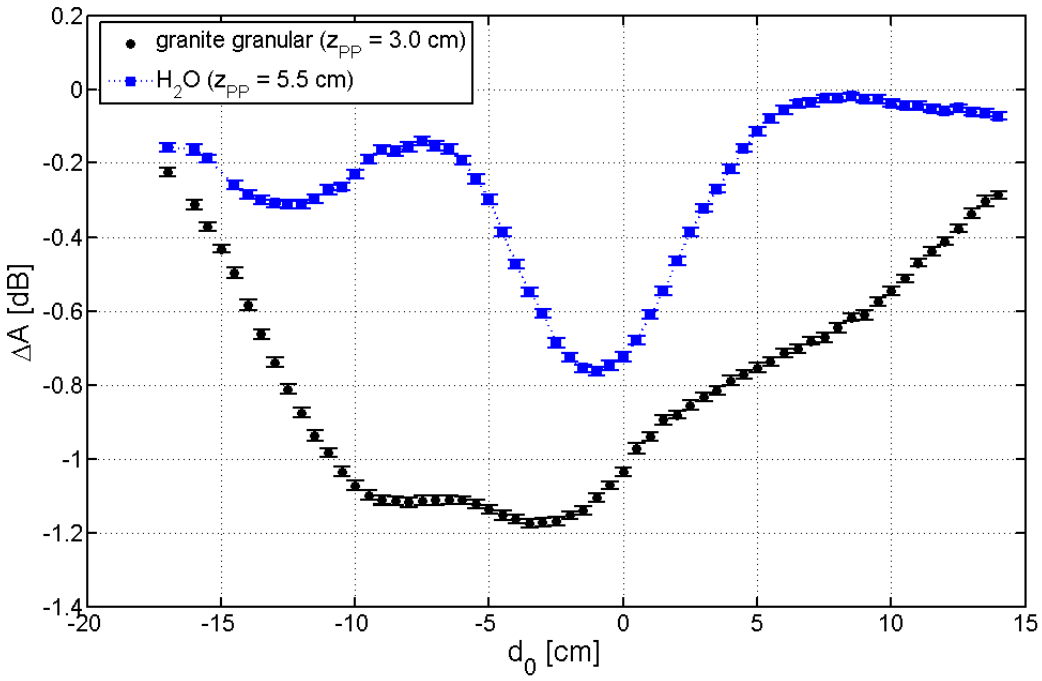

Figure 8.7: For a 6 cm half sphere filled with granular granite (distance to PP $z_{pp} \approx 3$ cm) or H_2O ($z_{pp} \approx 5.5$ cm) the maximum feature of the amplitude variation ΔA is damped by the main minimum at the electrode centre position. The measurement frequency was 10 kHz.

both measurements show the expected minimum at the electrode centre position. Since both material posses a higher conductivity σ than the host material polystyrol, this minimum in amplitude is the signal, which is theoretically expected from the potential calculation (eq. 4.20). The peak, in front of the main minimum at the position of $d_0 \approx -7$ cm, is the second characteristic peak for the Wenner-α array. These peaks are damped by the main minimum. The most likely explanation for the damping of the maxima in comparison to fig. 8.6 is, that the measurement reported in fig. 8.7 was performed in low density polystyrol as host material, which has a permittivity of $\epsilon'_{r,p} \approx 1.2$ (In fig. 8.6 the host material was glass beads with a ϵ'_r-value of about four). Thus the higher permittivity contrast of granular granite ($\epsilon'_{r,g} \approx 4$) and H_2O ($\epsilon'_{r,h} \approx 80$) to the host material can cause this strong signal. A more sophisticated consideration is needed for the evaluation of the amplitude variation in fig. 8.8. The plot shows the amplitude variations to the homogeneous host material while moving PP laterally on a polystyrol layer with various embedded inhomogeneities (see picture 8.8, right). The measurement has been performed twice, for a distance to the inclusions of about 4.5 cm (blue dots) and for a distance of about 2.2 cm (green squares). The lateral positions on the x-axis are labelled in fig. 8.8 (right). For the measurement at 4.5 cm distance the two minima at position 6 and 10 indicate the big central inclusion in fig. 8.8 (right). Both data sets provide a lot of features, which are shown in the plots underneath. The origin of the occurrence of the maxima and minima in the 3D plot can

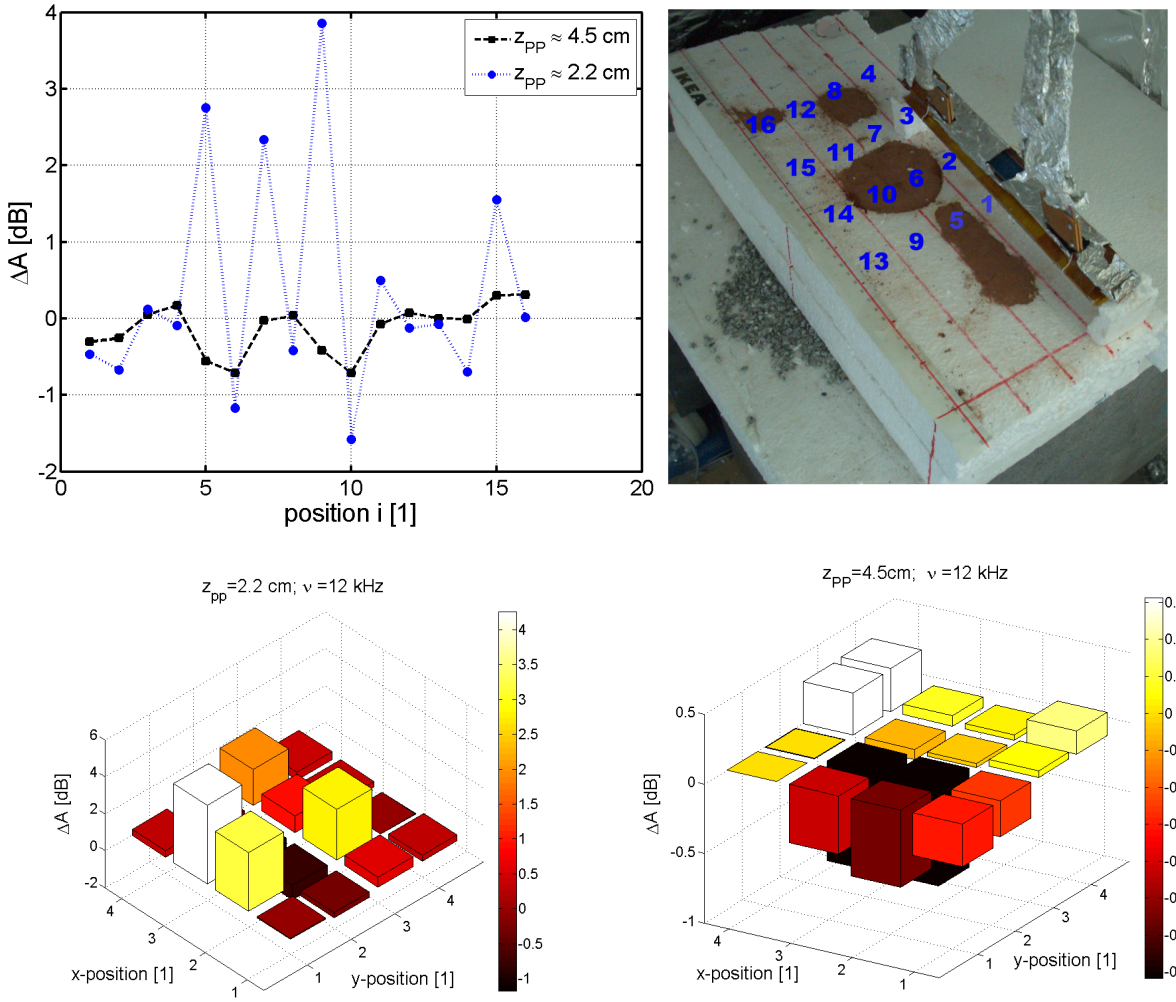

Figure 8.8: PP was laterally moved above the inclusions shown in the figure at a distance of 2.2 cm (green squares) and 4.5 cm (blue dots). The positions are marked in the same figure. The main minima of the 4.5 cm measurement are expected to originate from the big centre inclusion in the picture to the right (6,10). The data of the 2.2 cm measurement provides a lot of features, which are better resolved by the underneath 3D plot.

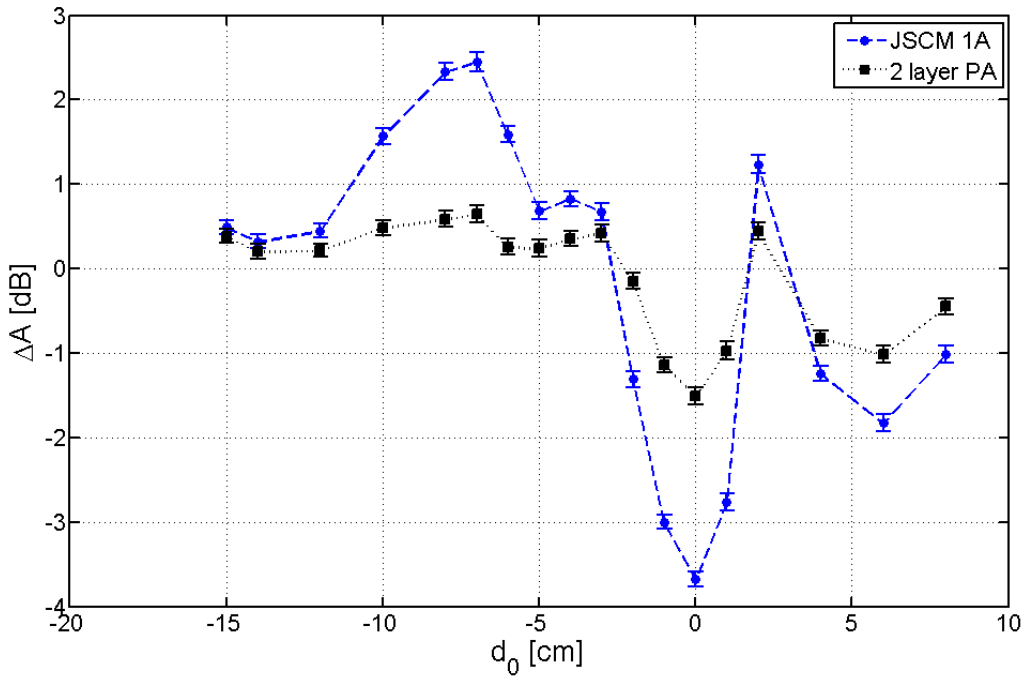

Figure 8.9: Two Poyamid plates sandwiching air (red squares) and JSC Mars 1A (blue dots) define a boundary between two polystyrol blocks. PP shows for both measurement cycles the expected minima and maxima in the amplitude change ΔA. The features at the end of the plot may be due to edge effects in the apparatus. The x-axis shows the centre position of PP relative to the boundary d_0.

only be guessed, since multiple signals overlap in this evaluation. It is expected, that the main minima (position 6 and 10) are resolved as main damping positions for both distances in the 3D plot. Probably the difference in the signal between the two operating distances directly in front of position 6 and 10, could be adressd to the characteristic maximum in the PP signal. This maximum dominates for the near distance measurement and causes the gain in amplitude. For the 4.5 cm measurement this maximum only damps the signal minimum (Note the order of magnitude in the scales at the right of each plot: The 2.2 cm signal is higher in general). The signal increase for the 4.5 cm measurement for the two last positions in the edge rows, is probably caused by limited sample size. PP detects the low permittivity boundary to air. In general more valuable estimates will only be possible by methods of data-inversion (see sec. 8.3.1). For the sake of completeness fig. 8.9 shows an example for the detection of a boundary. As boundary two 1 mm thick plates of Polyamid sandwiching a 1 mm thick sample have been put vertically between two polystyrol blocks. The space between the PA plates was left empty (2 PA) in a first run and then filled with JSC Mars 1A. The measurement frequency was 111 Hz. As shown in fig. 8.9 the significant minimum for ΔA indicates the boundary, if the centre of PP is placed onto the PA-plates. As expected the signal varies stronger for the (more) conductive JSC Mars 1A sample (compared to air). The typical maximum occurs when the boundary is between inner and

outer electrode. This boundary is better resolved for the filled PA plates. The features at the end of the plot may be due to edge effects in the apparatus.

8.3.1 Geophysical data inversion

Data sets as shown in fig. 8.8 are difficult to analyse, since the data points in the graph originate from various sources, inhomogeneities, different geometries and physical properties. For problems like these it is inefficient to compare only the measured data y_d with data obtained with a model y_m describing the general problem ("forward modelling"). The work with data inversion methods is preferable.
Inversion theories are based on the idea of varying the model parameters, until an agreement to the measured data is obtained. Thus, optimising the model through least squares or other numerical algorithms leads to the best solution.
As an example a data set described by Maxwell's equations (eq. 4.2-4.4), as an obtained resistivity pattern of the ground, will be explained by varying e.g. the parameters ϵ and μ within expected shapes and geometries. The optimised model of the ground then provides the best estimates for the real geometries and properties of the ground. To obtain these best estimates, prior information is put in the evaluation (e.g. expected ϵ-values), which result from experience.
These methods are most efficient to explain complex geophysical data, but it is beyond the scope of this thesis to develop and apply them.
For PP the proof of ability to detect layers and inhomogeneities as given by the data above is sufficient for the actual status of instrument development.

8.4 Determination of ice/H_2O content

As used in the previous sections with H_2O the liquid phase of water is meant. The term *ice* is used for the solid phase of H_2O in this section.
The detection of H_2O and ice with PP is an important scientific objective. To determine the instrument behaviour for various H_2O and ice concentrations in a sample, a set of test measurements has been performed.
In general the occurrences of H_2O components in a sample cause a characteristic low frequency dispersion in the real part permittivity ϵ'_r [111] and influence the sample conductivity, respectively the imaginary part of permittivity ϵ''_r. In the following considerations the focus will be given to the real part effects, since those are dominant.
The influence of H_2O on the dielectric spectra was shown in sec. 8.2. As an example the comparison of the real part permittivity spectrum in fig. 8.3 (a) to one obtained by the Novocontrol spectrometer (see 7.3) in fig. 8.10 demonstrates the effect of the H_2O traces. The PP measurement shows a very good agreement to a data set obtained by the reference

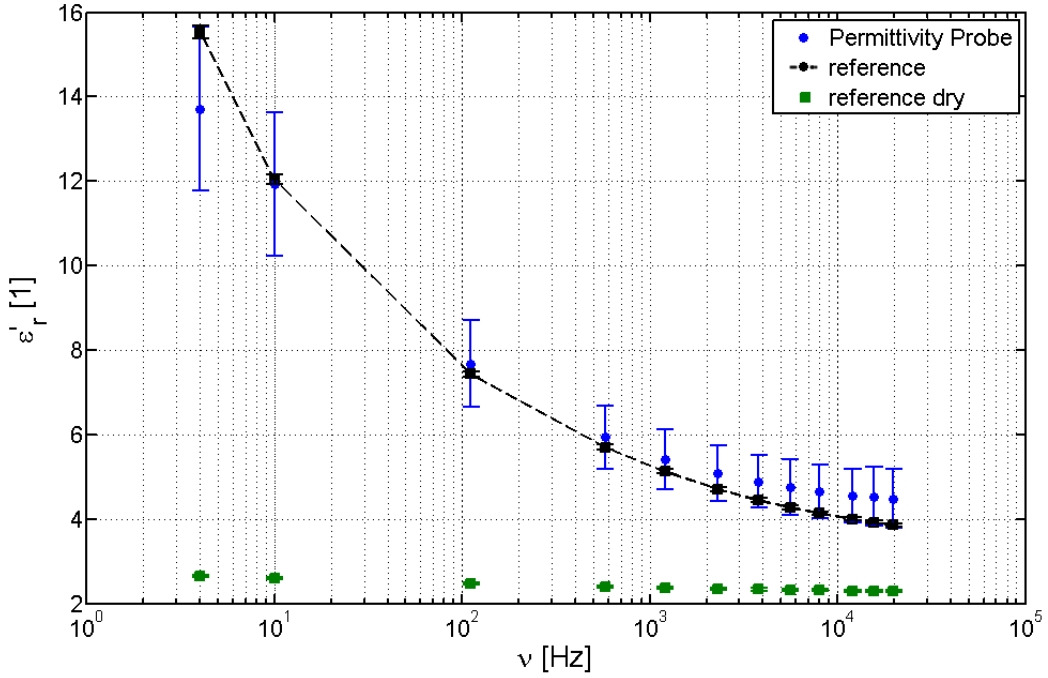

Figure 8.10: The Salten Skov ϵ'_r spectrum (blue dots) agrees very well with the data obtained by the Novocontrol spectrometer (dashed curve) for a Salten Skov sample containing (1.3 ± 0.1) m% H_2O. For comparison the dry sample result obtained with the reference instrument (black squares) is plotted.

instrument for a Salten Skov sample with (1.3 ± 0.1) m% (mass percent) H_2O. For comparison the reference measurement for the dry Salten Skov sample is plotted, in which no low frequency dispersion occurs. The general offset, respectively the higher permittivity-values, occurring between dry and water bearing sample are a direct result of H_2O abundances, too. The significant low frequency dispersion for the Salten Skov sample originates from Maxwell-Wagner polarisation. This significant fractional power law dispersion was evaluated for the Salen Skov sample and for the solid granite sample of sec. 8.2. It is plotted in fig. 8.11. These spectra follow an inverse fractional power law as described by (3.30). According to this function a least square fit in the form

$$\epsilon'_r = a + b\nu^{-\alpha} \tag{8.5}$$

has been applied on the data. These fits show very good agreement to both data sets. The used parameter and fit values are listed in tab. 8.2. The χ^2-value for each fit is stated too. The best fit values of the parameter α are in good agreement with those obtained by Knight and Nur [33]. The small variation of the granite sample in comparison to their data ($0<\alpha<0.4$) is most likely caused by the different frequency range in which the measurements were performed. Knight and Nur worked with excitation frequencies higher than 60 kHz, whereas the maximum frequency of PP is 20 kHz. The evaluation of ν instead of ω as in the work of Knight and Nur, doesn't affect the critical exponent. The 2π-shift of the x-values

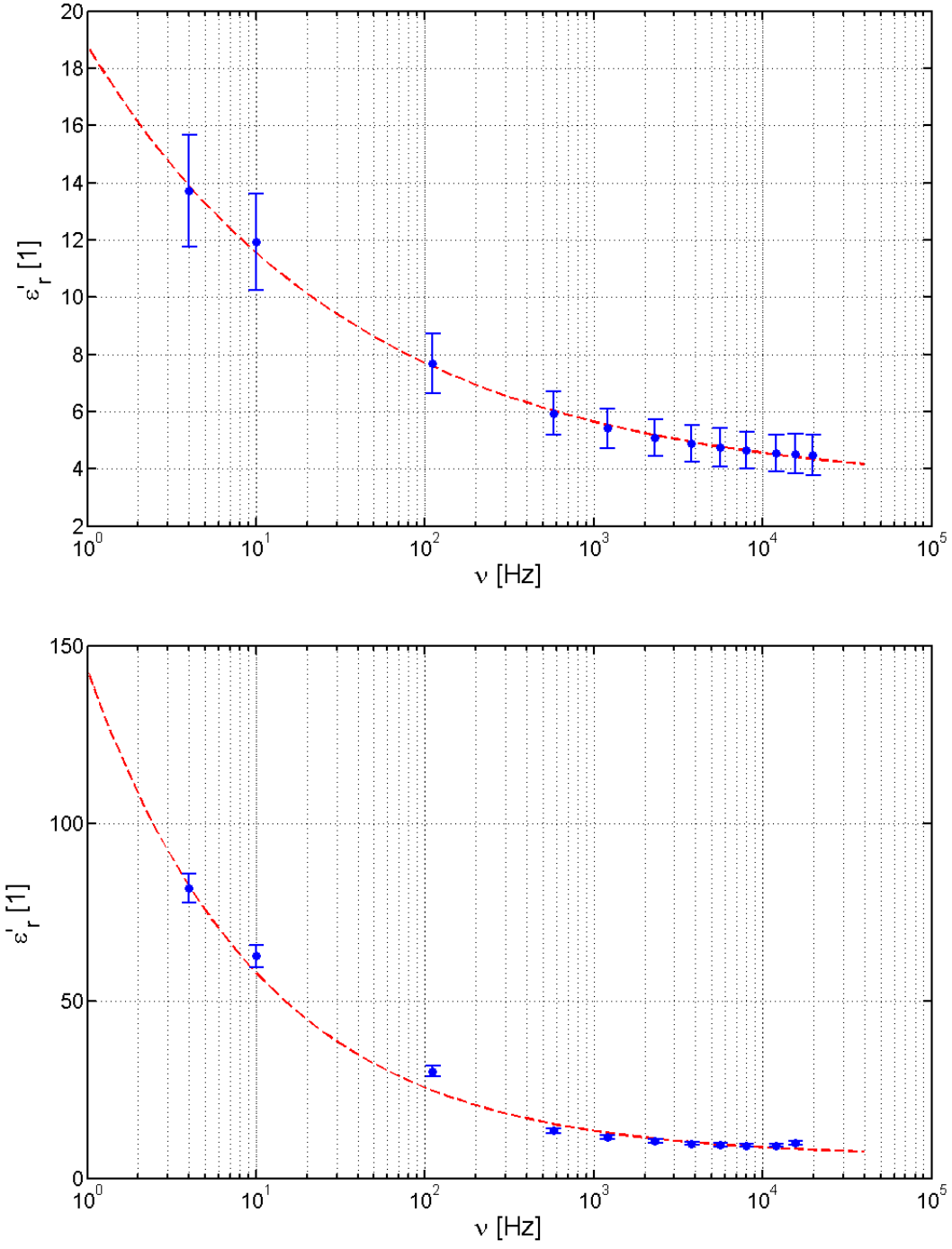

Figure 8.11: The typical fractional power law low frequency dispersion for the Salten Skov (upper plot) and the solid granite sample (lower plot). The evaluated fit values are listed in tab. 8.2

Table 8.2: The table lists the fit values a, b and α of eq. 8.5.

parameter	Salten Skov	granite (solid)
a	3.3 ± 0.4	6.0 ± 0.2
b [Hz]	16 ± 2	137 ± 5
α	0.27 ± 0.01	0.42 ± 0.02
χ^2	0.3	62

concerns only the parameters a and b.

To test the instrument behaviour to various H_2O fractions in a sample, different H_2O fractions have been included into a Salten Skov sample. After the measurement the real water fraction was determined by sampling the H_2O-mass fraction with a moisture meter [112] for at least 3 points in the material. This mass fractions have been converted to volume fractions by considering the total sample mass, the bulk density of Salten Skov (1200± 50) kgm^{-3} and the H_2O-density (998 kgm^{-3}).[9]

As shown even very small amounts of H_2O in the sample influence the ϵ'_r-value drastically. Unfortunately, no theoretical or empirical model of sec. 3.4.2 was able to describe the data set. Possible reasons for this mismatch are that most of them are only suitable for higher frequency ranges than that of PP and that they do not include Maxwell-Wagner effects. The discrepancies between the behaviour for the two plotted frequency-evaluations in fig. 8.12 and fig. 8.13 are not surprising, since the Maxwell-Wagner polarisation contributes more to lower frequencies (see sec. 4.1.1.1) than to higher ones. To describe the dependence between variation in the H_2O volume fraction Δf_{H_2O}, the variation in the water content to the not modified sample, and the measured permittivity ϵ'_r least square fits are plotted with the data set in fig. 8.12 and fig. 8.13. The parameter and fit values are listed in tab. 8.3. As shown for the higher frequency, the permittivity ϵ'_r shows a linear dependence to the H_2O volume fraction. A linear behaviour is observed too for low H_2O fractions for the low frequency measurement. At higher volume fractions Δf_{H_2O} the permittivity ϵ'_r increases exponentially. Both fits are drawn in fig. 8.13. The exponential fit describes almost the whole fractional H_2O range. Variations occur only at very low concentrations. Physically this exponential behaviour seems to be not realistic, because of the drastic increase of permittivity ϵ'_r. Nevertheless it describes the PP reaction to H_2O abundances, since higher H_2O fractions - respectively ϵ'_r-values higher than about 250 - would yield to a signal overload for this frequency.

[9] The value for the bulk density of Salten Skov is taken from Seiferlin et al. [113]. Since no compaction has been applied to the sample the "loose packing" value was chosen. This agrees with rough measurements of the bulk density by determining the sample mass to volume ratio. The error was included as a result of the uncertainty of this determination.

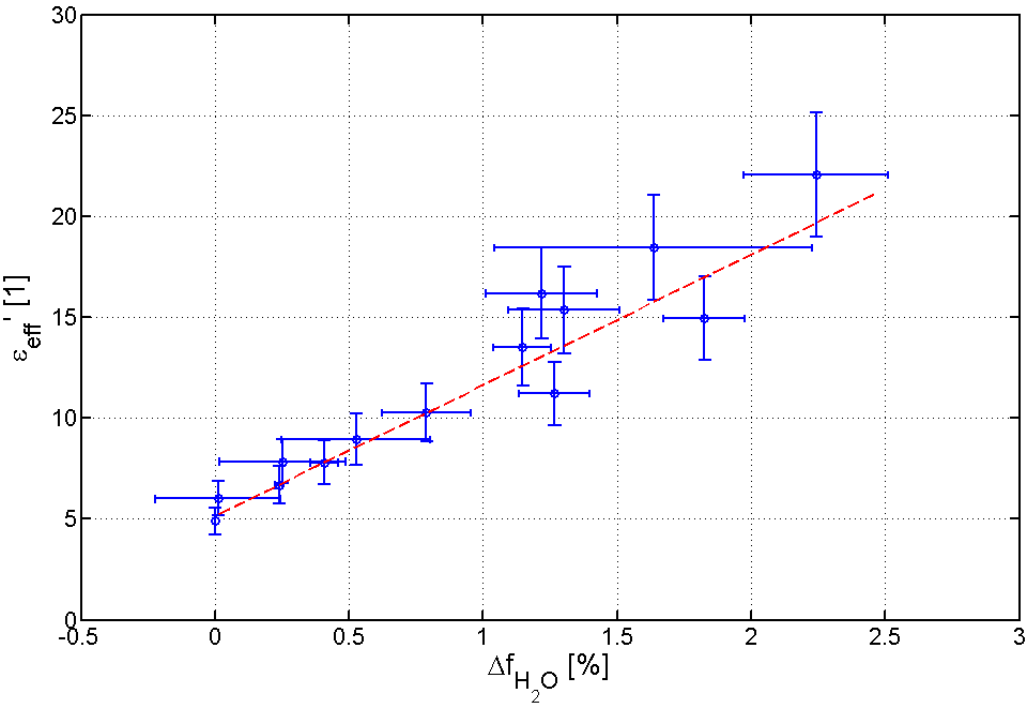

Figure 8.12: The Permittivity Probe shows a linear dependence in the ϵ'_r-increase due to the variation of the H_2O volume fraction Δf_{H_2O} to the non-modified sample for a source frequency of $\nu =$ 12 kHz.

Table 8.3: The parameters of the linear and the exponential fit for the results presented in fig. 8.13 and fig. 8.12. The high value for χ^2 of the exponential fit is a result of the uncertainty of the last data point.

model	$\epsilon'_r = a + b\Delta f_{H_2O}$	$a\ e^{(b\Delta f_{H_2O}{}^2)}$
interval [%]	[0,1]	[0.01, 2.2]
a	6.3 $\pm$ 0.1	2.3 $\pm$ 0.1
b	1500 $\pm$ 6	5000 $\pm$ 9
χ^2 ($10^{\ 3}$)	0.1	7.0

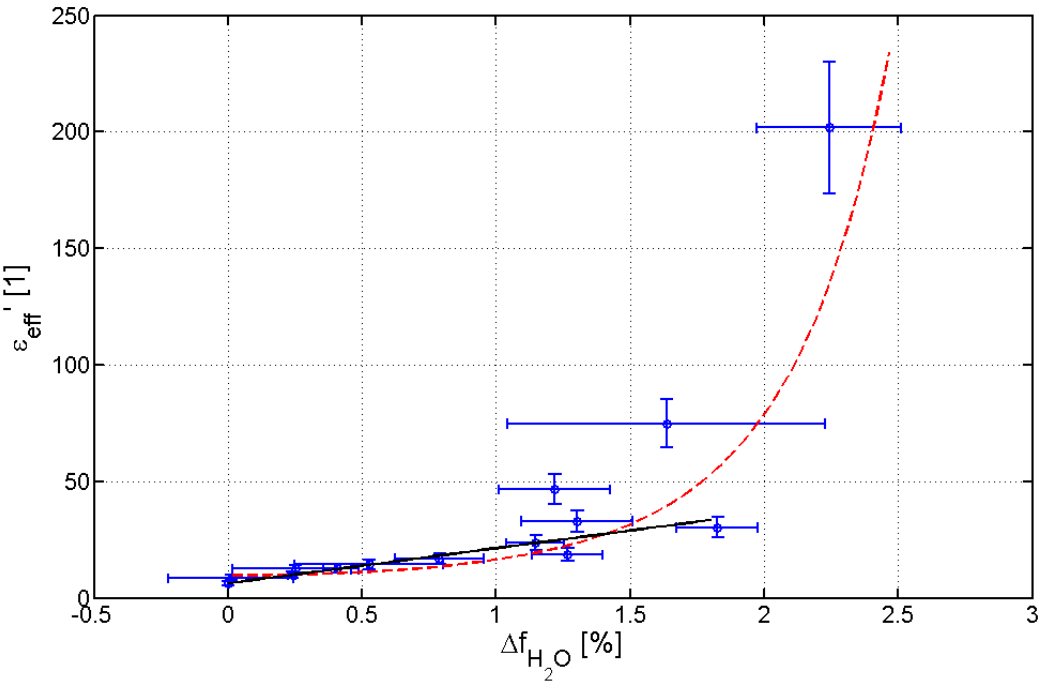

Figure 8.13: For a measurement frequency of $\nu = 1200$ Hz only small variations in the H_2O volume fraction Δf_{H_2O} to the untreated sample cause a linear increase of ϵ'_r. Higher variations ($\Delta f_{H_2O} > 1.5$ %) cause an exponential increase of ϵ'_r.

Small amounts of liquid H_2O are detectable with the HP^3-PP. Therefore diurnal and seasonal changes in the material properties resulting from the fractions of H_2O in the atmosphere will be recognised. Nevertheless the occurrence of H_2O on Mars is more likely in the form of H_2O-ice. The instruments ability to detect homogeneous variations in a sand/ice mixture was tested by varying continuously the ice (snow) content in a JSC Mars 1A dust analogue sample. Figure 8.14 shows the variations in the real part effective permittivity ϵ_{eff} as a function of ice volume fraction f_{ice} in the sample for a set of frequencies in the kHz range, which are supposed to be less influenced by potential H_2O-effects. Unfortunately it was not possible to guarantee a homogeneous mixture higher than an ice volume fraction of $f_{ice} >$ 37.5 %, because of ice agglomerations causing lumps of ice to form in the sample. Figure 8.14 shows that there was a significant variation in ϵ_{eff} for the JSC Mars 1A/ice mixture compared to the pure JSC Mars 1A sample even for very low fractions of ice. The ϵ_{eff} value is higher than common mixing models (see sec. 3.4.2) would predict. To explain this high value an additional high permittivity phase in the mixture has to be considered. This phase originates from the heterogeneity (Maxwell-Wagner polarisation) of the sample. Possibly it is related to so called "unfrozen" water (adsorbed water) that appears in a liquid-like state below the triple-point [67]. The energy to create additional unfrozen water within the mixture could have been applied when mixing the sand/ice-sample.
To describe the data set, the same model as Stillman et al. [30] used has been applied to the data (eq.3.28). The results of the model are compared to the PP data in fig. 8.14.

The model includes the pure JSC Mars 1A permittivity, the pure ice permittivity and the permittivity of a third phase, which was chosen to be the water permittivity (ϵ_{r,H_2O}). The volume fractions of the different materials is given by the measurement. It is expected that the volume fraction of the third phase, which describes the fraction affected by H_2O, is not constant for the various ice-to-sand ratios. The host particles for possible adsorbed H_2O decrease with the volume fraction of the analogue sample. Consequently the volume fraction of the high permittivity phase has been chosen to be dependent on the sand volume fraction. A least squares evaluation of (3.28) for different parameters γ and H_2O-affected-phase fractions, led to a critical exponent of $\gamma = 1$. Consequently the model is reduced to the Maxwell-Garnett formulation (eq. 3.25). The best estimate for the H_2O-affected volume fraction is obtained for 19% of the JSC Mars 1A value. At a first view this is a very high value compared to the ice volume fraction (see fig. 8.14), which is even less than this value for the very first data points (19% of the sand content is general in the order of 10% in total). Nevertheless, this model seems to be reasonable, if one considers that H_2O was frozen within the JSC Mars 1A sample too and the high permittivity phase is not liquid water. This third phase describes rather the volume fraction of analogue material which is affected by H_2O than its volume fraction itself. The model describes the data for frequencies higher than 576 Hz. It is possible that, at the lower end of the selected frequency range, the high permittivity phase dominates the effective permittivity value ϵ_{eff} (see sec. 4.1.1.1). This dominant phase suppresses the variation in real part effective permittivity ϵ_{eff} especially for the variation of low ice fractions.

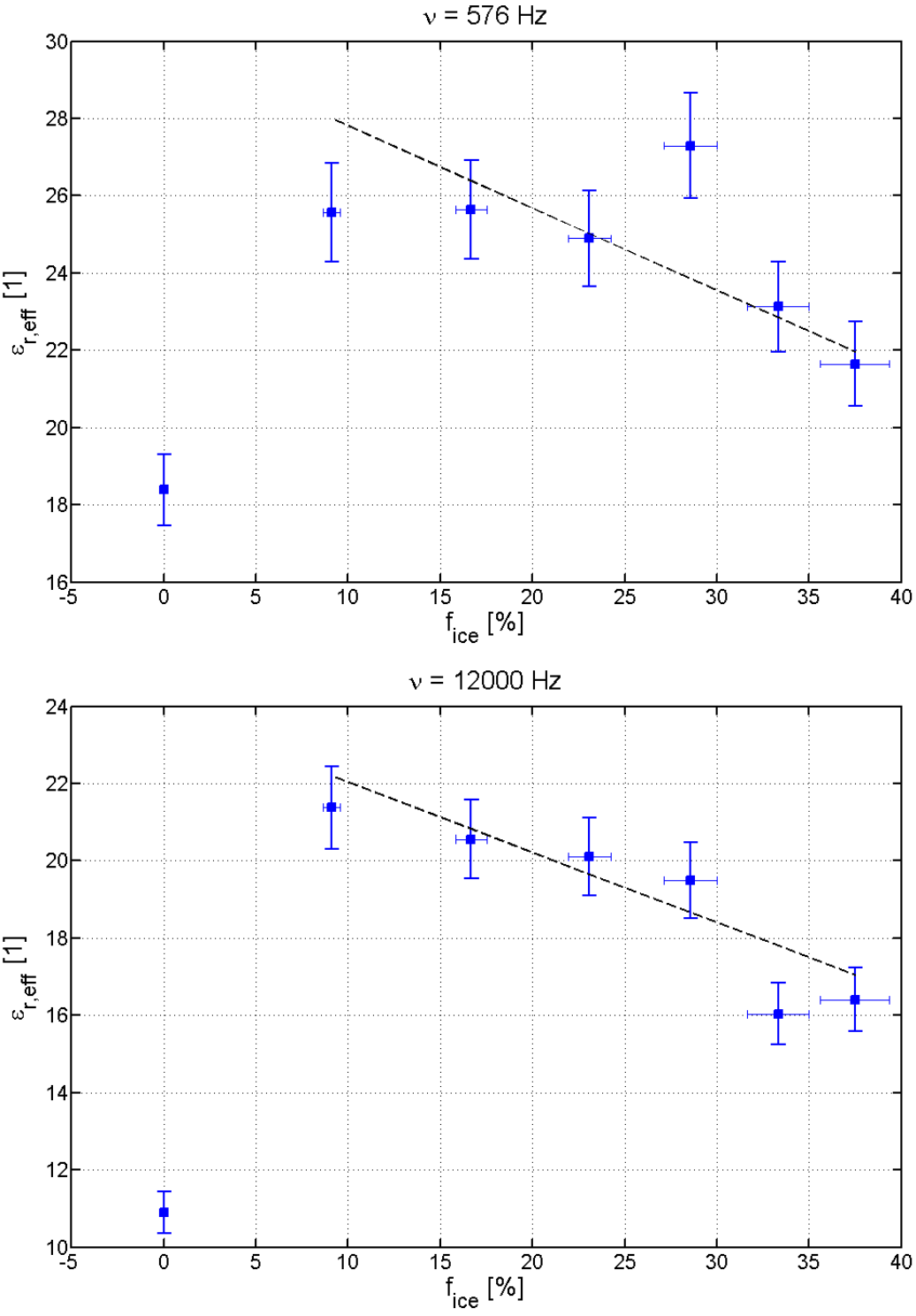

Figure 8.14: The real part effective permittivity (ϵ_{eff}) dependence for the snow volume-ratio f_{ice} within a JSC Mars 1A sample was tested for a set of frequencies and compared to the evaluations by Stillman et al. [30]. For PP the used model was reduced to the Maxwell-Garnett formulation. Additional to the sand and ice phase a third H_2O-affected phase had to introduced to describe the data (see text). The Maxwell-Garnett model (red line) is in good agreement with the PP data for frequencies higher than 576 Hz.

CHAPTER 9

Conclusions and future work

With the presented work the science performance of the HP^3-Permittivity Probe (PP) has been validated. This instrument within the **H**eat-Flow and **P**hysical **P**roperties **P**ackage (HP^3) is able to

- determine the electrical properties of a sample material with a relative uncertainty less than 5 % for the real part permittivity ϵ_r' and about 10 % for its imaginary part ϵ_r'' in the calibration interval,
- recognise local imhomogeneities like layer boundaries and inclusions along its penetration path
- and to detect liquid H_2O and H_2O-ice abundances within a sample.

Consequently, PP is able to determine variations in geometry and H_2O abundance within a material and its total mission time. If PP will be part of a Mars mission, this will provide clues to state the phase of H_2O and its abundance in the Martian atmosphere within diurnal and seasonal cycles. The inner structure of the Martian surface and sub-surface will be determined in centimetre-scale resolution. Additionally, the high accuracy of real part permittivity evaluation will provide a good estimation of density variations within the subsurface. This will enhance the information obtained with the heat-flow probe within the instrument package.
For a detailed and accurate evaluation of the absolute H_2O volume fractions within the investigated material, several additional measurements have to be performed in future, which include variations of measurement temperature and variable grain sizes of the host material. For a precise understanding of possible measurement results obtained in a Mars mission in future times, these measurements generally have to be performed under Martian environmental conditions, respectively in low temperature and low pressure CO_2-atmosphere.

For the detailed evaluation of the data including layered structures and inhomogeneities, the transmitter and receiver pattern has to be experimentally determined free from other electromagnetic noise. With this knowledge methods of inverse theory can be applied to the data to reveal the real structural state of the investigated ground.
Tests have to be performed, which determine the influence of the other science instruments within the HP^3-sensor suite and PP. Especially the heat flow probe could be used to vary the environmental temperature and therefore increase the scientific output.
These, as well as every other measurement should generally be supported by numerical simulations. This is especially necessary, if PP will be on board a space mission, because the influence of other instruments and the lander/rover body have to be defined.
If the instrument development is completed, the calibration, based on the work in this thesis has to be repeated. If a higher accuracy for the imaginary part permittivity ϵ_r'' is required, a reference instrument working with the 4-point principle should be used. Such a set-up in principle could be obtained, by developing an own sample cell for the Novocontrol impedance spectrometer used for this work, since pre-selected connections for the actual high accuracy measurement cell could be switched to obtain a 4-contact device. Unfortunately it is likely that this change will decrease the overall measurement accuracy.
Within the science performance tests with the final version of the HP^3 instrument, the virtual rotation of the instrument by switching various electrode configurations will be tested. Enhancing this rotation, it is possible to select different transmitter gain for the two redundant electronic-boards. Therefore a better resolution within this 360° scan can be obtained. For a maximum resolution a tunable gain of each of the four transmitters is mandatory.
Finally, a broader operation frequency range would reveal a higher amount of spectral features within the test samples. Evidently each variation concerning the inner electronics of PP has to be feasible within the overall instrument design, especially considering size, mass, and power budget.

Apendix 1

Derivation of Clausius-Mossotti equation

The polarisation $\mathbf{P}$ is defined as mean dipole moment per volume $\langle \mathbf{u} \rangle$ (N is the number of contributing dipoles).

$$\mathbf{P} = \sum_i N_i \mathbf{u}_i \xrightarrow{(2.9)} \mathbf{P} = \sum_i N_i \alpha_i \mathbf{E}_{lok}(i) \tag{.1}$$

Inserting the definition of the Lorentz local field $\mathbf{E}_{lok}$ (3.6) and rearranging yields ($\mathbf{E}$ is the sum of the external field $\mathbf{E}_0$ and depolarisation field $\mathbf{E}_1$):

$$\begin{aligned}
\mathbf{P} &= \sum_i N_i \alpha_i (\mathbf{E} + \frac{\mathbf{P}}{3\epsilon_0}) \\
&= \sum_i N_i \alpha_i \mathbf{E} + (\sum_i N_i \alpha_i) \frac{\mathbf{P}}{3\epsilon_0} \\
\mathbf{P} - \sum_i N_i \alpha_i \frac{\mathbf{P}}{3\epsilon_0} &= \frac{\mathbf{P}}{3\epsilon_0} \mathbf{E} \\
\mathbf{P}(1 - \frac{1}{3\epsilon_0} \sum_i N_i \alpha_i) &= \sum_i N_i \alpha_i \mathbf{E} \\
\mathbf{P} &= \frac{\sum_i N_i \alpha_i}{(1 - \frac{1}{3\epsilon_0}(\sum_i N_i \alpha_i))} \mathbf{E}
\end{aligned}$$

When this expression for the polarisation **P** is substituted in the general relation to the field **E** (eq. 3.10) it follows:

$$\begin{aligned}
\epsilon_0(\epsilon_r - 1)\mathbf{E} &= \frac{(\sum_i N_i\alpha_i)}{(1 - \frac{1}{3\epsilon_0}(\sum_i N_i\alpha_i))}\mathbf{E} \\
\epsilon_0(\epsilon_r - 1)(1 - \frac{1}{3\epsilon_0}(\sum_i N_i\alpha_i)) &= (\sum_i N_i\alpha_i) \\
(\epsilon_r - 1)(\epsilon_0\frac{1}{3}(\sum_i N_i\alpha_i)) &= (\sum_i N_i\alpha_i) \\
(\epsilon_r - 1)\epsilon_0 - \frac{1}{3}(\epsilon_r - 1)(\sum_i N_i\alpha_i) &= (\sum_i N_i\alpha_i) \\
(\epsilon_r - 1)\epsilon_0 &= \sum_i N_i\alpha_i + \frac{1}{3}(\epsilon_r - 1)(\sum_i N_i\alpha_i) \\
(\epsilon_r - 1)\epsilon_0 &= (\sum_i N_i\alpha_i)(1 + \frac{1}{3}(\epsilon_r - 1)) \\
\frac{(\epsilon_r - 1)\epsilon_0}{1 + \frac{1}{3}(\epsilon_r - 1)} &= \sum_i N_i\alpha_i \\
\frac{3(\epsilon_r - 1)\epsilon_0}{3 + \epsilon_r - 1} &= \sum_i N_i\alpha_i \\
\frac{\epsilon_r - 1}{\epsilon_r + 2} &= \frac{1}{3\epsilon_0}\sum_i N_i\alpha_i
\end{aligned}$$

This is the expression of the Clausius-Mossotti equation, which includes the Lorentz local field intrinsically. It relates the macroscopic permittivity to the polarisability of a medium.

Apendix 2

Temperature dependence of Polyamid 6 sample

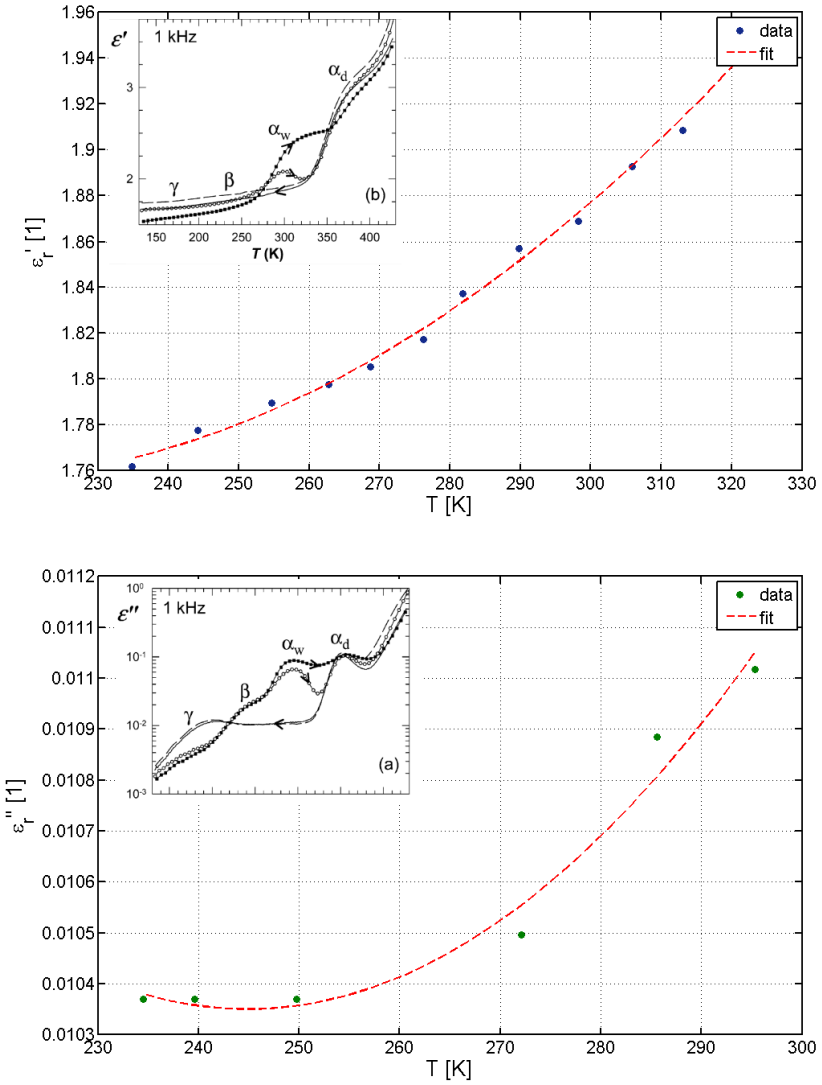

Figure .1: The fitted data of Laredo et al. [89] for the temperature range in the laboratory (the solid line with right to left arrow in the reference is described). The considered real part (above) as well as imaginary part data is decribed by a polynomial fit with degree 2. The fit values are listed in table .1.

Fit values

Table .1: Fit values a, b and c, and least square χ^2 for the polynomial fit of degree 2 in fig. .1 ($\epsilon_r = a + bx + cx^2$).

	a	**b (10^{-4}) [$\mathbf{K}^{-1}$]**	**c (10^{-5}) [$\mathbf{K}^{-2}$]**	χ^2
ϵ_r'	2.38	-60	1.50	$2{\cdot}10^{-4}$
ϵ_r''	0.03	-1	0.03	$1{\cdot}10^{-8}$

Apendix 3

Calibration constants

Table .2: Values for the calibration constants K_i (i = 1,2,3) determined in sec. 7.4. Shown are the values for the extended default frequency range (j denotes the complex number).

ν [Hz]	$\tilde{K}_1$ (10^3) [Sm^{-1}]	K_2 [Hz]	$\tilde{K}_3$ (10^4) [Sm^{-1}]
4	(3-3j)$\cdot 10^{-3}$	1.1+0.8j	0.02-0.04j
10	(5-13j)$\cdot 10^{-3}$	1.10+0.80j	0.03+0.10j
111	0.03+0.01j	0.73+0.70j	0.2+1.3j
576	0.2-0.7j	0.47+0.78j	0.9+6.8j
1.2k	0.4-1.4j	0.33+0.84j	1.9+14j
2.3k	0.8-2.5j	0.18+0.91j	3.4+2.8j
3.8k	1.4-4.0j	0.05+0.97j	4.8+47j
5.6k	2.2-5.7j	-0.08+1.00j	5.3+71j
8k	3.4-7.8j	-0.21+1.00j	3.4+103j
12k	5.1-11j	-0.46+1.05j	-13+160j
15.6k	5.7-14j	-0.90+0.88j	-84+216j
19.8k	6.3-18j	-1.39+0.60j	-228+271j

Uncertainty of calibration constants

Table .3: Errors for the calibration constants K_i (i = 1,2,3) of tab. .2

ν [Hz]	$\Delta\tilde{K}_1$ [Sm^{-1}]	ΔK_2 (10^{-4}) [Hz]	$\Delta\tilde{K}_3$ [Sm^{-1}]
4	0.8+1.7j	610+180j	1+1j
10	0.4+1.4j	63+43j	1+4j
111	0.2+1.7j	8+1j	1+1j
576	0.2+1.9j	5+1j	2+6j
1.2k	0.3+2.6j	4+1j	3+11j
2.3k	0.4+4.3j	4+1j	6+28j
3.8k	0.8+10.0j	8+1j	12+100j
5.6k	0.6+11.2j	5+1j	8+90j
8k	0.1+25.3j	15+1j	25+300j
12k	7.6+64.7j	27+8j	300+900j
15.6k	6.4+15.5j	1+2j	50+60j
19.8k	27.1+30.6j	1+9j	500+40j

Bibliography

[1] M. Hamelin, C. Beghin, R. Grard, J. Lopez-Moreno, K. Schwingenschuh, F. Simoes, R. Trautner, J. Berthelier, V. Brown, M. Chabassiere, P. Falkner, F. Ferri, M. Fulchignoni, I. Jernej, J. Jeronimo, G. Molina-Cuberos, R. Rodrigo, T. Tokano. Electron conductivity and density profiles derived from the mutual impedance probe measurements performed during the descent of Huygens through the atmosphere of Titan. *Planetary and Space Science* **55** (2007) 1964 .
DOI: 10.1016/j.pss.2007.04.008. Titan as seen from Huygens

[2] A. P. Zent, M. H. Hecht, D. R. Cobos, S. E. Wood, T. L. Hudson, S. M. Milkovich, L. P. DeFlores, M. T. Mellon. Initial Results from the Thermal and Electrical Conductivity Probe (TECP) on Phoenix. *J. Geophys. Res (Planets)* **115** (2010) 23

[3] K. J. Seidensticker, D. Möhlmann, I. Apathy, W. Schmidt, K. Thiel, W. Arnold, H.-H. Fischer, M. Kretschmer, D. Madlener, A. Péter. SESAME - An Experiment of the Rosetta lander Philae: Objectives and general design. *Space Science Reviews* **128** (2007) 301

[4] C. Kittel. *Einführung in die Festkörperphysik.* Oldenbourg, 2006, p.501-504

[5] I. N. Bronstein, K. A. Semendjajew, G. Musiol, H. Mühlig. *Taschenbuch der Mathematik.* Harri, Deutsch, 2005

[6] L. Onsager. Electric Moments of Molecules in Liquids. *Journal of the American Chemical Society* **58** (1936) 1486.
DOI: 10.1021/ja01299a050

[7] K. C. Kao. *Dielectric Phenomena in Solids.* Elsevier Academic Press, 2004, p. 61

[8] Feynman, Leighton, Sands. *The Feynman lectures on Physics*, Band 2. Pearson, Addison Wesley, 2006, p.114

[9] K. C. Kao. *Dielectric Phenomena in Solids.* Elsevier Academic Press, 2004, p. 71-72

[10] P. Hadley. Advanced Solid State Physics. Lecture notes, 2010

[11] A. Martinez, A. P. Byrnes. Modeling dielectric-constant values of geologic materials: An aid to ground-penetrating radar data collection and interpretation. *Current Research in Earth Sciences* **247** (2001) 1

[12] W. Plassmann, D. Schulz. *Handbuch Elektrotechnik: Grundlagen und Anwendungen für Elektrotechniker.* Vieweg + Teubner, 2009

[13] W. D. Kingery, H. Bowen, D. Uhlmann. *Introduction to Ceramics.* John Wiley and Sons, 2 Auflage, 1976

[14] P. Debye. *Polar Molecules.* Chemical Catalog, 1929

[15] K. S. Cole, R. H. Cole. Dispersion and absorption of dielectrics-1. Alterning Current Characteristics. *Journal of Chemical Physics* **9** (1941) 341

[16] R. H. Cole. On the Analysis of Dielectric Relaxation Measurement. *The Journal of Chemical Physics* **23** (1955) 493

[17] D. W. Davidson, R. H. Cole. Dielectric Relaxation in Glycerol, Propylene Glycol, and n-Propanol. *The Journal of Chemical Physics* **19** (1951) 1484

[18] S. Havriliak, S. Negami. A complex plane representation of dielectric and mechanical relaxation processes in some polymers. *Polymer* **8** (1967) 161 .
DOI: 10.1016/0032-3861(67)90021-3

[19] R. M. Hill, A. K. Jonscher. The Dielectric Behaviour of Condensed Matter and its Many-body Interpretation. *Contemporary Physics* **24** (1983) 75

[20] W. Kauzmann. Dielectric Relaxation as a Chemical Rate Process. *Rev. Mod. Phys.* **14** (1942) 12

[21] C. Weissmantel, C. Hamann. *Grundlagen der Festkörperphysik*, Band 4. Johann Ambrosius Barth, 1995, p.580

[22] E. Havinga. The temperature dependence of dielectric constants. *Journal of Physics and Chemistry of Solids* **18** (1961) 253 .
DOI: 10.1016/0022-3697(61)90169-X

[23] C. Weissmantel, C. Hamann. *Grundlagen der Festkörperphysik*, Band 4. Johann Ambrosius Barth, 1995, p.581-583

[24] W. R. Tinga, W. A. G. Voss, D. F. Blossey. Generalized approach to multiphase dielectric mixture theory. *Journal of Applied Physics* **44** (1973) 3897

[25] G. Mavko, T. Mukerji, J. Dvorkin. *The Rock Physics Handbook-Tools for seismic analysis in porous media.* Cambridge University Press, 1998, p.271

[26] G. Mavko, T. Mukerji, J. Dvorkin. *The Rock Physics Handbook-Tools for seismic analysis in porous media.* Cambridge University Press, 1998, p.272

[27] T. L. Chelidze, Y. Gueguen. Electrical spectroscopy of porous rocks: a review -1.Theoretical models. *Geophys. J. Int.* **137** (1999) 1

[28] T. Hanai, K. Sekine. Theory of dielectric relaxations due to the interfacial polarization for two-component suspensions of spheres. *Colloid & Polymer Sci* **264** (1986) 888

[29] G. Olhoeft, D. Strangway. Dielectric properties of the first 100 meters of the Moon. *Earth and Planetary Science Letters* **1975** (24) 394

[30] D. E. Stillman, R. E. Grimm, S. F. Dec. Low-Frequency Electrical Properties of Ice and Silicate Mixtures. *The Journal of Physical Chemistry B* **114** (2010) 6065. DOI: 10.1021/jp9070778. PMID: 20408561

[31] R. Knight, A. Endres. A new concept in modeling the dielectric response of sandstones: Defining a wetted rock and bulk water system. *Geophysics* **55** (1990) 586.
DOI: 10.1190/1.1442870

[32] R. H. Johnson, E. P. Poeter. Iterative use of the Bruggeman-Hanai-Sen mixing model to determine water saturations in sand. *Geophysics* **70** (2005) K33.
DOI: 10.1190/1.2049348

[33] R. Knight, A. Nur. The dielectric constant of sandstones, 60 kHz to 4 MHz. *Geophysics* **52** (1987) 644

[34] L. Rusiniak. Dielectric constant of water in a porous rock medium. *Physics and Chemistry of The Earth* **23** (1998) 1133 .
DOI: DOI: 10.1016/S0079-1946(98)00141-4

[35] M. Hamelin, R. Trautner, R. Grard. Detection of near-surface ice on Mars with electromagnetic techniques on board future surface vehicles. *Journal of Geophysical Research* **108** (2003) 8045

[36] C. J. F. Böttcher, P. Bordewijk. *Theory of electric polarization*, Band 2. Elesevier, 1978

[37] K. C. Kao. *Dielectric Phenomena in Solids.* Elsevier Academic Press, 2004, p.75

[38] Y.-Z. Wei, S. Sridhar. Dielectric spectroscopy up to 20 GHz of LiCl/H[sub 2]O solutions. *The Journal of Chemical Physics* **92** (1990) 923.
DOI: 10.1063/1.458074

[39] C. Weissmantel, C. Hamann. *Grundlagen der Festkörperphysik*, Band 4. Johann Ambrosius Barth, 1995, p.575

[40] A. Technologies. Impedance Measurement Handbook. Technischer Bericht 4, Agilent Technologies, 2009

[41] K. Knödel, H. Krummel, G. Lange (Herausgeber). *Geophysik*. Springer, 2005, p.174

[42] F. Kohlrausch. *Praktische Physik*. 1. B.G. Teubner Stuttgart, 24 Auflage, 1996, p.605-607

[43] M. C. H. McKubre, D. D. Macdonald. *Impedance Spectroscopy Theory, Experiment, and Applications*. John Wiley & Sons, 2 Auflage, 2005

[44] H. Vogel. *Gerthsen Physik*. Springer, 20 Auflage, 1999, p.438

[45] N. Technologies. *Alpha-A High Resolution Dielectric, Conductivity, Impedance and Gain Phase Modular Measurement System, User's Manual*. 11. Novocontrol Technologies, 2005

[46] K. Knödel, H. Krummel, G. Lange (Herausgeber). *Geophysik*. Springer, 2005, p.142

[47] F. Wenner. A method of measuring the Earth resistivity. *U.S. Bur. Stand. Bull. Sci. Pap.* **25** (1915) 469

[48] K. Knödel, H. Krummel, G. Lange (Herausgeber). *Environmental Geology*. Springer, 2007, p.205

[49] S. M. Zhdanov. *Geophysical electromagnetic theory and method*, Band 43 von *Methods in Geochemistry and Geophysics*. Elesevier, 2009, p.511

[50] R. D. Barker. Depth of investigation of collinear symmetrical four-electrode arrays. *Geophysics* **54** (1989) 1031.
DOI: 10.1190/1.1442728

[51] C. Weissmantel, C. Hamann. *Grundlagen der Festkörperphysik*, Band 4. Johann Ambrosius Barth, 1995, p.576

[52] J. C. Mankins. Affordable Mars Exploration Architectures: Applying Systems From The Commercial Development Of Space. *Acta Astronautica* **50** (2002) 27 .
DOI: DOI: 10.1016/S0094-5765(01)00145-X

[53] A. J. Ball, J. R. C. Garry, R. D. Lorenz, V. V. Kerzhanovich. *Planetary Landers and Entry Probes.* Camvridge University Press, 2007

[54] C. Pillinger. *The guide to Beagle 2.* Faber & Faber, 2003

[55] www.astronautix.com/craft/phoenix, 01/2011

[56] nssdc.gsfc.nasa.gov/nmc/spacecraftDisplay.do?id=2007-034A, 01/2011 01/2011

[57] P. Fortescue, J. Stark, G. Swinerd (Herausgeber). *Spacecraft System Engineering.* John Wiley and sons, 1995

[58] A. J. Ball, J. R. C. Garry, R. D. Lorenz, V. V. Kerzhanovich. *Planetary Landers and Entry Probes.* Camvridge University Press, 2007, p.95

[59] P. Fortescue, J. Stark, G. Swinerd (Herausgeber). *Spacecraft System Engineering.* John Wiley and sons, 2004, p.14

[60] (not official) G. Kminek. ESA Planetary Protection Requirements. Technischer Bericht ESSB-ST-PP-001, European Space Agency, 2010

[61] R. Trautner, R. Grard, M. Hamelin. Detection of subsurface ice and water deposits on Mars with a mutual impedance probe. *Journal of Geophysical Research* **108** (2003) 8047

[62] M. Hamelin, R. Grard, H. Laakso, R. Ney, W. Schmidt, F. Simoes, R. Trautner. Conductivity and Dielectric Characteristics of Planetary Surfaces Measured with Mutual Impedance Probes: From Huygens and Rosetta Lander to Netlanders and Future Missions. *Tools and Technologies for Future Planetary Exploration*, Band 543 von *ESA Special Publication* (Herausgeber B. Battrick), 2004 S. 169–174

[63] R. Grard. A quadrupolar array for measuring the complex permittivity of the ground: application to Earth prospection and planetary exploration. *Measurement Science and Technology* **1** (1990) 295

[64] G. Vannaroni, E. Pettinelli, C. Ottonello, A. Cereti, G. D. Monica, D. D. Vento, A. M. D. Lellis, R. D. Maio, R. Filippini, A. Galli, A. Menghini, R. Orosei, S. Orsini, S. Pagnan, F. Paolucci, A. R. Pisani, G. Schettini, M. Storini, G. Tacconi. MUSES: multi-sensor soil electromagnetic sounding. *Planetary and Space Science* **52** (2004) 67 .
DOI: DOI: 10.1016/j.pss.2003.07.003. Exploring Mars Surface and its Earth Analogues

[65] Simões, R. Grard, M. Hamelin, J. López-Moreno, K. Schwingenschuh, C. Béghin, J.-J. Berthelier, J.-P. Lebreton, G. Molina-Cuberos, T. Tokano. The Schumann resonance: A tool for exploring the atmospheric environment and the subsurface of the planets and their satellites. *Icarus* **194** (2008) 30. DOI: 10.1016/j.icarus.2007.09.020

[66] R. Grard. A quadrupole system for measuring in situ the complex permittivity of materials: application to penetrators and landers for planetary exploration. *Measurement Science and Technology* **1** (1990) 801

[67] D. Möhlmann. Water in the upper martian surface at mid- and low-latitudes: presence, state, and consequences. *Icarus* **168** (2004) 318

[68] P. Rochette, J. Gattacceca, V. Chevrier, P. Mathé, M. Menvielle. Magnetism, Iron Minerals, and Life on Mars. *Astrobiology* **6** (2006) 423

[69] R. W. Zurek. Martian Great Dust Storms: An Update. *Icarus* **50** (1982) 288

[70] W. Fa, F. Xu, Y. Jin. SAR imaging simulation for an inhomogeneous undulated lunar surface based on triangulated irregular network. *Science in China Series F: Information Sciences* **52** (2009) 559

[71] T. Spohn, A. J. Ball, K. Seiferlin, V. Conzelmann, A. Hagermann, N. I. Kömle, G. Kargl. A heat flow and physical properties package for the surface of Mercury. *Planetary and Space Science* **49** (2001) 1571.
DOI: 10.1016/S0032-0633(01)00094-0

[72] M. Grott. Thermal disturbances caused by lander shadowing and the measurability of the martian planetary heat flow. *Planetary and Space Science* **57** (2009) 71

[73] M. S. Skidmore. *A Geophysical Package for In situ Planetary Science*. Dissertation, University of Leicester, 2009

[74] R. Trautner, F. Simoes, R. Grard, M. Hamelin. A New Instrument for Measuring the Low-Frequency Electrical Properties of Planetary Subsurface Materials. *Tools and Technologies for Future Planetary Exploration*, Band 543 von *ESA Special Publication* (Herausgeber B. Battrick), 2004 S. 193–196

[75] G. Kargl. HP 3 PP Design Document, 2010. Private communication

[76] National Instruments, LabView 8.6, 2008

[77] R. E. Grimm. Low-frequency electromagnetic exploration for groundwater on Mars. *Journal of Geophysical Research* **107** (2002) 1

[78] V. Ciarletti, C. Corbel, F. Cais, D. Plettemeier, S. Hamran, M. Øyan, the Wisdom instrument team. Performances of the WISDOM GPR designed for the shallow sounding of Mars. *40th Lunar and Planetary Science Conference*, 2009 S. 2367

[79] J. J. Berthelier, R. Neya, F. Costardb, M. Hamelina, A. Meyera, B. Martinatc, A. Reineixc, T. Hansend, M. Banoe, W. Kofmanf, F. Lefeuvreg, P. Paillou. The GPR experiment on NETLANDER. *Planetary and Space Science* **48** (2000) 1161.
DOI: 10.1016/S0032-0633(00)00101-X

[80] D. Parasnis. *Principles of Applied Geophysics.* Chapman & Hall, 5 Auflage, 1997

[81] K. Knödel, H. Krummel, G. Lange (Herausgeber). *Geophysik.* Springer-Verlag, 2005, p.389-424

[82] M. Nabighian. *Controlled source audio-frequency magnetollurgics*, Band 2 von *Electromagnetic Methods in Applied Geophysics.* Soc. Explor. Geophys., 1991

[83] G. R. Olhoeft. Subsurface exploration for water on Mars. *Sixth International Conference on Mars*, 2003 S. 3213

[84] P. Caïs. Wisdom Electronic Unit Thermal and Structural Analysis (draft version). Technischer Bericht, 2008. Draft version

[85] R. E. Grimm, B.Berdanier, R. Warden, J. Harrer, R. Demara, J. Pfeiffer, R. Blohm. A time-domain electromagnetic sounder for detection and characterization of groundwater on Mars. *Planetary and Space Science* **57** (2009) 1268.
DOI: 10.1016/j.pss.2009.05.003

[86] L. S. Edwards. A modified pseudosection for resistivity and IP. *Geophysics* **42** (1977) 1020.
DOI: 10.1190/1.1440762

[87] www.faigle.com/Materials.aspx?Language=DE&Nav=materialtabelle. internet, 02/2011

[88] Fa. Faigle Kunststoffe GmbH, Materialtabelle PAS PTFE rein, 02/2011

[89] E. Laredo, M. Grimau, F. Sanchez, A. Bello. Water Absorption Effect on the Dynamic Properties of Nylon-6 by Dielectric Spectroscopy. *Macromolecules* **36** (2003) 9840.
DOI: 10.1021/ma034954w

[90] G. R. Olhoeft, D. W. Strangway. Electrical properties of the surface layers of Mars. *Geophysical Research letters* **1** (1974) 141

[91] F. Simoes, R. Trautner, R. Grard, H. Hamelin. Laboratory Measurements on Martian Soil Simulant JSC Mars-1 supporting the calibration of Instruments for Planetary Missions. *Proceedings of the 37th ESLAB Symposium Tools and Technologies for Future Planetary Exploration* **1** (2004) 543.
DOI: 10.1103/PhysRevB.2.883

[92] A. Cereti, M. T. Mellon, H. G. Sizemore, R. J. Phillips. Measurements of dielectric properties of Mars analog soils with variable temperature and moisture content. *40th Lunar and Planetary Science Conference*, 2009 S. 2189

[93] D. Evans, J. Adams, T. Farr, T. Roush. Terrestrial and synthetic analogs to Martian weathering products. *Proc. 10th Lunar Planet. Sci. Conf.* **10** (1979) 1829

[94] R. V. MORRIS, D. C. GOLDEN, J. F. B. III, H. V. L. JR., J. B. ADAMS. Pigmenting agents in Martian soils: Inferences from spectral, Miissbauer, and magnetic properties of nanophase and other iron oxides in Hawaiian palagonitic soil PN-9*. *Geochimica et Cosmochimica Acta* **57** (1993) 4597

[95] G. Hofbauer. Complex permittivity measurements by the three-term network-analysis method and capacitive voltage division. Private communication

[96] W. Klein. *Mehrtortheorie*, Band 3. Akademie Verlag, 1976

[97] G. Kirchengast, A. Steiner. Methoden der Modellierung und Simulation. Lecture notes, 2010

[98] private communication. Technischer Bericht, Novocontrol Technologies GmbH & Co. KG, 2010. 2010

[99] MatLab 7.1, The MathWorks Inc., 2005

[100] Aluminiumoxid wasserfrei (gamma-Tonerde), Art.Nr.101095, Product information sheet. Technischer Bericht, Fa. Merck Chemicals, Germany, 2010

[101] A. A. Garrouch, M. M. Sharma. The influence of clay content, salinity, stress, and wettability on the dielectric properties of brine-saturated rocks: 10 Hz to 10 MHz. *Geophysics* **59** (1994) 909

[102] T. L. Chelidze, Y. Gueguen, C. Ruffet. Electrical spectroscopy of porous rocks: a review-II. Experimental results and interpretation. *Geophys. J. Int.* **137** (1999) 16

[103] M. Saint-Amant, D. W. Strangway. DIELECTRIC PROPERTIES OF DRY, GEOLOGIC MATERIALS. *Geophysics* **35** (1970) 624.
DOI: 10.1190/1.1440120

[104] G. Hofbauer. Private communication, 02.2011

[105] D. Strangway, W. Chapman, G. Olhoeft, J. Carnes. Electrical properties of lunar soil dependence on frequency, temperature and moisture. *Earth and Planetary Science Letters* **16** (1972) 275 .
DOI: 10.1016/0012-821X(72)90203-8

[106] S. Evans. Dielectric properties of ice and snow-a review. *Journal of Glaciology* **5** (1965) 773

[107] P. Nornberg, U. Schertmann, H. Stanjek, T. Andersen, H. P. Gunnlaugsson. Mineralogy of a burned soil compared with four anomalously red Quaternary deposits in Denmark. *Clay Minerals* **39** (2004) 85

[108] P. Nornberg, H. P. Gunnlaugsson, J. P. Merrison, A. L. Vendelboe. Salten Skov I: A Martian magnetic dust analogue. *Planetary and Space Science* **57** (2009) 628 .
DOI: 10.1016/j.pss.2008.08.017

[109] C. C. Allen, R. V. M. D. J. Lindstrom, M. M. Lindstrom, J. P. Lockwood. JSC Mars-1 - Martian regolith simulant. *Lunar and Planetary Science XXVIII*, 1997 S. 1797

[110] M. Loke. Tutorial : 2-D and 3-D electrical imaging surveys, 2004. Www.geoelectrical.com

[111] A. K. Jonscher. Dielectric relaxation in solids. *Journal of Physics D: Applied Physics* **32** (1999) R57

[112] Feuchtebestimmer MAC-50, Art.Nr MAC 50 .2, Rauch, Graz (Austria), 2010

[113] K. Seiferlin, P. Ehrenfreund, J. Garry, K. Gunderson, E. Hütter, G. Kargl, A. Maturilli, J. P. Merrison. Simulating Martian regolith in the laboratory. *Planetary and Space Science* **56** (2008) 2009